UNIVERSITAT ROVIRA I VIRGILI

Preparation and characterization of surfaces modified with carbon nano-onions. Biomedical and environmental applications

Julio César Zuaznabar Gardona

ADVERTIMENT. L'accés als continguts d'aquesta tesi doctoral i la seva utilització ha de respectar els drets de la persona autora. Pot ser utilitzada per a consulta o estudi personal, així com en activitats o materials d'investigació i docència en els termes establerts a l'art. 32 del Text Refós de la Llei de Propietat Intel·lectual (RDL 1/1996). Per altres utilitzacions es requereix l'autorització prèvia i expressa de la persona autora. En qualsevol cas, en la utilització dels seus continguts caldrà indicar de forma clara el nom i cognoms de la persona autora i el títol de la tesi doctoral. No s'autoritza la seva reproducció o altres formes d'explotació efectuades amb finalitats de lucre ni la seva comunicació pública des d'un lloc aliè al servei TDX. Tampoc s'autoritza la presentació del seu contingut en una finestra o marc aliè a TDX (framing). Aquesta reserva de drets afecta tant als continguts de la tesi com als seus resums i índexs.

ADVERTENCIA. El acceso a los contenidos de esta tesis doctoral y su utilización debe respetar los derechos de la persona autora. Puede ser utilizada para consulta o estudio personal, así como en actividades o materiales de investigación y docencia en los términos establecidos en el art. 32 del Texto Refundido de la Ley de Propiedad Intelectual (RDL 1/1996). Para otros usos se requiere la autorización previa y expresa de la persona autora. En cualquier caso, en la utilización de sus contenidos se deberá indicar de forma clara el nombre y apellidos de la persona autora y el título de la tesis doctoral. No se autoriza su reproducción u otras formas de explotación efectuadas con fines lucrativos ni su comunicación pública desde un sitio ajeno al servicio TDR. Tampoco se autoriza la presentación de su contenido en una ventana o marco ajeno a TDR (framing). Esta reserva de derechos afecta tanto al contenido de la tesis como a sus resúmenes e índices.

WARNING. Access to the contents of this doctoral thesis and its use must respect the rights of the author. It can be used for reference or private study, as well as research and learning activities or materials in the terms established by the 32nd article of the Spanish Consolidated Copyright Act (RDL 1/1996). Express and previous authorization of the author is required for any other uses. In any case, when using its content, full name of the author and title of the thesis must be clearly indicated. Reproduction or other forms of for profit use or public communication from outside TDX service is not allowed. Presentation of its content in a window or frame external to TDX (framing) is not authorized either. These rights affect both the content of the thesis and its abstracts and indexes.

UNIVERSITAT
ROVIRA i VIRGILI

Preparation and characterization of surfaces modified with carbon nano-onions. Biomedical and environmental applications

---

JULIO CÉSAR ZUAZNABAR GARDONA

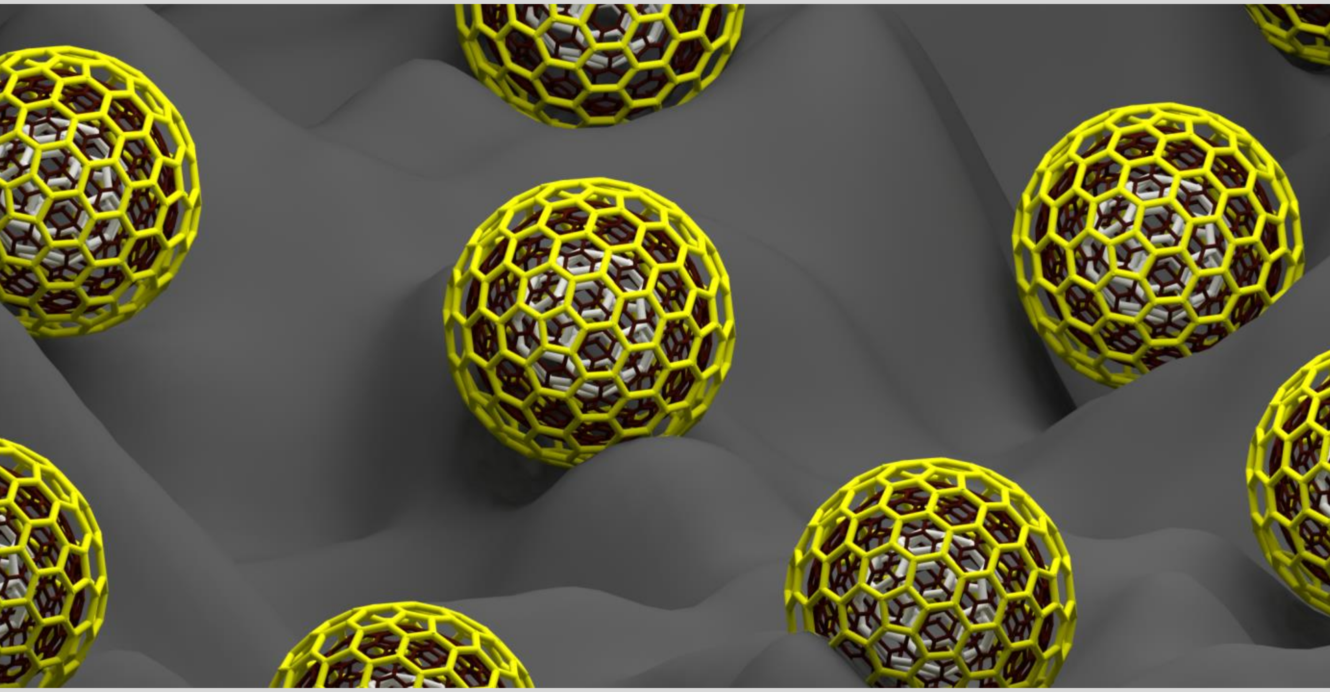

DOCTORAL THESIS
2020

Preparation and characterization of surfaces modified with carbon nano-onions. Biomedical and environmental applications
Julio César Zuaznabar Gardona

Julio César Zuaznabar Gardona

PREPARATION AND CHARACTERIZATION OF SURFACES MODIFIED WITH CARBON NANO-ONIONS. BIOMEDICAL AND ENVIRONMENTAL APPLICATIONS

DOCTORAL THESIS

supervised by Dr. Alex Fragoso Sierra

Departament d'Enginyeria Química

UNIVERSITAT ROVIRA i VIRGILI

Tarragona

2020

UNIVERSITAT
ROVIRA I VIRGILI
Departament d'Enginyeria Química
Universitat Rovira i Virgili
Campus Sescelades,
Avda. Països Catalans, 26
43007 Tarragona
Tel: 977 55 85 79
Fax: 977 55 96 67

Dr. Alex Fragoso

CERTIFIES:

That the present study, entitled "**Preparation and characterization of surfaces modified with carbon nano-onions. Biomedical and environmental applications**" presented by Julio César Zuaznabar Gardona for the award of the degree of Doctor, has been carried out under my supervision at the Department of Chemical Engineering of Universitat Rovira i Virgili.

Tarragona, November 2nd 2020.

Dr. Alex Fragoso

Acknowledgements

Each time I have finished a step in my academic formation, I have the moral duty to express my gratitude to those people who have contributed to my advance in different ways.

First, I would like to thank my former chemistry teachers at the secondary school, Dani and Misladys, who introduced me to the world of reactions, stoichiometry and mixtures. I want to thank Agustin and Jorge Enrique who continued my formation in molecular orbital theory, chemical equilibrium and thermodynamic at high school. Agustin was my defensor against to those that considered that working at the farm´s school was more important than training for chemistry olympiads. I have to mention the names of Luis Guerra, Rolando, Isidro and Landrove. They were my teachers at the Cuban national training center for olympiads of knowledge, known as “la preselección”. To them, I owe the decision to be a good chemist or at least to attempt it.

During my Bachelor degree at the Faculty of Chemistry of Havana University in Cuba, I was lucky to have great teachers who then, became colleagues and friends. I thank Prof. Néstor Fernandez for teaching me about inorganic chemistry, periodicity, electronic structure of solids and about the importance of a clear and precise language in science. Unfortunately, he is no longer among us physically, but his lessons are imperishable. I am grateful to meet Prof. Alicia Diaz who taught me about coordination chemistry, nanoparticle synthesis and electrochemistry, but more important, she is my referent in science of humility, modesty and kindness. To Prof.

Pedro Ortiz and Carlos Pérez for showing me the wave-particle duality and that the spin is not the rotation of electrons. I also want to thank Prof. Margarita Suarez for her unique way of teaching organic chemistry. To Prof. Luis Alberto Montero for opening without hesitation the doors of the Theoretical and Computational Chemistry group to this rookie experimentalist. To all of them, one mole of thanks.

The experience to leave your home country and its consequences were more bearable thanks to a new family I met in Tarragona. We were at same Faculty and worked at the same labs in Cuba but, we did it at different moments. Fortunately, it was by chance we met here in this Mediterranean city. I am referring to Mabel, Jose Luis, Neyvis, Mayreli and Alex. Mabel proved to me that is possible to live in the same city and have a quite different time zone (+ 6 hrs) and also to have always a smile despite the adversities. I will never forget all the times Jose Luis was willing to drive me from Altafulla to Tarragona even at late hours and his patience to deal with our small but noisy Cuban community. I thank Neyvis for guiding me since I arrived at Tarragona and for the good times we shared together. I am grateful to Mayreli for always taking care of me and being like a mother in a foreign country.

My most sincere gratitude to Dr. Alex Fragoso, my supervisor and friend. For his invaluable guidance, his accurate vision of life and science, his timely comments, his pragmatism, and for all his patience with this diffuse student. Thanks for trusting me even when I was deviating from the correct path and for giving me endless degrees of

freedom to work. This thesis would not have been possible without your expertise, efforts and command.

Also, my special gratitude to Dr. Pascal Blondeau for his excellent lessons on supramolecular chemistry and for his support whenever I needed any materials, reagents or equipment from the Laboratory of Nanosensors.

I am very grateful for the FPU predoctoral scholarship (FPU 15/04761) from the Ministerio de Educación, Cultura y Deporte and the grant BIO2017-87946-C2-1-R from Ministerio de Ciencia, Innovación y Universidades, Spain which provided the funds for the execution of this project.

I should thank Nuria Juanpere for her constant help and her efficiently work.

I want to give special thanks to all members of INTERFIBIO group for their help during these years, but specially to Mary Carmen for her muffins, to Dr. Miriam Jauset, our black-belt in lateral flow assays and my wine-mate and friend, to my step-daughter Laura Andrea, and also to Ivan, Iris and Vibol. Thanks for the laughs and the spare time in and out of the lab.

I am lucky to have someone to share my happiness but also my weakness, my fears and mistakes. This person is my beloved Zaida. Thanks for inviting me to play Volley with you, for making me part of your family and your circle of friends. Thanks for being so patient with this grumpy and sometimes stubborn man. Thanks for your support, your cares and your constant encouragement. Thanks for

your transparence, your honesty and your absence of second thoughts. But above all, thanks for deciding to share your life and time with this guy who is irreversibly in love with you.

I am greatly grateful for having my other family, the one from here. The Herrero Medina family. Thanks to all for the warmth and for making me feel like at home. Thanks for the experience of belonging to a huge family. Thanks for joining me, for taking me in, and for the times we have spent together.

I must thank my aunt Omaira for all her support. I am here thanks to her. Her endless generosity is an example for me. To Pedro for taking care of my aunt and always opening his house´s doors to me. To my cousins Leidy, Liane and Michel for all the good moments we have spent together.

Finally, I am deeply grateful for my dear mother and father. They have paid the highest cost to make this work possible. Thanks for not hesitating to support my decision to find my way living abroad. Thanks for all the values you instilled in me, all your sacrifices, your devotion and your unconditional love. This work is entirely dedicated to you. All what I am and I have done, it has been thanks to you, I am indebted to you.

To all of you, THANKS!!

List of publications derived from the present Doctoral Thesis

1- J.C. Zuaznabar-Gardona, A. Fragoso, Electrochemical characterisation of the adsorption of ferrocenemethanol on carbon nano-onion modified electrodes, J. Electroanal. Chem. 871 (2020) 114314.

2- J.C. Zuaznabar-Gardona, A. Fragoso, Band structure, work function and interfacial diagrams of oxygen-functionalized carbon nano-onions, Synth. Met. 266 (2020) 116434.

3- J.C. Zuaznabar-Gardona, A. Fragoso, Electrochemistry of redox probes at thin films of carbon nano-onions produced by thermal annealing of nanodiamonds, Electrochim. Acta. 353 (2020) 136495.

4- J.C. Zuaznabar-Gardona, A. Fragoso, Development of highly sensitive IgA immunosensors based on co-electropolymerized L-DOPA/dopamine carbon nano-onion modified electrodes, Biosens. Bioelectron. 141 (2019) 111357.

5- J.C. Zuaznabar-Gardona, A. Fragoso, Determination of the Hansen solubility parameters of carbon nano-onions and prediction of their dispersibility in organic solvents, J. Mol. Liq. 294 (2019) 111646.

6- J.C. Zuaznabar-Gardona, A. Fragoso, A wide-range solid state potentiometric pH sensor based on poly-dopamine coated carbon nano-onion electrodes, Sensors Actuators B Chem. 273 (2018) 664.

Abbreviations

AA: ascorbic acid
AC: activated carbon,
Ac$_2$O: acetic anhydride
ACA: 2,4-pentanedione
ACE: acetone
ACN: acetonitrile
AMC: amorphous carbon
AT: assay time
AuNPs: gold nanoparticles
B.C.: before Christ
BODIPY: boron-dipyrromethene
BSA: bovine serum albumin
BuOH: 1-butanol
BzOH: benzyl alcohol
C$_{60}$: fullerene
CA: choronoamperometry.
CC: catechol
CEA: carcinoembryonic antigen
CF: carbon fibers
CHCl$_3$: chloroform
cHEX: cyclohexane
CMs: Carbon based materials
CNO-OXI: chemically oxidized CNOs
CNO-RF: radio frequency Ar/O$_2$ plasma oxidized CNOs
CNOs: carbon nano-onions
CNTs: carbon nanotubes
CS: chitosan
CTAB: hexadecyltrimethylammonium bromide
CV: cyclic voltammetry
CVs: cyclic voltammograms
DA: dopamine
Det: detection
DHB: dihydroxybenzene
DIOX: dioxane
DLS: dynamic light scattering
DMF: N,N-dimethylformamide
DMSO: dimethyl sulfoxide
DNA: deoxyribonucleic acid
DOS: density of states
DPME: dipropylene glycol methyl ether
DPSC: double potential step chronocoulometry
DPV: differential pulse voltammetry
EDC: 1-Ethyl-3-(3-dimethylaminopropyl)carbodiimide
E$_F$: Fermi level
EGDA: ethylene glycol diacetate
EGDA: ethylene glycol diacetate
EIS: electrochemical impedance spectroscopy
ELISA: enzyme-linked immunosorbent assay
EPR: electron paramagnetic resonance spectroscopy
ESEM: environmental scanning electron microscopy
Et$_2$O: diethyl ether
EtOH: ethanol
FA: formamide
FcCH$_2$OH: ferrocenemethanol
FcNH$_2$: aminoferrocene
FTIR: Fourier-Transformed Infrared spectroscopy
FWHM: full width at half maximum
GC: glassy carbon
GCE/CNO/c-PDA: GCE/CNO electrodes modified with chemical polymerized DA

GCE/CNO/e-PDA: GCE/CNO electrodes modified with electropolymerized DA
GCE/CNO/PDA: GCE/CNO modified with polydopamine
GCE/CNO: glassy carbon electrodes modified with CNOs
GCE/CNO-OXI: glassy carbon electrodes modified with CNO-OXI
GCE/CNO-RF: glassy carbon electrodes modified with CNO-RF
GCE: glassy carbon electrodes
GOx: graphene oxide
hCG: human chorionic gonadotropin
HEP: heptane
HET: heterogeneous electron transfer
HEX: hexane
HOMO: highest occupied molecular orbital
HOPG: highly oriented pyrolytic graphite
HPV: human papillomavirus
HQ: hydroquinone
HRP: horseradish peroxidase
HRTEM: high resolution transmission electron microscopy
HSPs: Hansen solubility parameters
IgA: immunoglobulin A
L-DOPA: L-3,4-dihydroxyphenylalanine
LDR: linear detection range
LOD: limit of detection
LR: linear range
LSV: linear sweep voltammetry
MD: methodology
MeOH: methanol
MES: 2-(N-morpholino)ethanesulfonic acid
MWCNTs: multi-walled carbon nanotubes
N-CNOs: nitrogen doped CNOs
NDs: nanodiamonds
Nepm: nephelometer
Nepy: nephelometry
NHE: Normal Hydrogen Electrode
NHS: N-hydroxysuccinimide
NMP: N-methyl-2-pyrrolidone
OCT: octane
ORR: oxygen reduction reaction
P:preparation
PAN: particle-enhanced nephelometric
PANI: polyaniline
PB: phosphate buffer
PBS: Phosphate-buffered saline
PDA: polydopamine
PDAB: poly-(1,2-diaminobenzene)
PDDA: poly(diallyldimethylammonium chloride)
PEI: polyethylenimine
PhEt: ethylbenzene
$PhNO_2$: nitrobenzene
poly(L-DOPA/DA): copolymer of DA and L-DOPA
PPI: polypropylenimine
RED: relative energy difference
RF: radio frequency
RS: resorcinol
SDBS: sodium dodecyl benzene sulfonate
SDS: sodium dodecyl sulfate
Self-P: self-polymerization
SP: sensing platform

SPE: screen-printed electrodes
SS: signal source
SSA: specific surface area
STM: scanning tunneling microscopy
SWCNTs: single-walled carbon nanotubes
SWCNTs-OXI: oxidized single-walled carbon nanotubes
TBA: tert-butyl alcohol
TCE: 1,1,2,2-tetrachloroethane
TEM: transmission electron microscopy
THF: tetrahydrofuran
TMB: 3,3',5,5'-tetramethylbenzidine
TOL: toluene
Triton X-100: 4-(1,1,3,3-tetramethylbutyl)phenyl-polyethylene glycol
Tween 20: polyethylene glycol sorbitan monolaurate
UA: uric acid
UB: universal buffer
UPS: ultraviolet photoelectron spectroscopy
XPS: X-ray photoelectron spectroscopy
XRD: X-ray diffraction
α-IgA: anti-human IgA (μ-chain specific) antibody produced in goat
α-IgA-HRP: anti-human IgA-peroxidase conjugate

Table of contents

Summary

The focus of the present thesis is to prepare and characterize surfaces modified with carbon nano-onions (CNOs) to develop electrocatalytic systems and electrochemical (bio)sensors for biomedical and environmental applications.

Chapter 1 is a general introduction to the topics that will be discussed in this thesis. It covers general information about carbon materials with emphasis in the preparation, characterization, functionalization and electrochemical (bio)sensing applications of CNOs.

Chapter 2 covers the dispersibility study of CNOs in 20 solvents of different polarities. These solvents were classified as “good” or “bad” to determine the Hansen solubility parameters (HSPs) for CNOs using various optimization approaches. These parameters were further used to predict the dispersion behavior of CNOs in other solvents with a very good agreement between expected and observed dispersibilities.

Chapter 3 is dedicated to study the effect of two oxidation treatments on the electronic structure and the surface chemical composition of CNOs. Pristine, physical and chemical oxidized CNOs were analyzed by using ultraviolet photoelectron spectroscopy (UPS) and X-ray photoelectron spectroscopy (XPS). It was found that each oxidative treatment affects the electronic structure and the surface chemical composition of CNOs in different ways. The interfacial energy

diagrams for pristine and oxidized CNOs are also provided and used to explain some electrochemical properties of these materials.

Chapter 4 provides electrochemical data for pristine CNOs, radio frequency Ar/O_2 plasma oxidized CNOs (CNO-RF) and chemically oxidized CNOs (CNO-OXI) cast on glassy carbon (GC) electrodes. The electrochemical response was evaluated by cyclic voltammetry using $[Fe(CN)_6]^{3-}$, $[Ru(NH_3)_6]^{3+}$, $[Fe(H_2O)_6]^{2+}$ and ferrocenemethanol ($FcCH_2OH$) as redox probes. The results indicate the electron transfer kinetics for these probes was influenced by the nature of functional groups on the electrode material, adsorption processes and the electrostatic interactions between the redox probes and the surface of the different carbon nano-onions.

Chapter 5 is a deeper understanding of the electrochemical behaviour of $FcCH_2OH$ and $[Fe(CN)_6]^{3-}$ redox probes at unmodified and CNOs modified GC electrodes. Cyclic voltammetry experiments were used to demonstrate that the electrochemical response of $[Fe(CN)_6]^{3-}$ is a fully diffusion-controlled process, while for $FcCH_2OH$ a weak adsorption of its reduced form takes place on the GCE/CNO electrodes and in higher extension than on bare GC electrodes. Double potential step chronocoulometry was used to obtain the empirical adsorption isotherms which were found to respond to the Sips model isotherm.

Chapter 6 explores the electrocatalytic properties of CNO, CNO-RF and CNO-OXI modified electrodes. At these surfaces, the electroreduction of O_2 to H_2O_2 in acid media and the electrooxidation of H_2O_2, ascorbic acid (AA), dopamine (DA) and uric acid (UA) were studied by cyclic voltammetry and differential pulse voltammetry. The modified electrodes displayed excellent electrocatalytic activity to these molecules. The results demonstrate that CNOs enhance the electroactive properties of redox molecules and are thus promising materials for electrochemical detection and metal-free electrocatalysts of different reactions.

Chapter 7 introduces a novel potentiometric pH sensor based on polydopamine films coated on CNOs conductive surfaces. Glassy carbon electrodes containing a carbon nano-onion layer were modified by electropolymerization and self-polymerization of dopamine. The modified surfaces were characterized by ESEM, Raman spectroscopy and cyclic voltammetry. The modified electrodes displayed an almost Nernstian potentiometric response over the pH range 2-10. Furthermore, the pH sensors exhibit a fast and reversible behavior toward variations of pH and negligible interference effects from monovalent cations. The sensors showed an excellent correspondence between the pH values obtained using the GCE/CNO/PDA electrodes and those measured with glass electrodes.

Chapter 8 explores the possibility to use the co-electropolymerization of DA and L-3,4-dihydroxyphenylalanine (L-DOPA) on CNOs modified electrodes as versatile platform to develop electrochemical immunosensors. Mixtures of DA and L-DOPA at different molar rations were co-electropolymerized on CNOs-modified glassy carbon electrodes to form a poly(L-DOPA/DA) film. This platform was applied to the electrochemical detection of IgA antibodies using both a HRP-based sandwich type assay and a label-free detection based on $[Fe(CN)_6]^{3-/4-}$ signal blocking. The sandwich and the label-free assays showed a wide linear response and suitable LOD to allow the detection of serum IgA deficiency. Most remarkably, the incorporation of CNOs layer led to a significant improvement (three-orders of magnitude) of the analytical performance of these immunosensors.

Overall, the presented thesis has contributed to expand the current knowledge on the dispersibility, electronic structure, surface chemical composition and electrochemical properties of CNOs. Novel electrocatalytic properties and electrochemical (bio)sensing applications of these materials were also explored and systematized to understand their relationship with the electronic structure of CNOs. The results presented here illustrate the advantages of incorporating CNOs in the design of electrochemical systems to improve their performance. These results might also help to fabricate tailor made surfaces with unique properties to realize high potential of CNOs to the maximum and to open new application possibilities in areas such as electrochemical energy storage and electroanalytical methods.

Chapter 1

Introduction

1.1. Carbon materials

The earliest known use of carbon materials dates back to circa 3750 B.C., when Egyptians and Sumerians used wood chars (charcoal) for the reduction of copper, zinc and tin ores to manufacture bronze [1]. Since then, carbon materials have played important roles in industry and technology. For example, coal is the second largest fuel after oil accounting for about the 30% of the global energy production [2], graphite electrodes are extensively used in batteries and to slow-down fission reactions in nuclear plants. Carbon materials are also one of the hottest topics in materials research nowadays. In the last three decades, research on these materials have led to two Nobel Prizes (for fullerenes and graphene), and two Kavli Prizes in Nanoscience (to M. Dresselhaus and S. Iijima for work on carbon nanotubes) [3]. These examples illustrate the immense importance of carbon materials and research on this field.

Carbon materials are a huge family of materials that are mainly constituted by carbon atoms, although their structures and properties can vary significantly. Some of them like diamond are electric insulators and transparent with carbon atoms bonded in a tetrahedral geometry. Others like graphite are electric conductors and black opaque with carbon atoms arranged in a honeycomb lattice. Diamond, graphite, carbon fibers, glassy carbons, amorphous carbon and activated carbons (Figure 1.1 left) represent the bulky (macroscopic) members of the carbon materials' family. Their preparations, properties, and applications have been covered in different works and are out of the scope of this chapter [4,5].

Carbon materials with nanoscopic dimensions, also known as carbon nanomaterials, are a growing subgroup that is difficult to cover totally in a simple chapter. Thus, here it will be only mentioned some of them (Figure 1.1 right) that we modestly considered the most representative carbon nanomaterials. More information about carbon nanomaterials can be found in detailed reviews [6–8], and monographies [9,10], among many others.

The subgroup of carbon nanomaterials started with the discovery of fullerene (C_{60}) by H. Kroto, R. E. Smalley, and R. F. Curl in 1985 [11]. Fullerene C_{60} has a truncated icosahedral structure with hexagonal and pentagonal rings made up of "sp^2" hybridized carbon atoms. Since the arrangement of carbon atoms is pyramidalized to allow curvature, a pseudo sp^3 bonding component must be present. Thus, the hybridization of carbon atoms in C_{60} should be between sp^2 and sp^3 instead of a purely sp^2 hybridization [12]. Several other C_n-type structures have been subsequently discovered, but C_{60} is by far the most widely studied to date [6]. The properties of C_{60} lie on the boundary between molecules and nanomaterials. Thus, it has gathered intense research interest for many applications in functional materials and nanodevices [13–15].

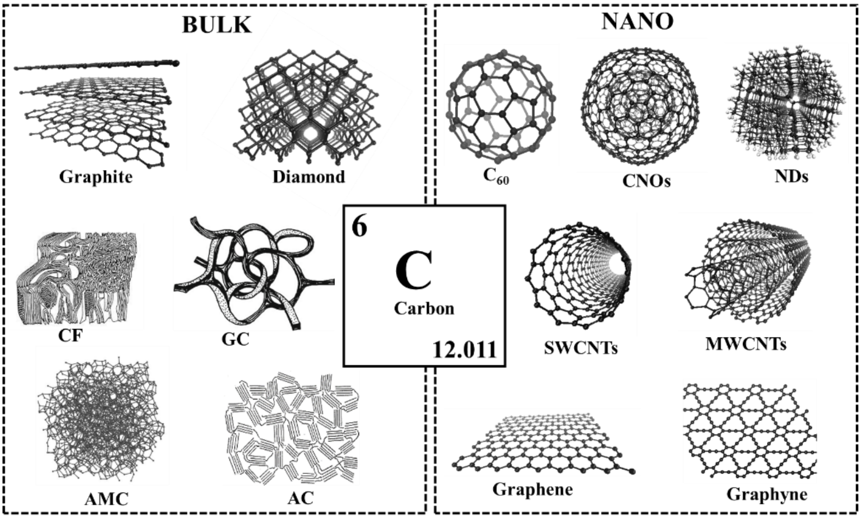

Figure 1.1. Schematic representation of different carbon materials. CF: carbon fibers, GC: glassy carbon, AMC: amorphous carbon, AC: activated carbon, C_{60}: fullerene, CNOs: carbon nano-onions, NDs: nanodiamonds, SWCNTs: single-walled carbon nanotubes, and MWCNTs: multi-walled carbon nanotubes.

In 1991, carbon nanotubes (CNTs) were formally rediscovered by S. Iijima [16,17]. It seems that multi-walled carbon nanotubes (MWCNTs) were first discovered by two Russian scientists, L.V. Radushkevich and V.M. Lukyanovich, in 1952 [18], and it has been argued they should be credited for the discovery of CNTs [19]. CNTs consist in 1 or *n*-th rolls of graphene layers (where *n* is an integer) wrapped around together to form a cylindrical tube formed by sp^2 hybridized carbon atoms. The diameter of the tube ranges from few nanometers up to 100 nm, while the longitude may be up to the order of millimeters [20]. The sp^2 hybridized carbon atoms in a cylindrical shape give CNTs a high conductivity, excellent strength and stiffness [21]. These characteristics are translated in suitable properties of CNTs for a wide range of applications [22,23].

Nanodiamonds (NDs) became popular in the 90's, although they were accidentally discovered much back in the 1960s by Russian scientists [24]. NDs are polyhedral particles with sizes between 2 and 10 nm. Their structure consists of a diamond core built up of sp^3 hybridized carbon atoms, which may be partially coated by a graphitic shell or amorphous carbon with dangling bonds terminated by functional groups [25]. The properties of NDs differ from that of bulk diamond expanding the applications of NDs in a variety of research fields as it was reviewed recently [26].

The next major step on carbon nanomaterials was taken in 2004 with the isolation and characterization of graphene by A. Geim and K. Novoselov [27]. The existence of graphene was predicted in 1947 [28], and experimentally identified by Boehm et al. in 1962 [29]. Graphene is a one-atom-thick layer of sp^2-hybridized carbon atoms arranged in a honeycomb lattice. Thus, it can be considered as the building block of graphite and CNTs. Graphene is remarkably strong for its atomic thinness and conducts heat and electricity with great efficiency because of its unusual electronic structure [10,28]. More details about graphene structure, its properties and applications can be found in several books and reviews [5,10,30–33].

Further efforts on the design and synthesis of new carbon materials resulted in the synthesis of novel carbon allotropes named generically graphynes. The existence of these structures were predicted by Baughman et al. in 1987 [34], but they were synthesized for the first time in 2010 by Y. Li et al. [35]. Graphynes are formed by the combination of sp and sp^2 hybridized carbon atoms according to certain periodic rules [36]. The presence of sp-hybridized carbon atoms resulted in different structures and properties when compared to graphene or CNTs. A comprehensive update on the synthesis, properties and applications of graphynes can be found in recent reviews [6,36,37].

Probably one of the least studied carbon nanomaterial despite their discovery before nanotubes and fullerenes are carbon nano-onions (CNOs) also known as multilayered fullerenes or onion-like carbons. CNOs were initially described by S. Iijima in the early 80's [38], and further rediscovered by D. Ugarte in 1992 [39]. CNOs are quasi-spherical multi-shelled fullerenes resembling the structure of an onion. The number of onion shells can be described by the series: $C_{60}@C_{240}@C_{540}@...@C_{60n^2}$, where n is the shell number and thus, they can be considered as spherical analogues of MWCNTs [40]. Depending on the preparation method, CNOs are typically 2–50 nm in diameter [41]. CNOs present interesting properties that make them suitable for different applications [42–46]. Since CNOs are the subject of the present Doctoral Thesis, a more detailed overview on their synthesis, properties, characterization, functionalization and applications will be provided in the further sections of this chapter.

1.2. Synthesis of CNOs

Historically, CNOs were prepared for the first time by S. Iijima in the 80's during an *in situ* TEM analysis of amorphous carbon films [38]. Further in the 90's, Ugarte found that carbon soots were also transformed into CNOs by intense electron-beam irradiation in TEM experiments [39]. However, both approaches did not allow to produce enough amounts of CNOs to extend their structural and physico-chemical characterization. Consequently, various studies were further published regarding to the synthesis of CNOs. Some examples of these synthetic procedures are the thermal annealing of NDs, underwater arc discharge between two graphite electrodes, pyrolysis of organic materials, ion implantation, chemical vapour deposition, electron-beam irradiation and laser irradiation and ablation [10,45,46]. Among them, thermal annealing of NDs, underwater arc discharge between graphite electrodes and pyrolysis of organic materials (Figure 1.2.1) are the most popular methods to synthesize CNOs and thus, they will be briefly described in subsequent paragraphs.

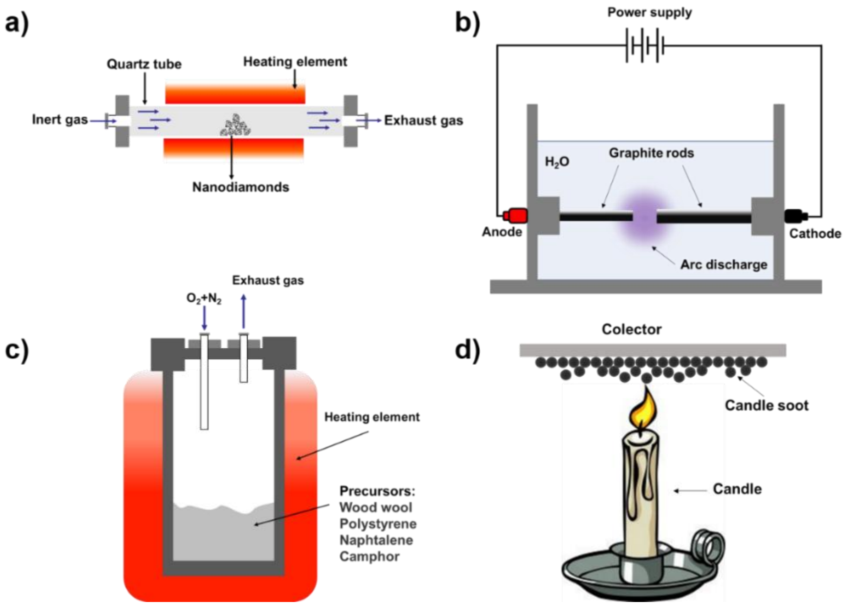

Figure 1.2.1. Schematic of the experimental setups to prepare CNOs by: a) annealing of nanodiamonds, b) underwater arc discharge and, c-d) pyrolysis of organic materials.

The thermal annealing of NDs was proposed by Kuznetsov et al. in 1994 to synthesize gram quantities of CNOs [47]. The method consists on the annealing (heating) of NDs (average diameter of 5 nm) at temperatures higher that 1100 ^{0}C in an inert atmosphere (Ar, He, N_2, and H_2) under high vacuum (Figure 1.2.1a). Under these conditions, the sp^3 hybridized carbon atoms of NDs are transformed to sp^2 hybridized ones forming curved graphene-like shells. Experimental evidence and theoretical simulations have demonstrated that this process occurs in different steps and takes place from the surface to the core of NDs [44,48–50]. The phase transformation is also connected with changes in the density, the surface area and the electrical conductivity of the annealed material as is summarized in Figure 1.2.2 [44]. The annealing of NDs allows to prepare quasi-spherical CNOs with small diameter (5-6 nm and 6-8 graphitic shells) in high yields (>80%) and in gram-scales [46]. As a result, this method has emerged as the most common approach to prepare CNOs in small and large quantities.

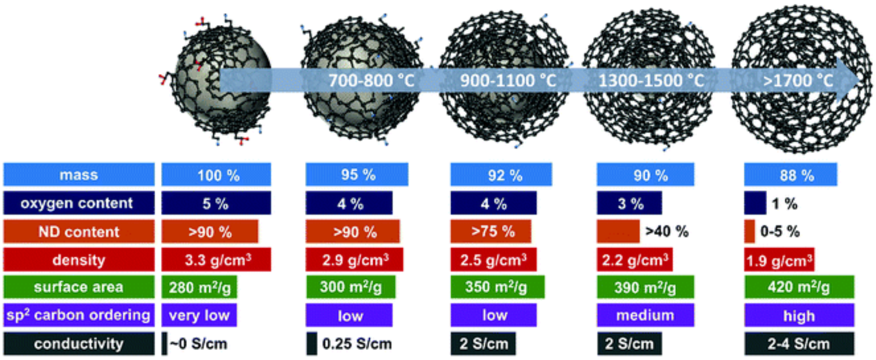

Figure 1.2.2. Schematic of the transformation from NDs to CNOs by the annealing process (top). Variation of the CNOs properties with the annealing temperature (bottom). Image reproduced from reference [44].

The underwater arc discharge between graphite electrodes method (Figure 1.2.1b) has been used to synthesize different carbon nanomaterials [51]. It was explored by Sano et. al. in 2001 to prepare CNOs in larger quantities and without using vacuum equipment [52]. This method consists in applying a direct current voltage (~16 V and ~30 A) across two high purity graphite electrodes submerged in water to generate and arc discharge (i.e. a plasma) between them [53–55]. Under these conditions, graphite is vaporized because of the plasma temperature (> 6000 K) [56], and then, the vapor is cooled down by surrounding water leading the formation of CNOs [56]. The CNOs are obtained as a floating powder on the water surface. The diameters of these CNOs are bigger than 20 nm, which correspond to approximately 30 graphene layers [57], and they can have quasi-spherical and polyhedral forms [53,58]. Additionally, other carbon particles like graphene, MWCNTs, amorphous and graphitic impurities are also formed [58]. This issue requires some sort of posterior purification/separation process that limit the practical applications of this method [54].

The pyrolysis of organic matters is a more recent strategy to prepare larger amount of CNOs. There are two approaches: i) pyrolysis of wood wool in a muffle furnace under a flow of N_2:O_2 (95:5) gas mixture (Figure 1.2.1c) [59], and ii) the open-flame pyrolysis of organic precursors also known as candle soot method (Figure 1.2.1d) [60]. A wide variety of organic precursors have been used like lycopene [61], rice husk [62], naphthalene [63], polymers [64,65] vegetal oils [66] and waste tyres [67]. In both approaches, the organic precursor is decomposed into atomic or radical fragments that leads the formation of graphite-like structures [68]. These structures nucleate and self-curl promoting the growth of CNOs from inside-out like the snowball accreting process [66,69]. The CNOs prepared following these methods are quasi-spherical and have diameters between 15-60 nm.

1.3. Characterization of CNOs

Several techniques can be employed to characterize the surface and structural properties of CNOs. High resolution transmission electron microscopy (HRTEM), Raman spectroscopy, X-ray diffraction (XRD) and N_2 isothermal adsorption are used for structural characterization. Nuclear magnetic resonance, Fourier-transformed infrared spectroscopy (FTIR), X-ray photoemission spectroscopy (XPS), ultraviolet photoelectron spectroscopy (UPS), and thermogravimetric analysis are employed to study the chemical composition of CNOs. Electron paramagnetic resonance spectroscopy, scanning tunneling microscopy and electrochemical techniques are useful to study the electrical and electrochemical properties of CNOs. In this section, we will briefly comment the techniques used in this work to characterize the CNOs.

HRTEM is very useful to clearly visualize the structural features of CNOs and to study its mechanism of formation [44]. Figure 1.3.1 show HRTEM images of CNOs prepared by thermal annealing of NDs [70], pyrolysis of wood wool [71], and underwater arc discharge methods [58]. Quasi-spherical multi-shell structures are observed in the case of CNOs prepared by thermal annealing and pyrolysis methods. In contrast, polygonal CNOs are obtained by the underwater arc discharge method. Another feature that can be extracted from HRTEM are the distances between lattice fringes. For CNOs show in Figure 1.3.1, the distances are 0.34-0.37, 0.34-0.22 and 0.35-0.37 nm, respectively. These values are very close to the distance between two (002) planes of graphite indicating the basic graphitic structure of CNOs [72].

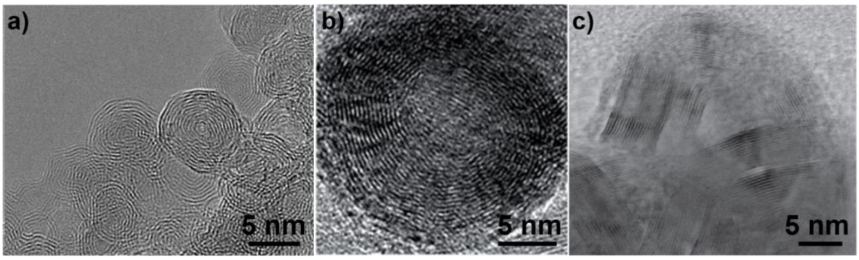

Figure 1.3.1. HRTEM images of CNOs obtained by a) annealing of NDs [70], b) pyrolysis of wood wool [71], and c) underwater arc discharge method [58].

Raman spectroscopy is a routine technique to characterize carbon materials [73]. This technique has been used systematically as a tool for characterization of CNOs to mainly distinguish the different structures that originate during their synthesis, to corroborate the graphitic-like structure of CNOs, and to detect the presence of structural defects [41,74,75]. Figure 1.3.2a shows Raman spectra of CNOs prepared by annealing of NDs at different temperatures [76].

It is observed that the Raman spectrum of CNOs contain three main bands. These three bands are also observed in the spectrum of graphite and graphene confirming the basic graphitic structure of CNOs [77]. The first two bands located at about 1580 and 1350 cm^{-1} are the G and D band, respectively [74]. The G band corresponds to the in-plane stretching mode E_{2g} of carbon atoms in sp^2-hybridized networks. The D band is due to the A_{1g} breathing mode of six-atom rings in disordered structure [77]. The D band is always present in curved carbon nanostructures like CNTs and CNOs. The third band located near 2700 cm^{-1} is the 2D band and corresponds to a two-phonon process involving phonons with opposite wave vectors [74]. The 2D band offers complementary information about the arrangement of the different layers on CNOs [74]. The full width at half maximum (FWHM) of the D and G bands and their intensity ratio (I_D/I_G) are used as criteria to assess the degree of defect and functionalization of CNOs. From Figure 1.3.2b, it is observed that the FWHM and the I_D/I_G ratio decreases with an increase of the annealing temperature indicating a higher structural order. On the other hand, the covalent functionalization of CNOs increases the I_D/I_G ratios due to the increase of sp^3- hybridized carbon atoms on the surface of CNOs [43].

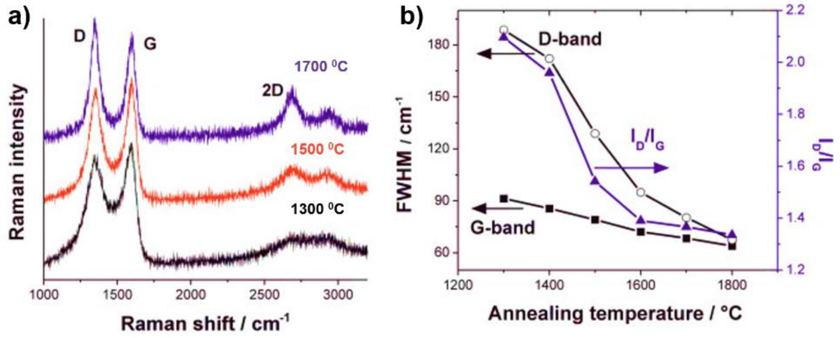

Figure 1.3.2. a) Raman spectra of CNOs prepared at different temperatures, and b) calculated D and G band line width and their corresponding I_D/I_G ratios. Images taken from reference [76].

X-ray photoelectron spectroscopy (XPS) and ultraviolet photoelectron spectroscopy (UPS) are two valuable techniques to extract the chemical composition and the electronic structure of a material, respectively. In the case of CNOs, XPS is extensively used to identify the different functional groups on the CNOs surface at each step of their synthesis or the new ones introduced by chemical functionalization [78–83]. Figure 1.3.3a shows the high-resolution XPS C 1s spectra of CNOs prepared by annealing of NDs at 1750 ^{0}C [82]. The deconvolution of the spectrum allows to identify the presence of sp^2 and sp^3 hybridized carbon atoms as well as of different oxygen-containing groups. In contrast, the UPS studies of CNOs are scarce and have mainly focused on studying how the annealing temperature used during their synthesis from NDs affects the electronic structure of the resulting CNOs [80,81,84,85].

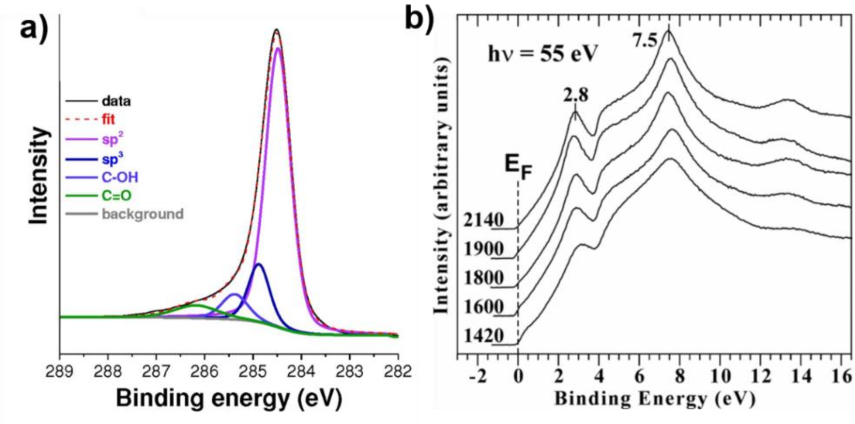

Figure 1.3.3. a) High-resolution XPS C 1s spectra of CNOs prepared by annealing of NDs at 1750 ^{0}C and, b) UPS spectra of CNOs prepared at different annealing temperatures. Images taken from references [82] and [81], respectively.

Figure 1.3.3b illustrates the UPS spectra of CNOs obtained at different temperatures [81]. The main features are the signals at about 3, 4 and 7 eV. These correspond to the π, mixed π-σ, and σ states of CNOs, respectively. These features are similar to those of graphite and CNTs [86,87]. Moreover, the non-zero intensity at the Fermi Level indicates that the CNOs have a metallic-like electronic structure. A more detailed discussion on XPS and UPS of CNOs will be provided in Chapter 3.

1.4. Functionalization of CNOs

Analogous to other carbon materials, CNOs display poor dispersibility in both aqueous and organic solvents. This is due to the tendency of CNOs to form aggregates as a result of strong interparticle interactions. To overcome this tendency, covalent or non-covalent functionalization of the outer shells of CNOs are the methods of choice. Since the structure of CNOs (sp^2-hybridized carbon atoms network) is similar to that of CNTs, the same strategies used for the functionalization of CNTs can be applied to CNOs. A detailed description and examples of all these strategies can be found in references [43], [88] and [89]. Thus, here we will just comment some of them that we considered the most versatile (Figure 1.4.1).

Probably the simplest approach to functionalize CNOs is the oxidation of their outer shells. In general, oxidation is used as the first step for further chemical modifications of CNOs and to produce particles that are well dispersible in many polar solvents including water [90]. The oxidation of CNOs is achieved by chemical oxidation with oxidant acids such as HNO_3 or a mixture of HNO_3 and H_2SO_4 in a 1:3 volume ratio [57,91–93], and by chemical activation using concentrate KOH solutions [94]. Oxidation of CNOs by electrochemical methods is also possible [95]. All these treatments introduce different oxygen-containing functional groups on the surface of the CNOs, such as aldehydes, ketones, esters, alcohols, and carboxylic acids [90]. On the other hand, chemical oxidation is a harsh process that introduces defects on the graphitic shells that disrupt the π-conjugation and might result in the loss of the structural integrity of CNOs [94,96,97]. A less aggressive oxidation can be done by ozonolysis of CNOs. This process does not result in any damage to the structure of the CNOs while introducing similar oxygen-containing groups as acid oxidation does [98]. More recently, our group reported the oxidation of CNOs by an Ar/O_2 radio frequency plasma [78]. Following this procedure, ketone and phenolic groups were preferentially introduced in the CNOs outer shells without significative structural damages.

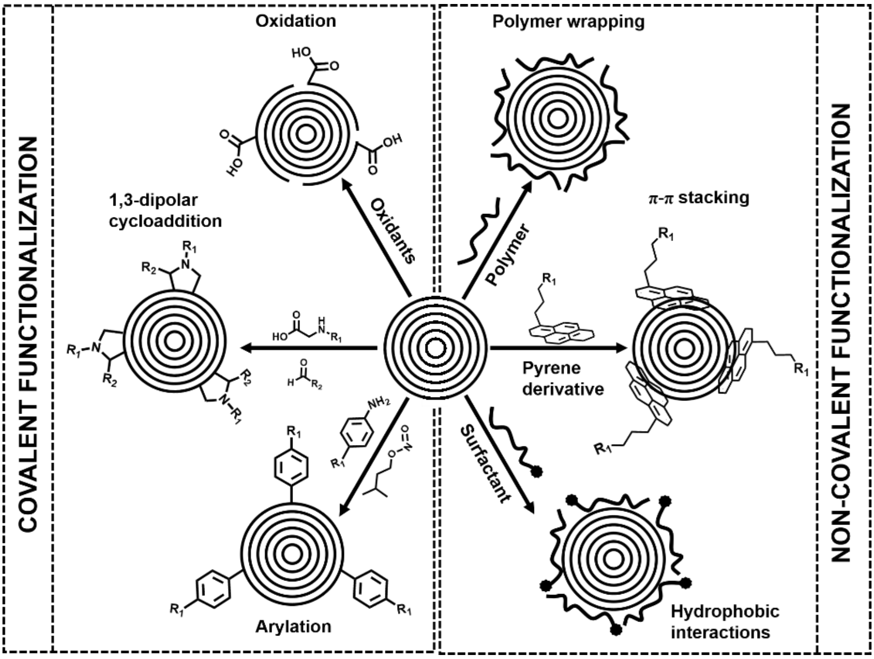

Figure 1.4.1. Some synthetic strategies for the functionalization of CNOs: chemical oxidation [57,91–93], 1,3-dipolar cycloaddition of azomethine ylides [99,100], radical addition of diazonium salts [101], polymer wrapping [93,102–105], π-π stacking with pyrene derivatives [106], and hydrophobic interaction with surfactants [89,107,108].

One of the first reported synthetic procedures to functionalize CNOs was the 1,3-dipolar cycloaddition of azomethine ylides developed by

Prato's group [99] and further extended by Echegoyen's group [100]. In general, this procedure consists on reacting under reflux the CNOs with an aldehyde and an N-substituted glycine derivative. The product is a pyrrolidine functionalized CNOs that are more dispersible in different solvents than pristine CNOs. Other cycloaddition approaches have been reported to functionalize CNOs like the Bingel-Hirsch cyclopropanation [57] and the cycloaddition of nitrenes [109].

Aryl group can be attached to the CNOs surface by radical addition to obtain dispersible CNOs. In this case, the most common approach is the radical addition of diazonium salts, known as Tour reaction [101]. In this method, CNOs are dispersed in a suitable solvent and then the aniline derivative and isoamyl nitrite are subsequently added to generate, in situ, the corresponding diazonium salt. Following this approach, bromides, benzoic acids, *tert*-butyl, nitro, methyl esters, and trimethylsilyl acetylenes functional groups were attached to the surface of CNOs. More recently, our group used this approach to attach 4-aminobenzo-18-crown-6 ether moieties to the surface of CNOs [110]. The modified CNOs formed stable dispersions in water in the presence of aminated carboxymethyl cellulose or poly-L-lysine because of non-covalent interactions between the positive charged ammonium groups in the polymers and the oxygen atoms in the crown ether.

Non-covalent functionalization of CNOs is another approach to improve the dispersibility in different solvents without disrupting the electronic structure of CNOs. The current understanding and developments in non-covalent approaches to surface modification of CNOs have been recently reviewed by Bartkowski and Giordani [89]. The non-covalent interactions used for CNOs functionalization include electrostatic interactions, van der Waal forces, and π interactions (Figure 1.4.2).

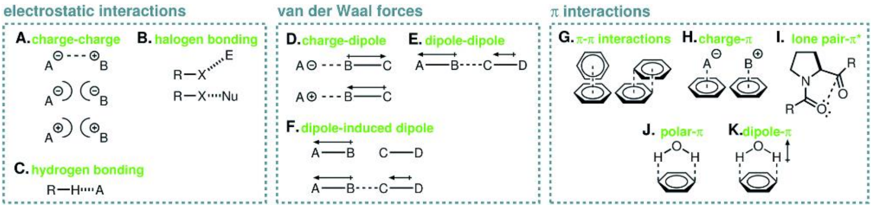

Figure 1.4.2. Common non-covalent interactions that may be utilized in the non-covalent functionalization of CNOs. Image taken from reference [89].

The first example of non-covalent functionalization of CNOs consisted in the complexation between a zinc tetraphenyl porphyrin and pyridyl functionalized CNOs [93]. This CNOs-porphyrin hybrid showed possible applications in catalysis and hydrogen storage. Polymer wrapping is another approach for non-covalent functionalization of CNOs. Poly(3,4-ethylene-dioxythiophene), poly(styrenesulfonate), poly(ethylene glycol), polysorbate 20, poly(4-vinylpyridine-co-styrene), poly(diallyldimethylammonium chloride), chitosan and poly(vinyl alcohol) have been used to prepare supramolecular systems with CNOs [93,102–105]. Overall, these CNOs/polymer systems showed enhanced water dispersibility and were suitable for supercapacitors, (bio)sensing and drug delivery applications.

Our group has demonstrated the possibility to prepare stable aqueous dispersion of CNOs through host-guest non covalent interactions between β-cyclodextrin modified CNOs and ferrocene grafted dextran polymer [111], and also through crown ether/ammonium interactions between 4-aminobenzo-18-crown-6 ether modified CNOs and aminated carboxymethyl cellulose or poly-L-lysine [110]. Non-covalent π-π interactions of pyrene derivatives and the CNOs surface have been used for cell imaging and cell internalization pathway elucidation. In this example, a soluble CNOs-based supramolecular system with fluorescent properties was prepared by reacting pristine CNOs and pyrene-BODIPY dyad fluorophore, whereby the pyrene moiety of the dyad was π–π stacked onto the CNOs surface [106]. Cationic, anionic and non-ionic surfactants can be used for non-covalent functionalization of CNOs. Sodium dodecyl sulfate (SDS), sodium dodecyl benzene sulfonate (SDBS), hexadecyltrimethylammonium bromide (CTAB), 4-(1,1,3,3-tetramethylbutyl)phenyl-polyethylene glycol (Triton X-100), and polyethylene glycol sorbitan monolaurate (Tween 20) have been investigated to disperse CNOs in water [107]. These studies revealed that these surfactants adsorb onto the CNOs surface, resulting in stable and well dispersed CNOs/surfactant composites [89]. A recent study demonstrated that anionic surfactants show the best ability to create stable CNOs dispersions, with SDBS exhibiting superior efficacy [108].

1.5. Application of CNOs

In the recent years, many potential applications of CNOs have been proposed including energy storage [44], photovoltaic cells [112], lubricants [113], catalysis [114], and biomedical applications [42,105]. A more wide overview on CNOs application can be found in various reviews [6,7,42–46]. These applications are the result of a combination of electronic (high conductivity) and interfacial (high area-to-volume ratio) properties and illustrate that CNOs are very attractive nanomaterials with a wide range of potential applications still to be explored or are at the fundamental research level. This is the case of electrochemical (bio)sensing applications where the studies incorporating CNOs are scarce with less than 20 articles in a decade. Since a half of this thesis is devoted to electrochemical (bio)sensing applications of CNOs, some of these articles will be commented in the following paragraphs.

Small molecules with biological interest like dopamine, epinephrine and norepinephrine have been detected by using CNOs/polymer composites or pristine CNOs cast on glassy carbon electrodes (GCE) [103,115,116]. The results indicated that the electrochemical performance of sensors containing CNOs showed higher sensitivity, higher selectivity and more stable electrode responses than other carbon materials like MWCNTs, graphite nanoflakes, and glassy carbon [115]. In another example developed by our group, CNOs were deposited on GC surfaces followed by electrochemical grafting of o-aminophenol or physical adsorption of thionine to detect nitrite ions and ascorbic acid in aqueous solution and in real samples, such as orange juice. The sensors incorporating CNOs showed enhanced sensitivity and a lower detection limit that those without CNOs [117]. More recently, the electrochemical detection of Fentanyl (a pain reliever stronger and deadlier than heroin) was addressed by casting CNOs on GCE. The electrochemical studies indicated the sensor was capable of the voltammetric determination of traces of Fentanyl with no influences in the current responses in the presence of common interferents with 100-fold concentrations [118]. Similarly, the simultaneous detection of carcinogenic substances like the dihydroxybenzene (DHB) isomers was reported by using nitrogen-doped CNOs (Figure 1.5a). The authors stated that the sensor showed approximately 1000-times better electrocatalytic performance and outperformed the Au, Ag, Pd, metal organic frameworks, conventional carbon allotropes, including their various composites in determining the DHB isomers with the ultrahigh sensitivity and ultralow detection limit [119].

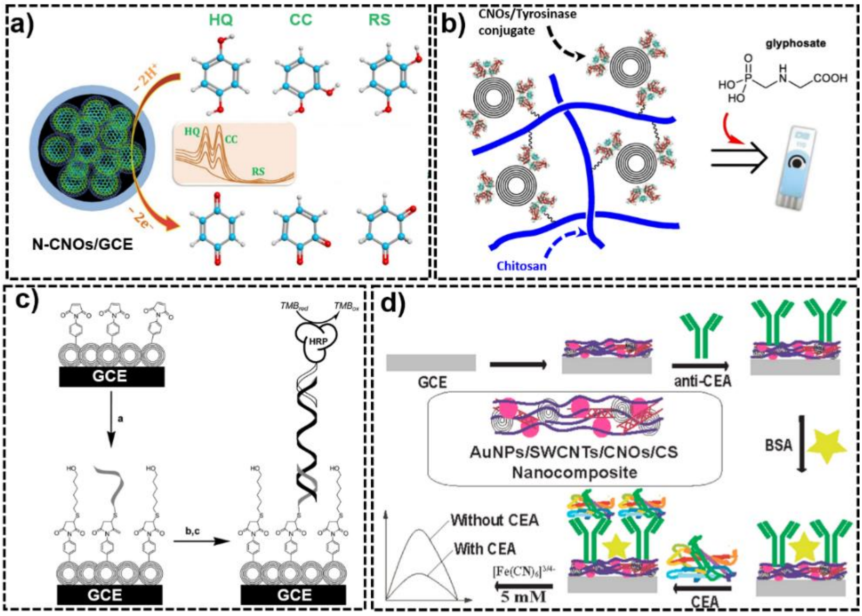

Figure 1.5. Schematic representation of some electrochemical (bio)sensor architectures incorporating CNOs: a) to detect small electroactive molecules [119], b) enzymatic glyphosate biosensor [120], c) human papillomavirus genosensor [121], and d) label-free immunosensor for carcinoembryonic antigen [122]. N-CNOs : nitrogen doped CNOs, HQ: hydroquinone, CC: catechol, RS: resorcinol, TMB: 3,3',5,5'-tetramethylbenzidine, HRP: horseradish peroxidase, and BSA: bovine serum albumin.

In the case of enzymatic sensors, a hybrid nanocomposite of CNOs/Nafion®/glucose oxidase was reported to detect glucose under physiological conditions. In the same work, Pt nanoparticles decorated on CNOs have also shown to possess an excellent catalytic activity for glucose oxidation [123]. Recently, in a work developed by our group, a biosensor for glyphosate (a carcinogenic pesticide) was described which consisted of a CNOs/tyrosinase conjugate immobilized in a chitosan (CS) matrix on a screen-printed electrode (Figure 1.5b). The sensor was applied to the detection of glyphosate in water and soil samples taken from irrigation of a rice field after aerial application. Results were in good agreement with data obtained by a commercial ELISA kit to detect glyphosate [120].

The incorporation of CNOs in sensors has also demonstrated advantages to detecting electrochemically more complex molecules like DNA sequences and proteins. Our group reported the amperometric detection of a DNA sequence associated with the human papillomavirus (HPV) by using CNOs (Figure 1.5c). In this work, CNOs were cast on GCE and further modified by electrografting of diazonium salts to attach the capture DNA probe on the CNOs surface. It was demonstrated that the incorporation of CNOs resulted in better sensitivities (~ four times) and lower limits of detection as compared to a GCE electrode without CNOs [121]. More recently, a nanocomposite of gold nanoparticles (AuNPs), CNOs, SWCNTs and CS (AuNPs/CNOs/SWCNTs/CS) was prepared to develop a “label-free” electrochemical immunosensor to detect the carcinoembryonic antigen (CEA), a clinical tumor marker (Figure 1.5d) [122]. The same group also reported an electrochemical immunosensor to detect human chorionic gonadotropin (hCG), a biomarker related to hydatid pregnancy, trophoblastic cancer and orchic teratoma. The immunosensor incorporated a nanocomposite of CNOs, AuNPs and polyethylene glycol to bind the recognition element, anti-hCG antibodies, by electrostatic and physical adsorption [124]. Both immunosensors showed wide linear ranges and detection limits of their respective analytes in the fg mL^{-1} order without significative interference caused by other antigens presented in real samples.

All these platforms can also be extended or used as inspiration to design highly selective and sensitive (bio)sensors to detect other molecules or clinically important biomarkers as it will be illustrated in the further chapters of this thesis.

1.6. Thesis objective

Nanomaterials based on carbon allotropes have gained significant attention in the last three decades. Carbon allotropes possess unique properties leading to unprecedented functions with numerous applications.

As described in the preceding sections, CNOs present very interesting properties which makes them promising materials to develop novel electrocatalytic systems and electrochemical (bio)sensors with improved analytical performance. Although, more understanding on CNOs properties must be obtained in order to realize their high potential to the maximum.

The overall objective of this thesis is thus to prepare and characterize surfaces modified with carbon nano-onions to develop electrocatalytic systems and (bio)sensors for biomedical and environmental applications.

To achieve this general objective, we have focused on the following aspects:

-To study the dispersion of CNOs in different organic solvents.

-To elucidate the electronic structure of CNOs and the effect of the oxidation treatments on it.

-To modify electrode surfaces with dispersions of pristine and oxidized CNOs to form films and to perform their electrochemical characterization.

-To post-functionalize CNOs modified surfaces with polycatecholamines and to perform their electrochemical characterization.

-To apply the CNOs and CNOs/polycatecholamines modified electrodes to develop electrochemical (bio)sensors to detect small molecules like ascorbic acid, dopamine, uric acid, hydrogen peroxide, oxygen and also antibodies like IgA.

This thesis is thus a contribution to the general understanding of the relationship between electronic structure, properties and applications of CNOs and an attempt to expand the current knowledge on these materials and open new application possibilities in areas such as electrochemical energy storage and electroanalytical methods.

References

[1] http://www.caer.uky.edu/carbon/history/carbonhistory.shtml (accessed:26/05/2020).
[2] https://www.bp.com/en/global/corporate/energy-economics/statistical-review-of-world-energy.html (accessed May 27, 2020).

[3] J. Zhang, M. Terrones, C.R. Park, R. Mukherjee, M. Monthioux, N. Koratkar, Y.S. Kim, R. Hurt, E. Frackowiak, T. Enoki, Y. Chen, Y. Chen, A. Bianco, *Carbon science in 2016: Status, challenges and perspectives*, Carbon 98 (2016) 708–732.

[4] M. Rahaman, D. Khastgir, A.K. Aldalbahi, Carbon-containing polymer composites, 1st ed., Springer, Singapore, Singapore, 2019.

[5] B.I. Kharisov, O.V. Kharissova, Carbon allotropes: metal-complex chemistry, properties and applications, 1st ed., Springer, Cham, 2019.

[6] V. Georgakilas, J.A. Perman, J. Tucek, R. Zboril, *Broad family of carbon nanoallotropes: classification, chemistry, and applications of fullerenes, carbon dots, nanotubes, graphene, nanodiamonds, and combined superstructures*, Chem. Rev. 115 (2015) 4744–4822.

[7] T. Laurila, S. Sainio, M. Caro, *Hybrid carbon based nanomaterials for electrochemical detection of biomolecules*, Prog. Mater. Sci. 88 (2017) 499–594.

[8] M. Notarianni, J. Liu, K. Vernon, N. Motta, *Synthesis and applications of carbon nanomaterials for energy generation and storage*, Beilstein J. Nanotechnol. 7 (2016) 149–196.

[9] D. Tománek, Guide through the nanocarbon jungle, 1st ed., Morgan & Claypool, San Rafael, CA, 2014.

[10] K.D. Sattler, Carbon nanomaterials sourcebook. Volume 1, Graphene, fullerenes, nanotubes, and nanodiamonds, 1st ed., CRC Press, 2016.

[11] H.W. Kroto, J.R. Heath, S.C. O’Brien, R.F. Curl, R.E. Smalley, *C_{60}: Buckminsterfullerene*, Nature. 318 (1985) 162–163.

[12] A. Hirsch, Principles of fullerene reactivity, in: A. Hirsch (Ed.), Fullerenes Relat. Struct., Springer, Berlin, Heidelberg, 1999: pp. 1–65.

[13] J.L. Delgado, M.Á. Herranz, N. Martín, *The nano-forms of carbon*, J. Mater. Chem. 18 (2008) 1417–1426.

[14] H. Singh, M. Srivastava, *Fullerenes: Synthesis, separation, characterization, reaction chemistry, and applications—A review*, Energy Sources. 17 (1995) 615–640.

[15] J. Coro, M. Suárez, L.S.R. Silva, K.I.B. Eguiluz, G.R. Salazar-Banda, *Fullerene applications in fuel cells: A review*, Int. J. Hydrogen Energy. 41 (2016) 17944–17959.

[16] S. Iijima, T. Ichihashi, *Single-shell carbon nanotubes of 1-nm diameter*, Nature. 363 (1993) 603–605.

[17] S. Iijima, *Helical microtubules of graphitic carbon*, Nature. 354 (1991) 56–58.

[18] L.V. Radushkevich, V.M. Lukyanovich, *O strukture ugleroda, obrazujucegosja pri termiceskom razlozenii okisi ugleroda na zeleznom kontakte*, Zurn Fis. Chim. 26 (1952) 88–95.

[19] M. Monthioux, V.L. Kuznetsov, *Who should be given the credit for the discovery of carbon nanotubes?*, Carbon. 44 (2006) 1621–1623.

[20] K. Hata, D.N. Futaba, K. Mizuno, T. Namai, M. Yumura, S. Iijima, *Water-assisted highly efficient synthesis of impurity-free single-walled carbon nanotubes*, Science. 306 (2004) 1362–1364.

[21] P.M. Ajayan, *Nanotubes from carbon*, Chem. Rev. 99 (1999) 1787–1799.

[22] M.S. Dresselhaus, R.E. Smalley, G. Dresselhaus, P. Avouris, Carbon nanotubes synthesis, structure, properties, and applications, 1st ed., Springer Berlin, 2014.

[23] K. Tanaka, S. Iijima, Carbon nanotubes and graphene, 2nd ed., Elsevier Inc., 2014.

[24] V. V. Danilenko, *On the history of the discovery of nanodiamond synthesis*, Phys. Solid State. 46 (2004) 595–599.

[25] V.N. Mochalin, O. Shenderova, D. Ho, Y. Gogotsi, *The properties and applications of nanodiamonds*, Nat. Nanotechnol. 7 (2012) 11–23.

[26] S. Kumar, M. Nehra, D. Kedia, N. Dilbaghi, K. Tankeshwar, K.-H. Kim, *Nanodiamonds: Emerging face of future nanotechnology*, Carbon. 143 (2019) 678–699.

[27] K.S. Novoselov, A.K. Geim, S. V. Morozov, D. Jiang, Y. Zhang, S. V. Dubonos, I. V. Grigorieva, A.A. Firsov, *Electric field in atomically thin carbon films*, Science. 306 (2004) 666–669.

[28] P.R. Wallace, *The band theory of graphite*, Phys. Rev. 71 (1947) 622–634.

[29] H.P. Boehm, A. Clauss, G.O. Fischer, U. Hofmann, *Dünnste Kohlenstoff-Folien*, Zeitschrift Für Naturforsch. B. 17 (1962) 150–153.

[30] Y. Zhu, H. Ji, H.-M. Cheng, R.S. Ruoff, *Mass production and industrial applications of graphene materials*, Natl. Sci. Rev. 5 (2017) 90–101.

[31] P. Solís-Fernández, M. Bissett, H. Ago, *Synthesis, structure and applications of graphene-based 2D heterostructures*, Chem. Soc. Rev. 46 (2017) 4572–4613.

[32] S. Szunerits, R. Boukherroub, A. Downard, J.J. Zhu, Nanocarbons for electroanalysis, 1st ed., John Wiley & Sons, Ltd, Chichester, UK, 2017.

[33] P. Bhagabati, M. Rahaman, S. Bhandari, I. Roy, A. Dey, P. Gupta, M.A. Ansari, A. Dutta, D. Chattopadhyay, Synthesis/preparation of carbon materials, in: Carbon-Containing Polym. Compos., 1st ed., Springer, Singapore, 2019: pp. 1–64.

[34] R.H. Baughman, H. Eckhardt, M. Kertesz, *Structure-property predictions for new planar forms of carbon: Layered phases containing sp^2 and sp atoms*, J. Chem. Phys. 87 (1987) 6687–6699.

[35] G. Li, Y. Li, H. Liu, Y. Guo, Y. Li, D. Zhu, *Architecture of graphdiyne nanoscale films*, Chem. Commun. 46 (2010) 3256–3258.

[36] X. Gao, H. Liu, D. Wang, J. Zhang, *Graphdiyne: synthesis, properties, and applications*, Chem. Soc. Rev. 48 (2019) 908–936.

[37] Q. Peng, J. Crean, L. Han, S. Liu, X. Wen, S. De, A. Dearden, *New materials graphyne, graphdiyne, graphone, and graphane: review of properties, synthesis, and application in nanotechnology*, Nanotechnol. Sci. Appl. 7 (2014) 1.

[38] S. Iijima, *Direct observation of the tetrahedral bonding in graphitized carbon black by high resolution electron microscopy*, J. Cryst. Growth. 50 (1980) 675–683.

[39] D. Ugarte, *Curling and closure of graphitic networks under electron-beam irradiation*, Nature. 359 (1992) 707–709.

[40] V.Z. Mordkovich, *The observation of large concentric shell fullerenes and fullerene-like nanoparticles in laser pyrolysis carbon blacks*, Chem. Mater. 12 (2000) 2813–2818.

[41] D. Roy, M. Chhowalla, H. Wang, N. Sano, I. Alexandrou, T.. Clyne, G.A. Amaratunga, *Characterisation of carbon nano-onions using Raman spectroscopy*, Chem. Phys. Lett. 373 (2003) 52–56.

[42] A. Camisasca, S. Giordani, *Carbon nano-onions in biomedical applications: Promising theranostic agents*, Inorganica Chim. Acta. 468 (2017) 67–76.

[43] J. Bartelmess, S. Giordani, *Carbon nano-onions (multi-layer*

fullerenes): chemistry and applications, Beilstein J. Nanotechnol. 5 (2014) 1980–1998.

[44] M. Zeiger, N. Jäckel, V.N. Mochalin, V. Presser, *Review: carbon onions for electrochemical energy storage*, J. Mater. Chem. A. 4 (2016) 3172–3196.

[45] O. Mykhailiv, H. Zubyk, M.E. Plonska-Brzezinska, *Carbon nano-onions: unique carbon nanostructures with fascinating properties and their potential applications*, Inorganica Chim. Acta. 468 (2017) 49–66.

[46] M.E. Plonska-Brzezinska, *Carbon nano-onions: a review of recent progress in synthesis and applications*, ChemNanoMat. 5 (2019) 568–580.

[47] V.L. Kuznetsov, A.L. Chuvilin, Y. V. Butenko, I.Y. Malkov, V.M. Titov, *Onion-like carbon from ultra-disperse diamond,* Chem. Phys. Lett. 222 (1994) 343–348.

[48] L. Hawelek, A. Brodka, S. Tomita, J.C. Dore, V. Honkimäki, A. Burian, *Transformation of nano-diamonds to carbon nano-onions studied by X-ray diffraction and molecular dynamics,* Diam. Relat. Mater. 20 (2011) 1333–1339.

[49] A. Bródka, T.W. Zerda, A. Burian, *Graphitization of small diamond cluster - Molecular dynamics simulation*, Diam. Relat. Mater. 15 (2006) 1818–1821.

[50] J.M. Leyssale, G.L. Vignoles, *Molecular dynamics evidences of the full graphitization of a nanodiamond annealed at 1500 K*, Chem. Phys. Lett. 454 (2008) 299–304.

[51] L. Hernandez-Tabares, S. Fortune-Fabregas, F.J. Chao-Mujica, J.G. Darias-Gonzalez, N. Torres-Figueredo, E. Reguera, L.F. Desdin-Garcia, *Multiparametric diagnostic in the synthesis of carbon nanostructures via submerged arc discharge: Stability, nucleation and yield,* J. Appl. Phys. 126 (2019) 183301.

[52] N. Sano, H. Wang, M. Chhowalla, I. Alexandrou, G.A.J. Amaratunga, *Synthesis of carbon "onions" in water*, Nature. 414 (2001) 506–507.

[53] Y. Zheng, P. Zhu, *Carbon nano-onions: Large-scale preparation, functionalization and their application as anode material for rechargeable lithium ion batteries*, RSC Adv. 6 (2016) 92285–92298.

[54] R. Borgohain, J. Yang, J.P. Selegue, D.Y. Kim, *Controlled synthesis, efficient purification, and electrochemical characterization of arc-discharge carbon nano-onions,*

Carbon. 66 (2014) 272–284.

[55] J. Darias, E. Carrillo, J. Arteche, L. Hernández, M. Ramos, L. Desdín, *Submerged arc discharge system for the synthesis of multi-layer carbon nanoonions*, Rev. Cuba. Física. 28 (2011) 1e80-1e84.

[56] H. Lange, M. Sioda, A. Huczko, Y.Q. Zhu, H.W. Kroto, D.R.M. Walton, *Nanocarbon production by arc discharge in water*, Carbon. 41 (2003) 1617–1623.

[57] A. Palkar, F. Melin, C.M. Cardona, B. Elliott, A.K. Naskar, D.D. Edie, A. Kumbhar, L. Echegoyen, *Reactivity differences between carbon nano onions (CNOs) prepared by different methods*, Chem. An Asian J. 2 (2007) 625–633.

[58] F. Alessandro, A. Scarcello, M.D. Basantes Valverde, D.C. Coello Fiallos, S.M. Osman, A. Cupolillo, M. Arias, O. Arias de Fuentes, G. De Luca, A. Aloise, E. Curcio, G. Nicotra, C. Spinella, L.S. Caputi, *Selective synthesis of turbostratic polyhedral carbon nano-onions by arc discharge in water*, Nanotechnology. 29 (2018) 325601-325611.

[59] M. Ghosh, S.K. Sonkar, M. Saxena, S. Sarkar, *Carbon nano-onions for imaging the life cycle of Drosophila melanogaster*, Small. 7 (2011) 3170–3177.

[60] M.R. Mulay, A. Chauhan, S. Patel, V. Balakrishnan, A. Halder, R. Vaish, *Candle soot: Journey from a pollutant to a functional material*, Carbon. 144 (2019) 684–712.

[61] V. Singh, *Natural source derived carbon nano-onions as electrode material for sensing applications*, Diam. Relat. Mater. 87 (2018) 202–207.

[62] H. Jin, S. Wu, T. Li, Y. Bai, X. Wang, H. Zhang, H. Xu, C. Kong, H. Wang, *Synthesis of porous carbon nano-onions derived from rice husk for high-performance supercapacitors*, Appl. Surf. Sci. 488 (2019) 593–599.

[63] M. Choucair, J.A. Stride, *The gram-scale synthesis of carbon onions*, Carbon. 50 (2012) 1109–1115.

[64] P. Dubey, K.M. Tripathi, S.K. Sonkar, *Gram scale synthesis of green fluorescent water-soluble onion-like carbon nanoparticles from camphor and polystyrene foam*, RSC Adv. 4 (2014) 5838-5844.

[65] P. Dubey, D. Muthukumaran, S. Dash, R. Mukhopadhyay, S. Sarkar, *Synthesis and characterization of water-soluble carbon nanotubes from mustard soot*, Pramana. 65 (2005) 681–697.

[66] T.H. Mongwe, B.J. Matsoso, B.K. Mutuma, N.J. Coville, M.S. Maubane, *Synthesis of chain-like carbon nano-onions by a flame assisted pyrolysis technique using different collecting plates*, Diam. Relat. Mater. 90 (2018) 135–143.

[67] M. Bhaumik, K. Raju, I. Arunachellan, T. Ludwig, M.K. Mathe, A. Maity, S. Mathur, *High-performance supercapacitors based on S-doped polyaniline nanotubes decorated with* $Ni(OH)_2$ *nanosponge and onion-like carbons derived from used car tyres*, Electrochim. Acta. 342 (2020) 136111.

[68] B. XU, *Prospects and research progress in nano onion-like fullerenes*, New Carbon Mater. 23 (2008) 289–301.

[69] V. Dhand, J.S. Prasad, M.V. Rao, S. Bharadwaj, Y. Anjaneyulu, P.K. Jain, *Flame synthesis of carbon nano onions using liquefied petroleum gas without catalyst*, Mater. Sci. Eng. C. 33 (2013) 758–762.

[70] Y.-J. Ko, K. Choi, J.-Y. Kim, I. Kim, D.S. Jeong, H.-J. Choi, H. Mizuseki, W.-S. Lee, *Onion-like carbon as dopant/modification-free electrocatalyst for* $[VO]^{2+}/[VO_2]^{+}$ *redox reaction: Performance-control mechanism*, Carbon N. Y. 127 (2018) 31–40.

[71] S.K. Sonkar, M. Roy, D.G. Babar, S. Sarkar, *Water soluble carbon nano-onions from wood wool as growth promoters for gram plants*, Nanoscale. 4 (2012) 7670.

[72] R. Bacon, *Growth, structure, and properties of graphite whiskers*, J. Appl. Phys. 31 (1960) 283–290.

[73] Puech, Kandara, Paredes, Moulin, Weiss-Hortala, Kundu, Ratel-Ramond, Plewa, Pellenq, Monthioux, *Analyzing the Raman spectra of graphenic carbon materials from kerogens to nanotubes: what type of information can be extracted from defect bands?*, C — J. Carbon Res. 5 (2019) 69.

[74] D. Codorniu Pujals, O. Arias de Fuentes, L.F. Desdín García, E. Cazzanelli, L.S. Caputi, *Raman spectroscopy of polyhedral carbon nano-onions*, Appl. Phys. A. 120 (2015) 1339–1345.

[75] J. Cebik, J.K. McDonough, F. Peerally, R. Medrano, I. Neitzel, Y. Gogotsi, S. Osswald, *Raman spectroscopy study of the nanodiamond-to-carbon onion transformation*, Nanotechnology. 24 (2013) 205703.

[76] J.K. McDonough, A.I. Frolov, V. Presser, J. Niu, C.H. Miller, T. Ubieto, M. V. Fedorov, Y. Gogotsi, *Influence of the structure of carbon onions on their electrochemical*

performance in supercapacitor electrodes, Carbon. 50 (2012) 3298–3309.

[77] A. Jorio, R. Saito, G. Dresselhaus, M.S. Dresselhaus, Raman spectroscopy in graphene related systems, Wiley-VCH, Weinheim, Germany, 2011.

[78] J.P. Bartolome, A. Fragoso, *Preparation and characterization of carbon nano-onions by nanodiamond annealing and functionalization by radio-frequency Ar/O_2 plasma*, Fullerenes, Nanotub. Carbon Nanostructures. 25 (2017) 327–334.

[79] Y. Lin, Y. Zhu, B. Zhang, Y.A. Kim, M. Endo, D.S. Su, *Boron-doped onion-like carbon with enriched substitutional boron: The relationship between electronic properties and catalytic performance*, J. Mater. Chem. A. 3 (2015) 21805–21814.

[80] A. V. Okotrub, L.G. Bulusheva, V.L. Kuznetsov, Y. V. Butenko, A.L. Chuvilin, M.I. Heggie, *X-ray Emission Studies of the Valence Band of Nanodiamonds Annealed at Different Temperatures*, J. Phys. Chem. A. 105 (2001) 9781–9787.

[81] Y. V. Butenko, S. Krishnamurthy, A.K. Chakraborty, V.L. Kuznetsov, V.R. Dhanak, M.R.C. Hunt, L. Šiller, *Photoemission study of onionlike carbons produced by annealing nanodiamonds*, Phys. Rev. B. 71 (2005) 075420.

[82] D. Weingarth, M. Zeiger, N. Jäckel, M. Aslan, G. Feng, V. Presser, *Graphitization as a universal tool to tailor the potential-dependent capacitance of carbon supercapacitors*, Adv. Energy Mater. 4 (2014) 1400316.

[83] G.S. Szymański, M. Wiśniewski, P. Olejnik, S. Koter, E. Castro, L. Echegoyen, A.P. Terzyk, M.E. Plonska-Brzezinska, *Correlation between the catalytic and electrocatalytic properties of nitrogen-doped carbon nanoonions and the polarity of the carbon surface: Experimental and theoretical investigations*, Carbon. 151 (2019) 120–129.

[84] A. V. Okotrub, L.G. Bulusheva, V.L. Kuznetsov, A. V. Gusel'Nikov, A.L. Chuvilin, *Electronic state of nanodiamond/graphite interfaces*, Appl. Phys. A Mater. Sci. Process. 81 (2005) 393–398.

[85] L.G. Bulusheva, A. V. Okotrub, V.L. Kuznetsov, D. V. Vyalikh, *Soft X-ray spectroscopy and quantum chemistry characterization of defects in onion-like carbon produced by nanodiamond annealing*, Diam. Relat. Mater. 16 (2007) 1222–

1226.

[86] A. Bianconi, S.B.M. Hagström, R.Z. Bachrach, *Photoemission studies of graphite high-energy conduction-band and valence-band states using soft-x-ray synchrotron radiation excitation*, Phys. Rev. B. 16 (1977) 5543–5548.

[87] H. Ago, T. Kugler, F. Cacialli, K. Petritsch, R.H. Friend, W.R. Salaneck, Y. Ono, T. Yamabe, K. Tanaka, *Workfunction of purified and oxidised carbon nanotubes*, Synth. Met. 103 (1999) 2494–2495.

[88] D. Tasis, N. Tagmatarchis, A. Bianco, M. Prato, *Chemistry of carbon nanotubes*, Chem. Rev. 106 (2006) 1105–1136.

[89] M. Bartkowski, S. Giordani, *Supramolecular chemistry of carbon nano-onions*, Nanoscale. 12 (2020) 9352–9358.

[90] O. Mykhailiv, H. Zubyk, M.E. Plonska-Brzezinska, *Carbon nano-onions: unique carbon nanostructures with fascinating properties and their potential applications*, Inorganica Chim. Acta. 468 (2017) 49–66.

[91] M.E. Plonska-Brzezinska, A. Palkar, K. Winkler, L. Echegoyen, *Electrochemical properties of small carbon nano-onion films*, Electrochem. Solid-State Lett. 13 (2010) K35.

[92] M.E. Plonska-Brzezinska, A.T. Dubis, A. Lapinski, A. Villalta-Cerdas, L. Echegoyen, *Electrochemical properties of oxidized carbon nano-onions: DRIFTS-FTIR and Raman spectroscopic analyses*, ChemPhysChem. 12 (2011) 2659–2668.

[93] A. Palkar, A. Kumbhar, A.J. Athans, L. Echegoyen, *Pyridyl-functionalized and water-soluble carbon nano onions: first supramolecular complexes of carbon nano onions*, Chem. Mater. 20 (2008) 1685–1687.

[94] Y. Gao, Y.S. Zhou, M. Qian, X.N. He, J. Redepenning, P. Goodman, H.M. Li, L. Jiang, Y.F. Lu, *Chemical activation of carbon nano-onions for high-rate supercapacitor electrodes*, Carbon. 51 (2013) 52–58.

[95] Y. Liu, D.Y. Kim, *Enhancement of capacitance by electrochemical oxidation of nanodiamond derived carbon nano-onions*, Electrochim. Acta. 139 (2014) 82–87.

[96] J. Zhang, H. Zou, Q. Qing, Y. Yang, Q. Li, Z. Liu, X. Guo, Z. Du, *Effect of chemical oxidation on the structure of single-walled carbon nanotubes*, J. Phys. Chem. B. 107 (2003) 3712–3718.

[97] H. Hu, B. Zhao, M.E. Itkis, R.C. Haddon, *Nitric acid*

purification of single-walled carbon nanotubes, J. Phys. Chem. B. 107 (2003) 13838–13842.

[98] M.E. Plonska-Brzezinska, A. Lapinski, A.Z. Wilczewska, A.T. Dubis, A. Villalta-Cerdas, K. Winkler, L. Echegoyen, *The synthesis and characterization of carbon nano-onions produced by solution ozonolysis*, Carbon. 49 (2011) 5079–5089.

[99] V. Georgakilas, D.M. Guldi, R. Signorini, R. Bozio, M. Prato, *Organic functionalization and optical properties of carbon onions*, J. Am. Chem. Soc. 125 (2003) 14268–14269.

[100] A.S. Rettenbacher, B. Elliott, J.S. Hudson, A. Amirkhanian, L. Echegoyen, *Preparation and functionalization of multilayer fullerenes (carbon nano-onions)*, Chem. - A Eur. J. 12 (2006) 376–387.

[101] K. Flavin, M.N. Chaur, L. Echegoyen, S. Giordani, *Functionalization of multilayer fullerenes (carbon nano-onions) using diazonium compounds and "click" chemistry*, Org. Lett. 12 (2010) 840–843.

[102] M.E. Plonska-Brzezinska, D.M. Brus, J. Breczko, L. Echegoyen, *Carbon nano-onions and biocompatible polymers for flavonoid incorporation*, Chem. - A Eur. J. 19 (2013) 5019–5024.

[103] J. Breczko, M.E. Plonska-Brzezinska, L. Echegoyen, *Electrochemical oxidation and determination of dopamine in the presence of uric and ascorbic acids using a carbon nano-onion and poly(diallyldimethylammonium chloride) composite*, Electrochim. Acta. 72 (2012) 61–67.

[104] J. Breczko, K. Winkler, M.E. Plonska-Brzezinska, A. Villalta-Cerdas, L. Echegoyen, *Electrochemical properties of composites containing small carbon nano-onions and solid polyelectrolytes*, J. Mater. Chem. 20 (2010) 7761.

[105] C.D.G. Tovar, J.I. Castro, C.H. Valencia, D.P.N. Porras, J.H.M. Hernandez, M.E. Valencia, J.D. Velásquez, M.N. Chaur, *Preparation of chitosan/poly(vinyl alcohol) nanocomposite films incorporated with oxidized carbon nano-onions (multi-layer fullerenes) for tissue-engineering applications*, Biomolecules. 9 (2019) 684.

[106] J. Bartelmess, M. Frasconi, P.B. Balakrishnan, A. Signorelli, L. Echegoyen, T. Pellegrino, S. Giordani, *Non-covalent functionalization of carbon nano-onions with pyrene-BODIPY dyads for biological imaging*, RSC Adv. 5 (2015) 50253–

50258.

[107] D.M. Bobrowska, J. Czyrko, K. Brzezinski, L. Echegoyen, M.E. Plonska-Brzezinska, *Carbon nano-onion composites: Physicochemical characteristics and biological activity*, Fullerenes, Nanotub. Carbon Nanostructures. 25 (2017) 185–192.

[108] A. Camisasca, S. Giordani, *Surfactant-mediated dispersions of carbon nano-onions in aqueous solution*, Nano Express. 1 (2020) 010018.

[109] L. Zhou, C. Gao, D. Zhu, W. Xu, F.F. Chen, A. Palkar, L. Echegoyen, E.S.-W. Kong, *Facile functionalization of multilayer fullerenes (carbon nano-onions) by nitrene chemistry and "grafting from" strategy*, Chem. - A Eur. J. 15 (2009) 1389–1396.

[110] J.P. Bartolome, A. Fragoso, *Preparation of stable aqueous dispersions of carbon nano-onions via supramolecular crown ether-ammonium interactions with aminated biocompatible polymers*, J. Mol. Liq. 269 (2018) 905–911.

[111] E. Wajs, A. Molina-Ontoria, T.T. Nielsen, L. Echegoyen, A. Fragoso, *Supramolecular solubilization of cyclodextrin-modified carbon nano-onions by host–guest interactions*, Langmuir. 31 (2015) 535–541.

[112] D. Zheng, G. Yang, Y. Zheng, P. Fan, R. Ji, J. Huang, W. Zhang, J. Yu, *Carbon nano-onions as a functional dopant to modify hole transporting layers for improving stability and performance of planar perovskite solar cells*, Electrochim. Acta. 247 (2017) 548–557.

[113] A. Hirata, M. Igarashi, T. Kaito, *Study on solid lubricant properties of carbon onions produced by heat treatment of diamond clusters or particles*, Tribol. Int. 37 (2004) 899–905.

[114] N. Keller, N.I. Maksimova, V. V. Roddatis, M. Schur, G. Mestl, Y. V. Butenko, V.L. Kuznetsov, R. Schlögl, *The catalytic use of onion-like carbon materials for styrene synthesis by oxidative dehydrogenation of ethylbenzene*, Angew. Chemie Int. Ed. 41 (2002) 1885.

[115] J. Yang, Y. Zhang, D.Y. Kim, *Electrochemical sensing performance of nanodiamond-derived carbon nano-onions: comparison with multiwalled carbon nanotubes, graphite nanoflakes, and glassy carbon*, Carbon. 98 (2016) 74–82.

[116] O.C. Ozoemena, L.J. Shai, T. Maphumulo, K.I. Ozoemena, *Electrochemical sensing of dopamine using onion-like*

carbons and their carbon nanofiber composites, Electrocatalysis. (2019) 1–11.

[117] J.P. Bartolome, A. Fragoso, *Electrochemical detection of nitrite and ascorbic acid at glassy carbon electrodes modified with carbon nano-onions bearing electroactive moieties*, Inorganica Chim. Acta. 468 (2017) 223–231.

[118] E. Sohouli, A.H. Keihan, F. Shahdost-fard, E. Naghian, M.E. Plonska-Brzezinska, M. Rahimi-Nasrabadi, F. Ahmadi, *A glassy carbon electrode modified with carbon nanoonions for electrochemical determination of fentanyl*, Mater. Sci. Eng. C. 110 (2020) 110684.

[119] D. Mohapatra, N.S.K. Gowthaman, M.S. Sayed, J.-J. Shim, *Simultaneous ultrasensitive determination of dihydroxybenzene isomers using GC electrodes modified with nitrogen-doped carbon nano-onions*, Sensors Actuators B Chem. 304 (2020) 127325.

[120] V. Sok, A. Fragoso, *Amperometric biosensor for glyphosate based on the inhibition of tyrosinase conjugated to carbon nano-onions in a chitosan matrix on a screen-printed electrode*, Microchim. Acta. 186 (2019) 569.

[121] J.P. Bartolome, L. Echegoyen, A. Fragoso, *Reactive carbon nano-onion modified glassy carbon surfaces as DNA sensors for human papillomavirus oncogene detection with enhanced sensitivity*, Anal. Chem. 87 (2015) 6744–6751.

[122] M. Rizwan, S. Elma, S.A. Lim, M.U. Ahmed, *AuNPs/CNOs/SWCNTs/chitosan-nanocomposite modified electrochemical sensor for the label-free detection of carcinoembryonic antigen*, Biosens. Bioelectron. 107 (2018) 211–217.

[123] J. Mohapatra, B. Ananthoju, V. Nair, A. Mitra, D. Bahadur, N.V. Medhekar, M. Aslam, *Enzymatic and non-enzymatic electrochemical glucose sensor based on carbon nano-onions*, Appl. Surf. Sci. 442 (2018) 332–341.

[124] M. Rizwan, M. Hazmi, S.A. Lim, M.U. Ahmed, *A highly sensitive electrochemical detection of human chorionic gonadotropin on a carbon nano-onions/gold nanoparticles/polyethylene glycol nanocomposite modified glassy carbon electrode*, J. Electroanal. Chem. 833 (2019) 462–470.

Chapter 2

Determination of the Hansen solubility parameters for carbon nano-onions and prediction of their dispersibility in organic solvents[1]

2.1. Introduction

CNOs are probably the least studied allotropes of carbon despite their discovery before nanotubes and fullerenes. In the recent years, many potential applications of CNOs have been proposed including energy storage [1], photovoltaic cells [2], lubricants [3], catalysis [4], and biomedical applications [5]. Our group has recently demonstrated that incorporating CNOs in the construction of electrochemical sensors leads to a marked improvement of the analytical performance of such devices [6,7]. These applications are the result of a combination of electronic (high conductivity) and interfacial (high area-to-volume ratio) properties and illustrate that CNOs are very attractive nanomaterials with a wide range of potential applications still to be explored.

Like other carbon nanomaterials, CNOs are poorly dispersible in polar and nonpolar solvents. The strong intermolecular interactions such as van der Waals and π-stacking forces between the CNOs lead to the formation of non-dispersible aggregates. To overcome this problem, chemical or supramolecular modifications of the outer layer

---

[1] *This Chapter was published in J.C. Zuaznabar-Gardona, A. Fragoso, Journal of Molecular Liquids, 294 (2019) 111646.*

of CNOs are the most extended choices [8]. The introduction of functional groups on the surface of CNOs hinders the formation of the aggregates and favors the interaction with the solvents. As a result, CNOs dispersible in polar and nonpolar solvents can be obtained [9–11]. Recently, the dispersion of carbon-based nanomaterials including functionalized CNOs have been reviewed [12]. However, studies on the dispersion behavior of pristine CNOs in different solvents have not been reported. This is very important, considering that covalent modifications may alter the electronic properties of the CNOs.

The determination of the solubility parameter (δ) is an effective way to evaluate the solubility or the dispersibility of a material in different solvents or the interaction between two materials [13]. The concept of the solubility parameter was first used by Hildebrand and Scott [14] and further extended by Hansen [15]. In Hansen's theory, the solubility parameter is split into three components called the Hansen solubility parameters (HSPs). These parameters represent the contributions from dispersive (δ_D), dipolar (δ_P), and hydrogen bond (δ_H) interactions between a solute and a solvent. The HSPs of a substance define the center of a sphere of radius R_0 in a three-dimensional space with axes δ_D, δ_P and δ_H (Figure 2.1a). R_0 is called the interaction radius and defines the maximum difference in interaction between solute and solvent or, in general, between the studied material and any other substance. This interaction is described by the solubility parameter distance (R_a) and the Relative Energy Difference (RED). R_a and RED are calculated according to equations 1 and 2, respectively:

$$R_a = \sqrt{4(\delta_{D_1} - \delta_{D_2})^2 + (\delta_{P_1} - \delta_{P_2})^2 + (\delta_{H_1} - \delta_{H_2})^2} \qquad (1)$$

$$RED = \frac{R_a}{R_0} \qquad (2)$$

where subscript 1 refers to the studied material and, 2 to the solvent. A RED lower than 1 (for $R_a < R_0$) suggest a relatively strong interaction between the studied material and the solvent while RED > 1 means that there is a weak interaction between the two substances.

The HSPs could be calculated by group contributions or classical methods. The group contributions method uses the contributions of dispersive forces, dipolar and hydrogen bond interactions from each functional group present on the structure of the studied material to the respective solubility parameters [16–18]. In the other hand, the classical approach consists in testing the studied material in a series of solvents with known HSPs. The solvents are arbitrarily classified in good or bad depending on whether there is or not interaction with the material, respectively. Finally, the values of δ_D, δ_P, δ_H and R_0 are determined by finding a sphere in the δ_D, δ_P, δ_H space with the minimum radio such that only the good solvents could lie inside, and all bad solvents are outside the sphere. This step involves an optimization problem and has been solved with the aid of different mathematical algorithms [19].

HSPs have been used to assess the solubility or the dispersion behavior of various materials including polymers, biomolecules and nanomaterials. For instance, the solubility of C_{60} has been correlated with the HSPs of various solvents and polymers being its δ_D, δ_P and

δ_H values equal to 19.7, 2.9, and 2.7 MPa$^{0.5}$, respectively [20]. For carbon nanotubes, the HSPs vary depending on the nature of the nanotubes and the functional groups present on the surface. The reported HSPs values for pristine single-walled carbon nanotubes (SWCNTs) and multi-walled carbon nanotubes (MWCNTs) are 17.8, 7.5, 7.6 MPa$^{0.5}$ and 16.0, 10.0, 8.5 MPa$^{0.5}$, respectively [21,22]. Finally, Hernández and co-workers estimated the Hansen solubility parameters for graphene to be $\delta_D \approx 18.0$, $\delta_P \approx 9.3$, and $\delta_H \approx 7.7$ MPa$^{0.5}$ [23]. In all cases, carbon nanomaterials show an important contribution of dispersive forces as a result of strong intermolecular hydrophobic forces.

To the best of our knowledge, the dispersion of CNOs in different solvents and the determination of their HSPs have not been addressed. Thus, in this Chapter, we study the dispersion behavior of CNOs in a series of 20 solvents with different polarities to estimate the HSPs for CNOs using different optimization algorithms. The reported HSPs for CNOs were then, used to predict their dispersion in other solvents.

2.2. Materials and methods

Hexane (HEX), heptane (HEP), dioxane (DIOX), cyclohexane (cHEX), toluene (TOL), diethyl ether (Et_2O), tert-butyl alcohol (TBA), 1-butanol (BuOH), ethanol (EtOH), methanol (MeOH), dimethyl sulfoxide (DMSO), chloroform ($CHCl_3$), tetrahydrofuran (THF), 1,1,2,2-tetrachloroethane (TCE), benzyl alcohol (BzOH), acetone (ACE), N-methyl-2-pyrrolidone (NMP), N,N-dimethylformamide (DMF), acetonitrile (ACN) and MiliQ® water were of high purity (<99.9%) and obtained from commercial suppliers. CNOs were prepared by annealing of nanodiamonds (NDs) at 1200ºC under inert atmosphere as previously reported [24].

The synthesized CNOs samples were characterized using high resolution transmission electron microscopy (HRTEM) on a Jeol 2011 instrument operated at 200 kV. Samples were prepared in copper grids with a carbon layer and the CNOs were dispersed in ethanol. Raman spectra were acquired with a Renishaw 2003 spectrometer operating at a wavelength of 244 and 514 nm and 10 s of exposition time for NDs and CNOs samples, respectively. The spectra were analyzed using Wire v 3.2 software (Renishaw plc, United Kingdom). A glass slide was used to hold the samples.

The dispersion of CNOs was tested in 20 solvents. In all cases, appropriate amounts of CNOs powder were placed in a 3 mL glass vial before adding a volume of solvent to obtain a 1 mg mL^{-1} dispersion. Then, the mixture was sonicated in an ultrasonic bath (40 kHz, 110 W) for 1 hour. If the CNOs powder remained as sediment after ultrasonic treatment, the solvent was considered as incompatible or a bad solvent. Solvents in which the CNOs remained clearly dispersed one hour after sonication were classified as compatible or good solvents.

The size distribution of the CNOs in the dispersion of good solvents was measured by Dynamic Light Scattering (DLS) with a 3000HSa ZetaSizer from Malvern Instruments at 25ºC. A 0.05 mg mL^{-1} dispersion was used directly without filtration. The scattered intensity fell within the range between 100 and 350 kcps, as suggested by the equipment vendor. The size distribution was reported in terms of the particle volume density (% volume). The stability of the dispersions was investigated by ζ-potential measurements using the same instrument. Ammonium acetate (1 mmol L^{-1}) was added to increase the conductivity of the dispersions in the good solvents [25].

The Hansen solubility parameters for CNOs were estimated by fitting the dispersion data to a sphere with the center defined by the δ_D, δ_P, δ_H values for the CNOs and a radius R_0 where only the good solvents could lie inside and all the bad solvents outside the sphere. The procedure for data fitting was based on the algorithm described by Gharagheizi [26], which seeks to minimize the objective function given by equation 3:

$$f\left(\delta_{D_{CNOs}}, \delta_{P_{CNOs}}, \delta_{H_{CNOs}}, R_0\right) = 1 - data\_fit \qquad (3)$$

where *data_fit* is a quality-of-fit function called the Desirability Function that is the most appropriate statistical treatment for this type of problem [27]. The *data_fit* function has the following form:

$$data\_fit = (A_1 \cdot A_2 \ldots A_n)^{\frac{1}{n}} \qquad (4)$$

where *n* is the total number of solvents tested and A_i is the data fit for the *i^th^* solvent given in equations 5, 6 and 7:

$$A_i = e^{-(error\_distance)} \qquad (5)$$

-For good solvents, (dispersibility (i) = 1):

$$error\_distance = \begin{cases} R_{a_i} - R_0 \; if \; R_{a_i} > R_0 \\ 0 \qquad if \; R_{a_i} \leq R_0 \end{cases} \qquad (6)$$

-For bad solvents, (dispersibility (i) = 0):

$$error\_distance = \begin{cases} 0 & if\ R_{a_i} > R_0 \\ R_0 - R_{a_i} & if\ R_{a_i} \leq R_0 \end{cases} \tag{7}$$

The minimization of equation 3 resulted in the determination of δ_D, $\delta_{P,}$ δ_H and R_0 for CNOs. Equation 3 was minimized by using different global and local solvers implemented in the Optimization Toolbox of MATLAB® version R2018b.

Once the Hansen sphere for CNOs was constructed, the δ_D, $\delta_{P,}$ δ_H and RED values of a group of 8 solvents not tested before were determined and compared with the experimental dispersibility of the CNOs in these solvents determined as described before.

2.3. Results and discussion

2.3.1. Preparation and characterization of CNOs

CNOs were prepared by annealing of nanodiamonds at 1200ºC under inert atmosphere. The structural transformation of NDs to CNOs results in a color change from grey to black (Figure 2.1b). The transformation is also reflected in the Raman active vibration modes of C-C bonds which are used systematically to characterize carbon nanostructures [28]. Raman spectra of NDs and the as-prepared CNOs are presented in Figure 2.1c. The Raman spectrum of NDs showed a sharp band at 1335 cm^{-1} due to the C-C sp^3 vibrations and a broad band around 1570 cm^{-1} which originates from surface functional groups and adsorbed molecules in nanodiamonds [29,30]. In contrast, the Raman spectrum of synthesized CNOs showed the so-called G and D bands [31]. The G band of CNOs is found at 1581 cm^{-1} and it is due to a Raman-active optic in-plane stretching mode of sp^2 bonded carbons. The D band at 1345 cm^{-1}, is related with defects in the crystalline lattice of the carbon material. Furthermore, the deconvolution of the G band in only one Lorentzian peak suggests the lack of edges observed in polyhedral carbon nano-onions (Figure 2.1c, inset) [31]. The D/G ratio was 1.03 and remained essentially unchanged after ultrasonication in acetone and TCE, similar to what has been observed for CNOs and CNTs [25].

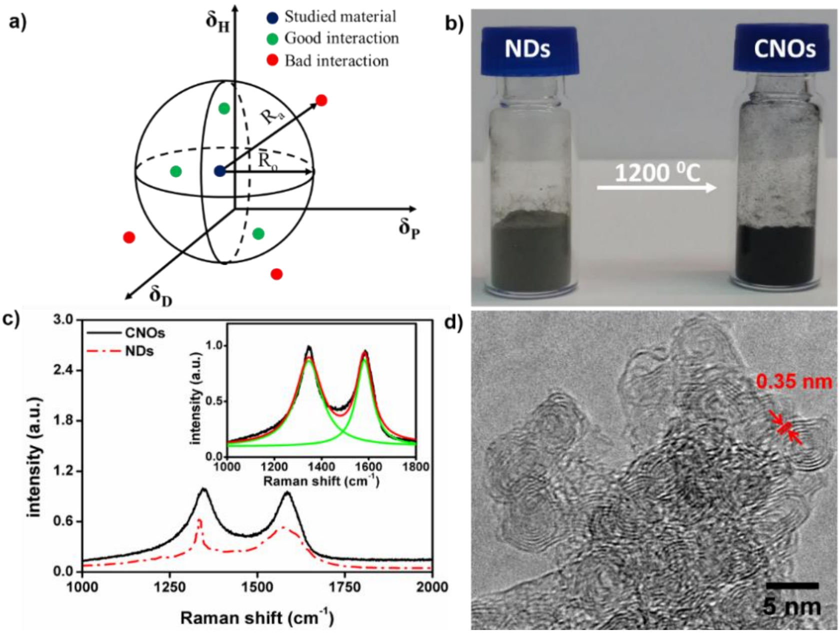

Figure 2.1. a) Schematic representation of the Hansen sphere. b) Transformation of NDs to CNOs after thermal annealing. c) Raman spectra of NDs and synthesized CNOs. Inset: Deconvolution of G and D bands of CNOs. d) HRTEM image of as-prepared CNOs.

High resolution transmission electron microscopy (HRTEM) was used to confirm the synthesis of CNOs from the annealing of NDs. A representative HRTEM image of synthesized CNOs is presented in Figure 2.1d. Inspection of HRTEM image showed quasi-spherical multilayered particles of around 5 nm. The particles have an average of 5-6 graphitic shells separated by around of 0.35 nm. These results agree with the Raman analysis and indicate that the synthetic conditions were adequate to form small diameter CNOs from NDs.

2.3.2. Dispersion of CNOs in different solvents

The dispersion of CNOs was addressed in 20 solvents with a wide range of characteristics including protic, polar aprotic and nonpolar solvents (Table 2.1). After ultrasonic treatment, stable dispersions were obtained in chloroform ($CHCl_3$), tetrahydrofuran (THF), 1,1,2,2-tetrachloroethane (TCE), benzyl alcohol (BzOH), acetone (ACE), N-methyl-2-pyrrolidone (NMP), *N*,*N*-dimethylformamide (DMF) and acetonitrile (ACN) (Figure 2.2a).

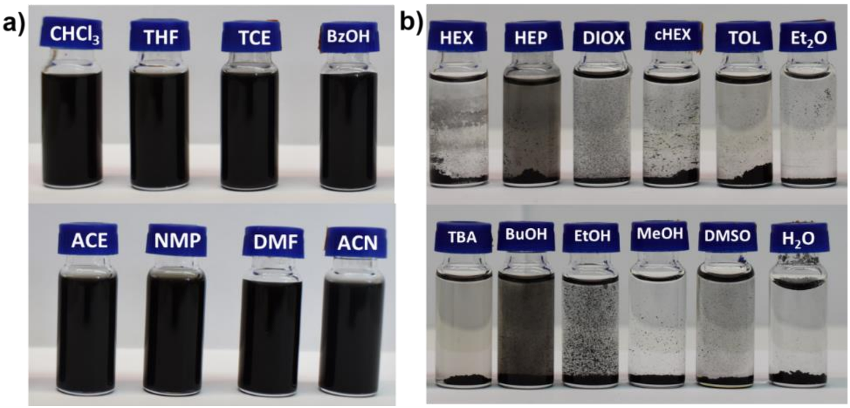

Figure 2.2. Photographs of CNOs dispersed in a) good and, b) bad solvents after ultrasonication for 1 hour.

In these solvents, no sedimentation was observed with time, even after five months in the case of NMP and DMF. Thus, these eight solvents were considered as good solvents. In contrast, most of the nonpolar solvents and some polar solvents like methanol (MeOH), 1-butanol (BuOH) and ethanol (EtOH) resulted in poor dispersion of CNOs (Figure 2.2b) and were classified as bad solvents for determination of the HSPs.

DLS analysis was performed to CNOs dispersions (0.05 mg/mL) in all of the good solvents. A monomodal particle size distribution was observed in all the cases. As an example, the particle size distribution of CNOs dispersed in DMF is illustrated in Figure 2.3a.

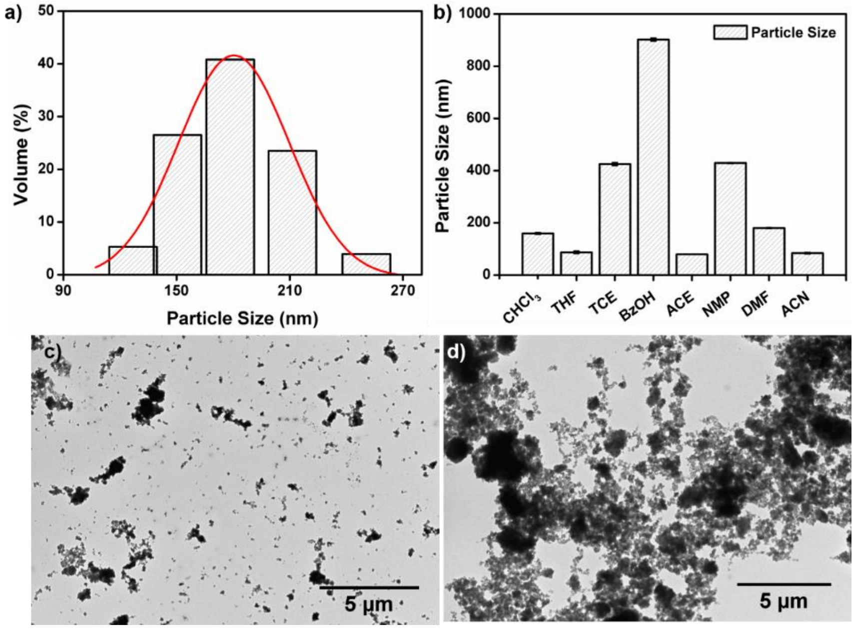

Figure 2.3. a) DLS particle size distribution of CNOs dispersed in DMF (0.5 mg mL^{-1}). b) Hydrodynamic particle sizes obtained by DLS analysis of CNOs dispersed in all good solvents. TEM images of CNOs dispersed in c) DMF and d) toluene.

The particle size of CNOs dispersed in these solvents are summarized in Figure 2.3b. In general, CNO dispersions contained particles ranging from 70 to 900 nm in size. Such sizes are greater than the size of a single CNO (~5 nm) and indicates that even in good solvents, CNOs form aggregates of different sizes. The presence of CNO aggregates was confirmed by TEM analysis. Representative TEM images of CNO dispersions in DMF (a good solvent) and toluene (a bad solvent) are shown in Figures 2.3c and 2.3d, respectively. CNO aggregates of around 180 nm are observed in the case of CNOs dispersed in DMF while highly aggregated micrometer sized particles were observed in toluene.

The CNO dispersions in the good solvents showed ζ-potential values higher than ±15 mV indicating they form stable dispersions (Figure 2.4). The differences in the sign of the values can be explained in terms of proton exchange between the solvents and the polar groups present on the surface of CNOs. When CNOs are placed in a solvent that is not a good proton acceptor like $CHCl_3$ or TCE, CNO groups are unable to donate protons to the medium, resulting in a positive value of the ζ-potential. On the other hand, solvents like DMF, or acetone enable CNOs to donate protons, switching the ζ-potential to negative values [32].

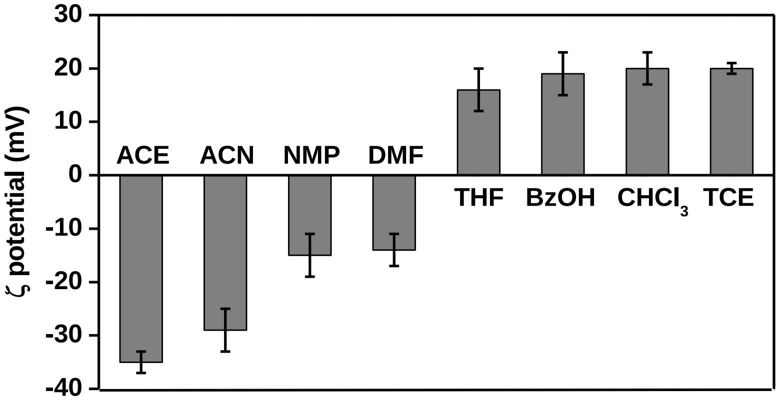

Figure 2.4. ζ potential values of CNO dispersions in the good solvents.

2.3.3. Determination of Hansen solubility parameters for CNOs

The results of the dispersion test of CNOs in the 20 solvents are tabulated in Table 2.1 and were used to determine the HSPs values for CNOs.

Table 2.1. List of solvents tested to determine the HSPs values for CNOs.

	Calculated parameters				**Experimental**
Solvent	**δ_D**	**δ_P**	**δ_H**	**RED***	**dispersibility**
acetone	15.5	10.4	7.0	0.171	1
tetrahydrofuran	16.8	5.7	8.0	0.553	1
N-methyl-2-pyrrolidone	18.0	12.3	7.2	0.574	1
N,*N*-dimethylformamide	17.4	13.7	11.3	0.686	1
1,1,2,2-tetrachloroethane	18.8	5.1	5.3	0.958	1
chloroform	17.8	3.1	5.7	0.978	1
benzyl alcohol	18.4	6.3	13.7	0.999	1
acetonitrile	15.3	18	6.1	0.999	1
dimethyl sulfoxide	18.4	16.4	10.2	1.001	0
tert-butyl alcohol	15.2	5.1	14.7	1.003	0
diethyl ether	14.5	2.9	4.6	1.004	0
dioxane	17.5	1.8	9.0	1.055	0
1-butanol	16.0	5.7	15.8	1.060	0
water	18.1	12.9	15.5	1.088	0
toluene	18.0	1.4	2.0	1.350	0
ethanol	15.8	8.8	19.4	1.366	0
cyclohexane	16.8	0.0	0.2	1.534	0
heptane	15.3	0.0	0.0	1.543	0
hexane	14.9	0.0	0.0	1.555	0
methanol	15.1	12.3	22.3	1.739	0

*RED was calculated using the HSPs average values listed in Table 2.2, see below.

The HSPs of each tested solvent were obtained from literature [15]. In all cases, δ_D, δ_P, δ_H and R_0 values are expressed in $MPa^{0.5}$ units. The dispersibility behavior of the test solvent was arbitrary judged as 1 if good dispersions of CNOs were obtained or 0 in the contrary (Figure 2.2).

This experimental data was fitted further to a sphere following the procedure described in the Experimental section. The δ_D, δ_P, δ_H and

R_0 values for CNOs were estimated by using different local and global solvers implemented in MATLAB® version R2018b. The global solvers used here were surrogate, pattern search, genetic algorithm, particle swarm and global search. Additionally, three local solvers were also tested for comparison: *fminsearch*, *fmincon* and *fminunc*. Genetic algorithm [33], particle swarm [19], and *fminsearch* solvers [26] have been used previously to estimate the HSPs for polymeric materials. All these solvers are able to find global or local solutions to optimization problems that contain multiple maxima or minima. They employ different algorithms to find the best solutions and their description are out of the scope of the present work. The values of δ_D, $\delta_{P,}$ δ_H and R_0 obtained with the different solvers are summarized in Table 2.2.

The HSPs and R_0 values calculated using the global solvers were quite similar among them. Additionally, these algorithms were able to find the best solutions since the values of *1–data_fit* function was 0. This means that all good solvents are located inside the solubility sphere while the bad solvents lied outside. On the contrary, the solutions found by two of the local solvers, *fminsearch* and *fminunc*, resulted in a local minimum since *1–data_fit* was greater than 0. That means that the HSPs and R_0 values obtained with these local solvers are local solutions and not a global solution of equation 3. This is one of the drawbacks of using local solvers algorithms to find global solutions for an optimization problem.

Table 2.2. HSPs for CNOs calculated using different local and global solver algorithms implemented in MATLAB®.

	Solver	$1 - data\_fit$	δ_D	δ_P	δ_H	R_0
local	*fmincon*	0	16.0	10.0	8.0	8.4
	fminsearch	0.0004	15.9	10.0	8.1	8.4
	fminunc	0.1594	15.9	10.0	8.1	8.4
global	pattern search	0	15.9	10.0	8.0	8.4
	genetic algorithm	0	15.9	10.0	8.1	8.3
	particle swarm	0	16.0	10.0	8.0	8.4
	global search	0	15.9	10.0	8.0	8.4
	surrogate	0	16.0	10.0	8.0	8.3
		Average	**15.9**	**10.0**	**8.0**	**8.4**

The HSPs and R_0 values for other carbon-based materials reported in previous studies are listed in Table 2.3 together with the solubility parameters for CNOs calculated in this work. The inspection of the tabulated values reflects the structural features of as-prepared CNOs and the similarities with other carbon-based materials. The small diameter (c.a. 5 nm) of studied CNOs increases the number of possible π-π interactions between the CNOs, which results in the relatively high value of the δ_D term [34].These multiple interactions difficult CNOs to be dispersed in common solvents. The δ_P term for CNOs is three times higher than that for C_{60} but similar to the values for MWCNTs and oxidized SWCNTs (SWCNTs-OXI). In these structures, the dipole moment depends mainly on the number of π electrons [22]. The presence of defects or carbon atoms with sp^3 hybrid orbitals increases the dipole moment resulting in higher δ_P values for CNOs, MWCNTs and SWCNTs-OXI in comparison to fullerenes which have a "*purer*" sp^2 structure. As for δ_H, the greater the number of functional groups that form hydrogen-bonds, the greater the value of this parameter. Thus, the δ_H value for CNOs indicates the presence of hydrogen-bonding functional groups on the outer-shell of CNOs. The presence of oxygenated functional groups in the CNOs prepared by NDs annealing have been previously confirmed by X-ray photoelectron spectroscopy analysis [24]. According to the values of the HSPs for CNOs, the good solvents would be those with relatively high values of δ_D, δ_P, and δ_H like DMF, NMP, acetic anhydride, etc.

Table 2.3. Comparison of HSPs and R_o values for CNOs and other reported carbon-based materials.

Material	**δ_D**	**δ_P**	**δ_H**	**R_0**	**Ref.**
SWCNTs-OXI	18.9	10.7	11.4	9.2	[35]
SWCNTs	16.0	4.3	2.1	5.2	[35]
MWCNTs	16.0	9.9	8.7	-	[22]
Carbon fibers	21.3	8.7	11.5	9.3	[36]
C_{60}	19.7	2.9	2.7	3.9	[36]
Graphene	18.0	9.3	7.7	-	[23]
CNOs	**15.9**	**10.0**	**8.0**	**8.4**	**This work**

The average of HSPs and R_0 values obtained with the global solvers were used to construct the Hansen solubility sphere for CNOs in the δ_D,δ_P,δ_H space (Figure 2.5). As a result of the optimization process the eight good solvents are inside the sphere while the bad ones are outside. These results are a visual indication that the optimization algorithms used in the present work were valid to calculate the HSPs for CNOs

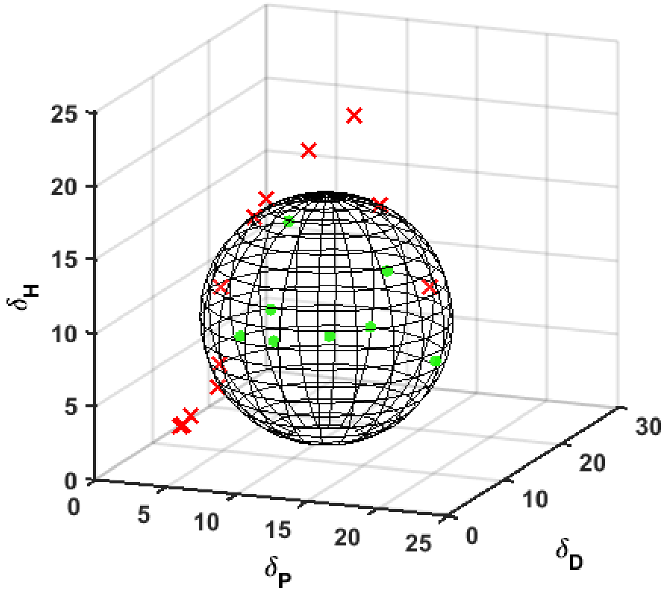

Figure 2.5. Hansen solubility sphere for CNOs calculated with the average values of HSPs and R_0 in Table 2.2. Green sphere points indicate good solvents and red crosses points bad solvents from Table 2.1.

2.3.4. Prediction of the dispersion of CNOs using their HSPs values

One practical application of the Hansen method is to estimate the solubility, the dispersibility or the interaction between two materials once their δ_D, δ_P, δ_H and R_0 values are known. To illustrate this, the prediction of the dispersion of CNOs in other solvents was attempted. The dispersion of CNOs was tested in four solvents with RED > 1 and other four with RED < 1. These solvents are listed in Table 2.4.

Table 2.4. HSPs values for the solvents used to predict the dispersion of CNOs.

Solvent	**Calculated parameters**				**Experimental**
	δ_D	**δ_P**	**δ_H**	**RED**	**dispersibility**
2,4-pentanedione	16.1	11.2	6.2	0.267	1
acetic anhydride	16	11.7	10.2	0.329	1
EGDA*	16.2	4.7	9.8	0.669	1
DPME*	15.5	4	10.3	0.773	1
ethylbenzene	17.8	0.6	1.4	1.447	0
nitrobenzene	20	10.6	3.1	1.140	0
octane	15.5	0	0	1.539	0
formamide	17.2	26.2	19	2.361	0

*EGDA: ethylene glycol diacetate, DPME: dipropylene glycol methyl ether

According to the RED definition (Equation 2), it would be expected that CNOs were dispersed only in those solvents where RED values were lower than 1. The results are presented in Figure 2.6. Cleary, only the solvents with RED < 1 were able to disperse the CNOs (Figure 2.6a). In the contrary, solvents with RED > 1 resulted in the precipitation of CNOs (Figure 2.6b). For solvents with RED close to 1 such as nitrobenzene, the dispersion sedimented slower than for the other three solvents. Among these four bad solvents, the solubility parameter ($\delta = \sqrt{\delta_D^2 + \delta_P^2 + \delta_H^2}$) for $PhNO_2$ is the closest to the δ for CNOs (22.8 and 20.5 $MPa^{0.5}$, respectively). This means that the energy to separate the $PhNO_2$ molecules in the liquid phase is similar to the energy required to disaggregate the CNOs. Thus, the interaction between the CNOs and $PhNO_2$ molecules are the most favorable energetically. As a result, a slower precipitation of CNOs in nitrobenzene is observed respect to the other three bad solvents.

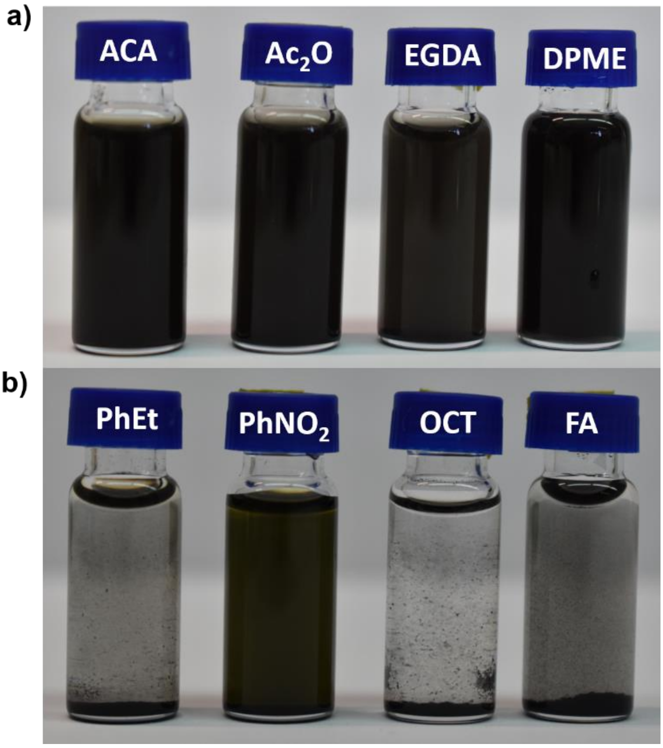

Figure 2.6. Digital pictures showing CNOs dispersed in solvents with a) RED < 1 and b) RED > 1. The solvents were 2,4-pentanedione (ACA), acetic anhydride (Ac_2O), ethylene glycol diacetate (EGDA), dipropylene glycol methyl ether (DPME), ethylbenzene (PhEt), nitrobenzene ($PhNO_2$), octane (OCT) and formamide (FA).

2.4. Conclusions

Carbon nano-onions (CNOs) were prepared by thermal annealing of nanodiamonds (NDs). Raman analysis and HRTEM images confirmed the transformation of NDs to quasi-spherical CNOs. The dispersion behavior of as-prepared CNOs was tested in 20 solvents with different polarities. Dynamical Light Scattering analysis revealed the presence of CNO aggregates even in those solvents where stable dispersions were obtained. This data was further used to calculate the Hansen solubility parameters (δ_D, δ_P, δ_H) and the solubility sphere for CNOs. Different global and local optimization algorithms implemented in MATLAB® were used for this purpose. There were not significant differences between the solutions found by the different solvers. The calculated δ_D (15.9), δ_P (10.0), δ_H (8.0) and R_0 (8.4) values for CNOs were similar to other carbon nanostructures (SWNTs and MWNTs). The HSPs and R_0 values for CNOs reported here were used to successfully predict their dispersion in other solvents. These results will be helpful to predict the behavior of CNOs in other solvents or their interaction with other materials with known HSPs.

References

[1] M. Zeiger, N. Jäckel, V.N. Mochalin, V. Presser, *Review: carbon onions for electrochemical energy storage*, J. Mater. Chem. A. 4 (2016) 3172–3196.

[2] D. Zheng, G. Yang, Y. Zheng, P. Fan, R. Ji, J. Huang, W. Zhang, J. Yu, *Carbon nano-onions as a functional dopant to modify hole transporting layers for improving stability and performance of planar perovskite solar cells*, Electrochim. Acta. 247 (2017) 548–557.

[3] A. Hirata, M. Igarashi, T. Kaito, *Study on solid lubricant properties of carbon onions produced by heat treatment of diamond clusters or particles*, Tribol. Int. 37 (2004) 899–905.

[4] N. Keller, N.I. Maksimova, V. V. Roddatis, M. Schur, G. Mestl, Y. V. Butenko, V.L. Kuznetsov, R. Schlögl, *The catalytic use of onion-like carbon materials for styrene synthesis by oxidative dehydrogenation of ethylbenzene*, Angew. Chemie Int. Ed. 41 (2002) 1885.

[5] A. Camisasca, S. Giordani, *Carbon nano-onions in biomedical applications: Promising theranostic agents*, Inorganica Chim. Acta. 468 (2017) 67–76.

[6] J.P. Bartolome, A. Fragoso, *Electrochemical detection of nitrite and ascorbic acid at glassy carbon electrodes modified*

with carbon nano-onions bearing electroactive moieties, Inorganica Chim. Acta. 468 (2017) 223–231.

[7] J.P. Bartolome, L. Echegoyen, A. Fragoso, *Reactive carbon nano-onion modified glassy carbon surfaces as DNA sensors for human papillomavirus oncogene detection with enhanced sensitivity*, Anal. Chem. 87 (2015) 6744–6751.

[8] J. Bartelmess, S. Giordani, *Carbon nano-onions (multi-layer fullerenes): chemistry and applications*, Beilstein J. Nanotechnol. 5 (2014) 1980–1998.

[9] E. Wajs, A. Molina-Ontoria, T.T. Nielsen, L. Echegoyen, A. Fragoso, *Supramolecular solubilization of cyclodextrin-modified carbon nano-onions by host–guest interactions*, Langmuir. 31 (2015) 535–541.

[10] J.P. Bartolome, A. Fragoso, *Preparation of stable aqueous dispersions of carbon nano-onions via supramolecular crown ether-ammonium interactions with aminated biocompatible polymers*, J. Mol. Liq. 269 (2018) 905–911.

[11] A.S. Rettenbacher, B. Elliott, J.S. Hudson, A. Amirkhanian, L. Echegoyen, *Preparation and functionalization of multilayer fullerenes (carbon nano-onions)*, Chem. - A Eur. J. 12 (2006) 376–387.

[12] O. V. Kharissova, C.M. Oliva González, B.I. Kharisov, *Solubilization and dispersion of carbon allotropes in water and non-aqueous solvents*, Ind. Eng. Chem. Res. 57 (2018) 12624–12645.

[13] X. Jiang, Y. Wang, M. Li, *Selecting water-alcohol mixed solvent for synthesis of polydopamine nano-spheres using solubility parameter*, Sci. Rep. 4 (2015) 6070.

[14] J.H. Hildebrand, R.L. Scott, The solubility of nonelectrolytes, 3rd ed., Reinhold, New York, 1950.

[15] C.M. Hansen, Hansen solubility parameters : a user's handbook, 2nd ed., CRC Press, Florida, 2007.

[16] E. Stefanis, C. Panayiotou, *A new expanded solubility parameter approach*, Int. J. Pharm. 426 (2012) 29–43.

[17] D.W. van. Krevelen, Properties of polymers, 3rd ed., Elsevier, Amsterdam, 1990.

[18] E. Stefanis, C. Panayiotou, *Prediction of Hansen solubility parameters with a new group-contribution method*, Int. J. Thermophys. 29 (2008) 568–585.

[19] M. Weng, *Determination of the Hansen solubility parameters with a novel optimization method*, J. Appl. Polym. Sci. 133

(2016) 43328.

[20] C.M. Hansen, A.L. Smith, *Using Hansen solubility parameters to correlate solubility of C_{60} fullerene in organic solvents and in polymers*, Carbon. 42 (2004) 1591–1597.

[21] S. Ata, T. Mizuno, A. Nishizawa, C. Subramaniam, D.N. Futaba, K. Hata, *Influence of matching solubility parameter of polymer matrix and CNT on electrical conductivity of CNT/rubber composite*, Sci. Rep. 4 (2015) 7232.

[22] S. Ata, T. Yamada, K. Hata, *Relationship between primary structure and Hansen solubility parameter of carbon nanotubes*, J. Nanosci. Nanotechnol. 17 (2017) 3310–3315.

[23] Y. Hernandez, M. Lotya, D. Rickard, S.D. Bergin, J.N. Coleman, *Measurement of multicomponent solubility parameters for graphene facilitates solvent discovery*, Langmuir. 26 (2010) 3208–3213.

[24] J.P. Bartolome, A. Fragoso, *Preparation and characterization of carbon nano-onions by nanodiamond annealing and functionalization by radio-frequency Ar/O_2 plasma*, Fullerenes, Nanotub. Carbon Nanostructures. 25 (2017) 327–334.

[25] L. Reinert, M. Zeiger, S. Suárez, V. Presser, F. Mücklich, *Dispersion analysis of carbon nanotubes, carbon onions, and nanodiamonds for their application as reinforcement phase in nickel metal matrix composites*, RSC Adv. 5 (2015) 95149–95159.

[26] F. Gharagheizi, *New procedure to calculate the Hansen solubility parameters of polymers*, J. Appl. Polym. Sci. 103 (2007) 31–36.

[27] E.C. Harrington, *The desirability function*, Ind. Qual. Control. 21 (1965) 494–498.

[28] P. Yan, B. Zhang, K.-H. Wu, D. Su, W. Qi, *Surface chemistry of nanocarbon: Characterization strategies from the viewpoint of catalysis and energy conversion*, Carbon. 143 (2019) 915–936.

[29] V.N. Mochalin, O. Shenderova, D. Ho, Y. Gogotsi, *The properties and applications of nanodiamonds*, Nat. Nanotechnol. 7 (2012) 11–23.

[30] A.C. Ferrari, J. Robertson, *Raman spectroscopy of amorphous, nanostructured, diamond–like carbon, and nanodiamond*, Philos. Trans. R. Soc. London. Ser. A Math. Phys. Eng. Sci. 362 (2004) 2477–2512.

[31] D. Codorniu Pujals, O. Arias de Fuentes, L.F. Desdín García, E. Cazzanelli, L.S. Caputi, *Raman spectroscopy of polyhedral carbon nano-onions*, Appl. Phys. A. 120 (2015) 1339–1345.

[32] M.. Chadwick, J.. Goodwin, E.. Lawson, P.D.. Mills, B. Vincent, *Surface charge properties of colloidal titanium dioxide in ethylene glycol and water*, Colloids Surfaces A Physicochem. Eng. Asp. 203 (2002) 229–236.

[33] G.C. Vebber, P. Pranke, C.N. Pereira, *Calculating Hansen solubility parameters of polymers with genetic algorithms*, J. Appl. Polym. Sci. 131 (2014) 39696–39708.

[34] J. Howell, M. Roesing, D. Boucher, *A functional approach to solubility parameter computations*, J. Phys. Chem. B. 121 (2017) 4191–4201.

[35] J. Ma, R.M. Larsen, *Effect of surface modification on the Hansen solubility parameters of single-walled carbon nanotubes*, Ind. Eng. Chem. Res. 52 (2013) 3514–3521.

[36] H. Launay, C.M. Hansen, K. Almdal, *Hansen solubility parameters for a carbon fiber/epoxy composite*, Carbon. 45 (2007) 2859–2865.

Chapter 3

Band structure, work function and interfacial diagrams of oxygen-functionalized carbon nano-onions[2]

3.1. Introduction

The interface between a CNOs layer and a metal or semiconductor becomes very important for most of their applications. This requires knowledge of the electronic structure of CNOs and the factors that can affect it. Ultraviolet photoelectron spectroscopy (UPS) is a useful tool to elucidate the electronic structure of a material and its corresponding work function, Fermi level and valence band position parameters [1]. UPS analysis of CNOs have mainly focused on studying how the annealing temperature used during their synthesis from nanodiamonds (NDs) affects their electronic structure [2–5]. These studies indicate the density of states (DOS) at the Fermi level increases with the annealing temperature. The increase in DOS was associated with the presence of unpaired electrons due to the accumulation of different types of defects in the curved graphite layers during graphitization of nanodiamonds [3,5]. Electron paramagnetic resonance (EPR) spectroscopy measurements confirmed the paramagnetism of CNOs prepared by the annealing of NDs [6].

---

[2] *This Chapter was published in J.C. Zuaznabar-Gardona, A. Fragoso, Synthetic Metals, 266 (2020) 116434.*

On the other hand, as it was discussed in Chapter 2, CNOs are poorly dispersible in polar and nonpolar solvents, similar to other carbon nanomaterials [7,8]. Chemical functionalization is a common strategy to overcome this problem. In particular, oxidative treatments have been frequently used for purification or as a first stage in further chemical modifications improving the dispersibility in a wide range of solvents [9]. However, few is known about the effect of the oxidation on the electronic structure of CNOs. Thus, in this Chapter, we study the effect of two oxidation treatments on the morphology and electronic structure of CNOs prepared by the annealing of NDs. CNOs were oxidized by using an Ar/O_2 radio frequency (RF) plasma or in the presence of a strong acid mixture (HNO_3/H_2SO_4) and the resulting products were analyzed by HRTEM, XPS and UPS. The interfacial energy diagrams were constructed from their respective UPS data with the aim to understand the electronic interactions at the interface between CNO particles and metal or semiconductor surfaces which could be exploited in the design of novel electrochemical or photovoltaic devices.

3.2. Materials and methods

CNOs were prepared by thermal annealing of detonation nanodiamonds (NDs) (from Tokyo Chemical Industry Co.) and further physically oxidized (CNO-RF) by using an Ar/O_2 radio frequency (RF) plasma [10] or chemically oxidized (CNO-OXI) in a HNO_3/H_2SO_4 mixture [11] as reported (Scheme 3.1).

High resolution transmission electron microscopy (HRTEM), X-Ray photoemission spectroscopy (XPS) and Ultraviolet photoelectron spectroscopy (UPS) were conducted at facilities of the Catalan Institute of Nanoscience and Nanotechnology (ICN2) in Barcelona, Spain. HRTEM images were recorded in a FEI TECNAI G^2 F20 microscope operated at 200 kV. Samples were dispersed in ethanol, cast on holey carbon grids and dried at room temperature before measurements.

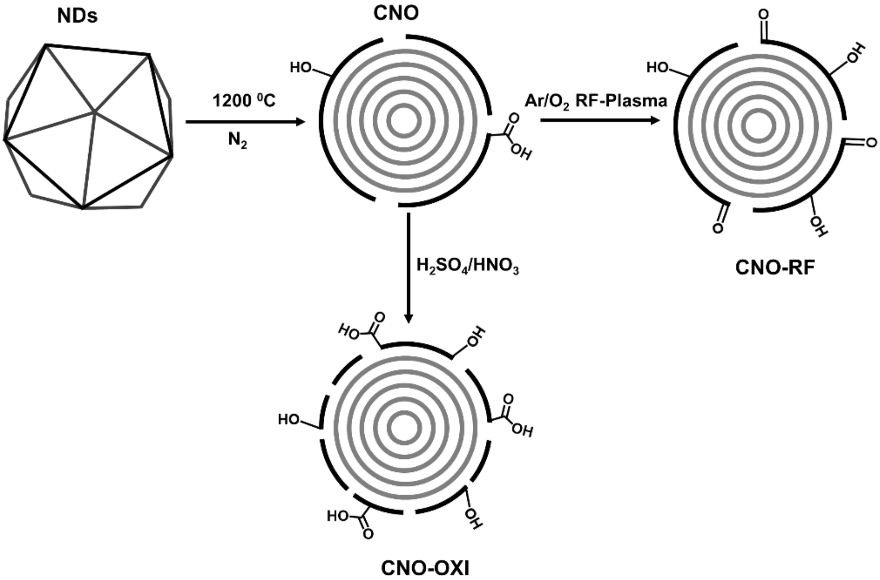

Scheme 3.1. Synthesis of CNO, CNO-RF and CNO-OXI.

XPS measurements were carried out using a Specs PHOIBOS 150 hemispherical energy analyzer using a monochromatic X-ray source (Al Kα line with an energy of 1486.6 eV and 400 W) with the energy referenced to the Fermi level. UPS spectra were obtained with incident irradiation from He I 21.2 eV ultraviolet light using the same hemispherical analyzer. Work functions were determined from the secondary electron cutoff of UPS He I spectra. The samples for XPS and UPS experiments were prepared by dropping a N,N-dimethylformamide suspension (4 mg mL^{-1}) of pristine CNO, CNO-RF or CNO-OXI onto a square piece cut from a glassy carbon wafer. The samples were then left to dry for several hours in vacuum prior to measurements. High-resolution XPS spectra were processed using the Casa XPS v 2.3.19 software.

Specific surface areas and pore size distribution of degassed samples of CNO, CNO-RF and CNO-OXI were calculated from the nitrogen adsorption isotherms at 77 K on a Quadrasorb SI (Quantachrome Instruments) surface area and pore size analyzer.

3.3. Results and discussion

3.3.1. Morphological and structural characterization of CNO, CNO-RF and CNO-OXI particles

HRTEM was employed to study the morphological structure of the starting material to synthesize the CNOs and the products obtained by the annealing process and by the oxidative treatments of the as-prepared CNOs (e.i. Ar/O_2 RF plasma and chemical oxidation in a HNO_3/H_2SO_4 mixture). The HRTEM image of the starting NDs particles (Figure 3.1a) shows the typical crystal lattice of diamond formed by the family of {111} planes, in agreement with previous reports [12]. After the annealing process, HRTEM images revealed quasi-spherical particles of 5 to 10 nm in diameter formed by several concentric graphitic shells, confirming the formation of the CNOs (Figure 3.1b). Inspection of HRTEM image of CNOs oxidized by using the Ar/O_2 RF plasma suggests that this treatment did not result in significant structural changes (Figure 3.1c). In contrast, the chemical oxidation of CNOs in the HNO_3/H_2SO_4 mixture (CNO-OXI) caused visible structural modifications which consist on a rougher outer shell (Figure 3.1d). It is known that the HNO_3/H_2SO_4 treatment is a very aggressive oxidation procedure that disrupts the external graphitic shells and creates surface defects of carbon materials [13].

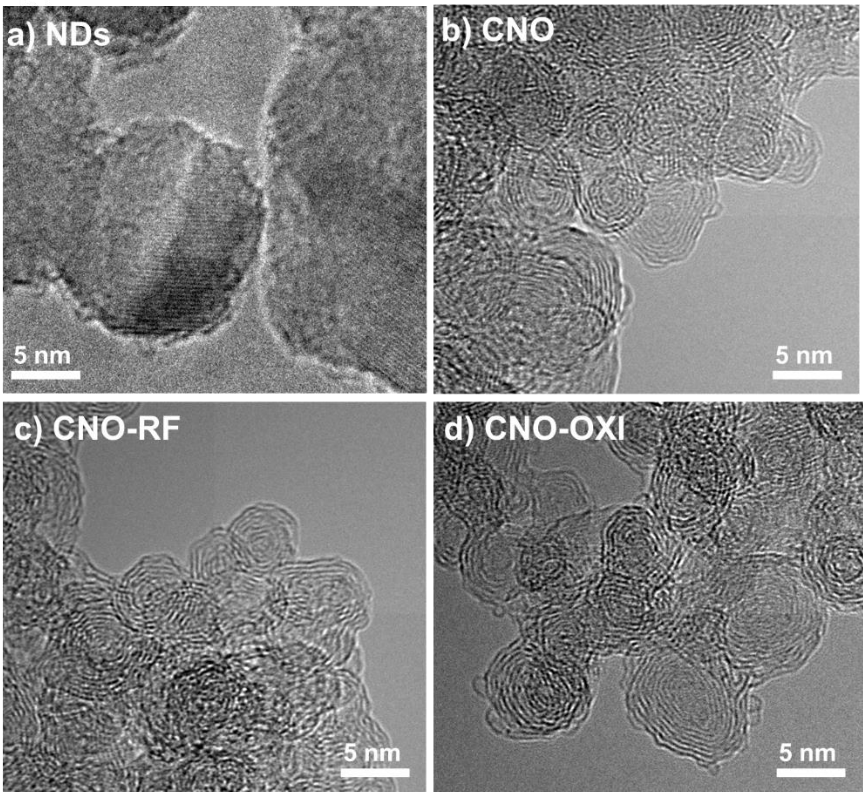

Figure 3.1. HRTEM images of a) starting NDs, b) CNOs, c) CNO-RF and d) CNO-OXI.

The Raman spectra of CNO [10], CNO-RF [10] and CNO-OXI [11] showed the D- and G-bands characteristic of graphitic carbon at about 1340 and 1580 cm^{-1}, respectively. The D to G band intensity ratios (I_D/I_G) for the studied CNO forms were 0.94, 1.01 and 1.7, respectively. This indicates that the defect density on the CNO was slightly increased by the Ar/O_2 RF plasma treatment, while it was almost doubled by oxidation in the HNO_3/H_2SO_4 mixture. These results are in line with the HRTEM analysis where visible defects on the outer-shell of CNO-OXI sample were observed.

Furthermore, the presence of surface defects can also be inferred from textural properties and capacitance measurements. The specific surface area (SSA) calculated from nitrogen adsorption/desorption measurements, and specific capacitances are listed in Table 3.1. The SSA of CNO was 273 m^2 g^{-1} and increased up to 333 m^2 g^{-1} when treated in the Ar/O_2 RF plasma, similar to what has been observed for CNOs before and after mild oxidation in air [14]. When CNO were oxidized with HNO_3/H_2SO_4, the SSA greatly increases up to 524 m^2 g^{-1}. This increase of the surface area by the oxidation of CNO is associated with a high concentration of defect (pores) possibly accompanied by the removal of a part of the outer shell of the CNOs caused by the oxidation process [14].

Table 3.1. Specific surface area (SSA), pore diameter and specific capacitances (C_s) for CNO, CNO-RF and CNO-OXI particles.

Sample	**SSA (m^2 g^{-1})**	**Pore diameter (nm)**	**C_s (F g^{-1})***
CNO	273	9.5	11.5
CNO-RF	333	11.5	21.9
CNO-OXI	524	12	66.1

* Calculated by integration of the cyclic voltammograms between -0.2 and 0 V vs. Ag/AgCl recorded in 0.1 mol L^{-1} $HClO_4$ at 0.1 V s^{-1}.

Additionally, the pore size distribution shows a pore size in the micropore region (~1.5 nm) and mesopores of about 9-12 nm, corresponding to interparticle and inter-cluster spaces between the

CNOs. These changes in the specific area are also associated with an increase in the specific capacitance of the materials [14]. Hence, the textural properties are in good agreement with HRTEM and Raman analysis and should be considered when explaining the electronic properties of the CNOs.

3.3.2 XPS analysis of the functional groups on CNO, CNO-RF and CNO-OXI

XPS analysis was carried out to estimate the chemical composition and identify the possible functional groups present on the surface of CNO, CNO-RF and CNO-OXI. In all survey spectra, the signatures of carbon and oxygen atoms were measurable in all particles. The oxygen atomic composition was 2.86, 4.27 and 5.98 atomic percent for CNO, CNO-RF and CNO-OXI, respectively, indicating an increased oxidation degree in that order.

Figure 3.2 presents the high-resolution XPS C 1s spectra of CNO, CNO-RF and CNO-OXI nanoparticles. All C 1s peaks were unsymmetrical which is characteristic of conducting forms of carbon [15]. For the as-prepared CNO, the main C 1s peak could be fitted with six components (Figure 3.2a). The main peaks centered at 284.4 and 284.7 eV can be assigned to sp^2 hybridized carbon atoms in strained C-C bonds due to the curvature of the onions [16]. The peak at 285.4 eV correspond to mixed sp^2+sp^3 hybridized carbon atoms [17]. The peak at 286.6 eV was assigned to phenolic OH groups. The other two peaks at 289.1 and 291.1 eV were assigned to carboxylic groups and a π-π* relaxation shake-up satellite peak, respectively [15]. The presence of oxygenated species on the surface of CNO prepared by the annealing of NDs have been also observed in a previous work [5] and it is in line with our results on the dispersibility of these CNO in some polar solvents (e.g. DMF and NMP) [7]. These oxygenated groups may be originated by the reaction of oxygen with the edges of incomplete graphitic layers containing highly reactive dangling bonds [18].

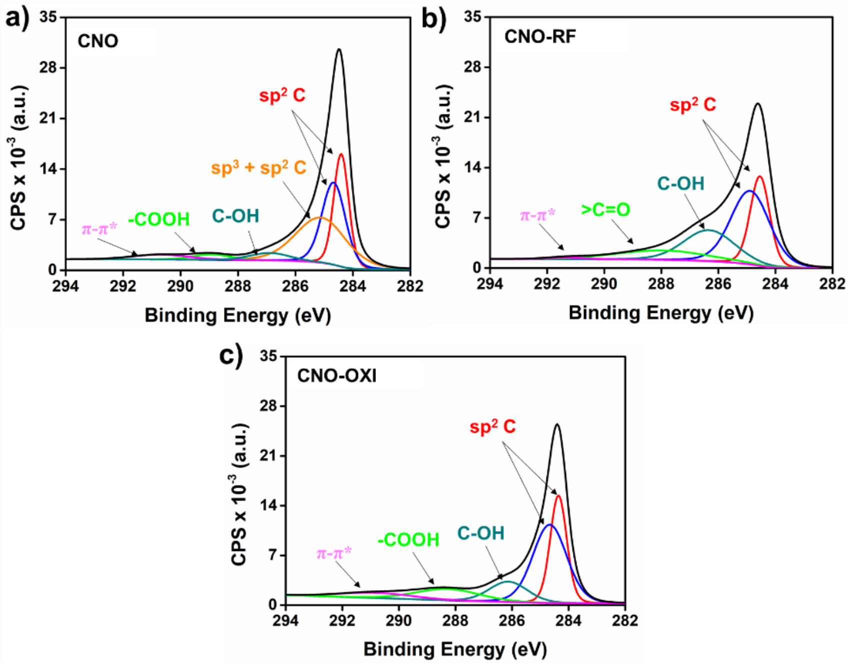

Figure 3.2. XPS spectra in the C 1s region and the fit components of a) CNO, b) CNO-RF, and c) CNO-OXI.

For the CNO-RF sample, the C 1s peak was deconvoluted into five components centered at 284.5, 284.8 (sp^2 hybridized carbon atoms), 286.1 (phenolic C-OH) and 288.1 (>C=O from carbonyl groups) and 291.4 eV (π-π* relaxation shake-up satellite) [10] (Figure 3.2b). These results indicate that the Ar/O_2 RF plasma treatment mildly oxidized the CNO introducing mainly carbonyl and hydroxyl groups onto the surface. In the case of the C 1s spectra of the CNO-OXI nanoparticles (Figure 3.2c), the peaks assigned to sp^2 hybridized carbon atoms were located at 284.4 and 284.7 eV. The peak at 286.1 eV could arise from carbon atoms bound to oxygen in the form of phenol groups or oxygen bridges -C-O-C-. The peaks at 288.3 and 291.3 eV correspond to carboxylic groups and the π-π^* relaxation shake-up satellite, respectively [19,20]. The integrated intensity of the carboxylic peak in the spectra for CNO-OXI sample increased 3.7 times relative to as-prepared CNO nanoparticles. Thus, the acid treatment of CNO mainly introduces new carboxylic acid moieties on the CNO surface. Similar XPS features have been previously described for oxidized CNO [21].

The relative intensities (expressed in %) of each fit component of the C 1s spectra and the O/C ratios of CNO, CNO-RF and CNO-OXI are summarized in Table 3.2. It is clear that oxidation of CNOs results in an increased number of oxygenated species bound to the carbon atoms of CNOs. It is also observed that there are significant differences between the oxidized CNOs. For the CNOs oxidized by Ar/O_2 RF plasma treatment, hydroxyl and carbonyl groups were mainly formed. For CNOs oxidized in the HNO_3/H_2SO_4 mixture, a higher oxygen content was found, and it was confirmed that carboxylic and phenol groups were preferentially formed, in contrast to the other dry oxidative treatment. These results suggest that different oxidative approaches could be used to introduce selectively different functional groups on the surface of CNOs.

Table 3.2. Curve fitting results of XPS C 1s spectra of CNO, CNO-RF and CNO-OXI.

Sample	**O/C ratio**	**Composition of the fit components (%)**					
		sp^2	**sp^2+sp^3**	**>C-OH**	**>C=O**	**COOH**	**π- π***
CNO	0.029	54.2	34.3	4.3	-	3.1	4.1
CNO-RF	0.045	64.8	-	22.2	12.1	-	0.9
CNO-OXI	0.064	70.0	-	12.4	-	11.5	6.1

3.3.3. Band structure and work function of CNO, CNO-RF and CNO-OXI

Figure 3.3 shows the UPS spectra of CNO, CNO-RF and CNO-OXI nanoparticles which provide the structure of the valence band of these materials. The intensity of the spectra is related with the density of states (DOS) of the samples under study. In the regions between -3 to -4 eV and -6 to -8 eV this intensity corresponds to the DOS of valence bands of $\pi_{p_z}$and $\sigma_{p_{x,y}}$ nature, respectively [22]. It is seen that the relative intensity of the π_{p_z}-derived DOS to the $\sigma_{p_{x,y}}$-derived DOS was smaller for CNO-RF and CNO-OXI than that of CNO. This means that π_{p_z} and $\sigma_{p_{x,y}}$ -derived DOS were noticeably affected by oxidative treatment due to the generation of structural defects and the introduction of different functional groups on the surface of CNOs, as indicated by the morphological, Raman and textural data.

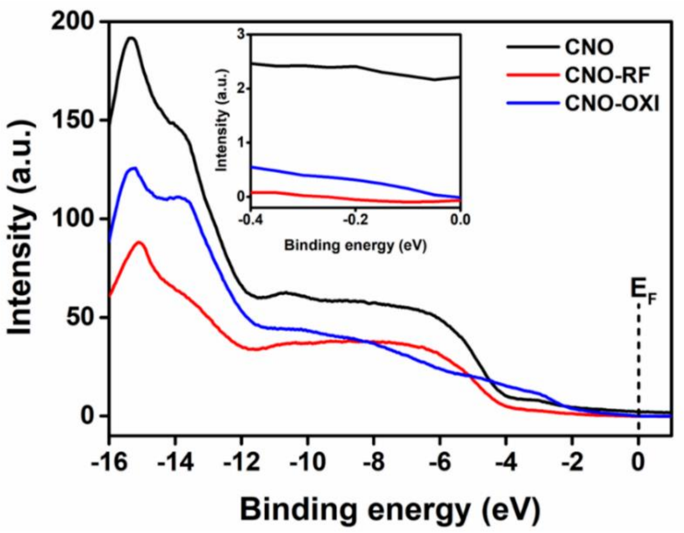

Figure 3.3. UPS spectra of CNO, CNO-RF and CNO-OXI. Inset: close-up of the UPS spectra in the 0 to -0.4 eV region. E_F corresponds to the Fermi level.

The inset in Figure 3.3 shows the valence band spectra near the Fermi level (E_F) of CNO, CNO-RF and CNO-OXI. It is interesting to note that the DOS near E_F of CNO and CNO-OXI is not zero, being the former the highest. This fact provides a strong indication of the metallic-like behavior of these two materials. STM experiments have shown that carbon nano-onions possess conductance values comparable to those of metallic nanowires [23]. Theoretical calculations of multi-shelled fullerenes indicate that the metallic properties of CNOs increase with the number of graphite shells [24–26]. Moreover, the difference in crystal structures of diamond and graphite results in an accumulation of different types of defects (five or seven atom rings, “Y” junctions of two graphite planes or an interstitial plane between two planes and vacancies) in the graphitic curved shells of CNO during the annealing process [5]. These defects are reflected in the appearance of the D band in the Raman spectrum of CNOs and lead to inter-shell and surface dangling bonds that generate a high density of states near de Fermi level [27]. All this contributes to CNOs to present metallic or semi-metallic characteristics.

As it was mentioned, the UPS spectrum of CNO-OXI shows lower DOS near the E_F than pristine CNO, whereas the metallic or semi-metallic characteristics were maintained (i.e. a non-zero DOS at the E_F). Thus, CNO-OXI has an electronic structure similar to that of pristine CNO except for the number of electronic states near the E_F. This change in the valence band of CNO after the oxidation in the HNO_3/H_2SO_4 mixture might be explained by i) the partial elimination of dangling bonds that contribute to the DOS near the E_F, ii) the creation of certain amount of holes in the outer-shells that disrupts the π conjugation of the graphitic layers as evidenced by textural measures, and iii) the introduction of oxygenated species (phenolic and carboxylic) which down-shift the DOS of the π_{p_z} states due to electron withdrawing characteristic of carboxylic moieties [28] as evidence by XPS. It has been shown that dangling bonds and carbon atoms located in structural defects are the first sites that are oxidized by the HNO_3/H_2SO_4 mixtures [29,30]. This also leads to the formation of holes on the graphitic shells as was observed on the HRTEM images of CNO-OXI and translated in an increase in specific surface area up to 524 $m^2\ g^{-1}$ and a higher I_D/I_G ratio in the Raman spectrum. However, it seems that the number of these holes was not too high to cause a drastic change in the electronic structure of the particle. On the other hand, the introduction of a high density of holes might result in the destruction of the concentric structure of the carbon nano-onions with a loss in their metallic characteristics.

Conversely, the UPS spectrum of CNO-RF revealed that the DOS is zero and hence no electronic states exist between E_F and -0.2 eV. This corresponds to the electronic characteristics of a semiconductor with a valence band located 0.2 eV below its E_F [31,32]. In this case, the electronic states disappeared near the E_F because of bonding between the graphitic π_{p_z} states and oxygen-related states to form carbonyl and hydroxyl groups. This produces electron transfer from sp^2 carbons to oxygen atoms resulting in a downward shift of the highest occupied molecular orbital (HOMO) state to higher binding energy and generate empty states just above the Fermi level which, in turn, opens a band gap [28,33]. Previous works provided some insight into the role of oxygen bonding on the electronic structure of some carbon materials [28,33,34]. They showed that increasing the amount of oxygen in the form of carbonyl and hydroxyl groups can modify the electronic structure of a carbon material from the metallic to a wide-bandgap semiconductor behavior. Thus, in the case of CNO-RF the observed changes in the valence band structure are due to electronic effects of the carbonyl and phenolic groups rather than due to the generation of structural defects as observed in CNO-OXI particles.

The work function (ϕ) of a material is another property that can be extracted from UPS experiments. The value of ϕ represents the minimum energy needed to remove an electron from the surface of a material to a point in the vacuum. Thus, ϕ indicates how below the vacuum level, the Fermi level of a material is [35]. Knowing the values of ϕ is very useful in the design of metal oxide–semiconductor field effect transistors [36], Schottky contacts [37], solid-state thermionics [38], etc. Moreover, since the values of ϕ depend on the structure and chemical composition of a surface, it is also a very useful piece of information in chemisorption process and in surface analysis [39]. The ϕ values of CNO, CNO-RF and CNO-OXI were determined from the secondary electron cutoff of UPS He I spectra. The results are listed in Table 3.3 together with those of multiwall carbon nanotubes (MWCNTs) and highly oriented pyrolytic graphite (HOPG) [40]. The CNO and CNO-RF nanoparticles have smaller ϕ values that MWCNTs and HOPG. This means that the binding energy of π-electrons for CNO and CNO-RF is smaller than that for MWCNTs and HOPG. The smaller ϕ values of CNO and CNO-RF might be explained in terms of the destabilization of the π-electrons due to curvature of the graphene sheets [41].This destabilization is also responsible of the higher reactivity of small CNO with respect to MWCNTs and larger CNOs prepared by arch discharge methods [6]. On the other hand, CNO-OXI shows a higher ϕ value (4.8 eV). This increase in ϕ could be explained by: i) a reduction of the π conjugation on the outer-shell of CNO-OXI and ii) an enhancement of surface dipoles because of the presence of oxygenated moieties [40].

Table 3.3. Work Functions of CNO, CNO-RF and CNO-OXI determined from the cutoff of the secondary electrons in UPS HeI spectra.

Sample	Work Function (eV)
CNO	4.3
CNO-RF	4.3
CNO-OXI	4.8
plasma oxidized MWCNTs	4.8
acid oxidized MWCNTs	5.1
HOPG	4.4

MWCNTs: multiwall carbon nanotubes, HOPG: highly oriented pyrolytic graphite. Data from reference [40].

3.3.4 Interfacial diagrams of CNO, CNO-RF and CNO-OXI

Interfacial electron transfer phenomena between two materials are very important in the design of electronic devices and also to explain some electrochemical behaviors. An approach to address this is to construct the respective interfacial energy diagrams [42]. These diagrams represent how the electronic densities of the two materials (in terms of DOS) vary over a same energy scale which is usually referred to the vacuum level. Since the ϕ of a material is indicative of how far below the vacuum level is the E_F, the construction of the diagrams is straightforward by summing the respective value of ϕ to the energy scale of each UPS spectra and plotting the resulting energy values *vs.* the DOS. Notice that in the case of UPS spectra, the DOS is plotted *vs.* energy. Figure 3.4 shows the interfacial energy diagram for CNO, CNO-RF and CNO-OXI resulting from lining up the UPS data with respect to the vacuum level. The relative positions of some redox systems were also represented, taking into account that the absolute potential of the Normal Hydrogen Electrode (NHE) recommended by IUPAC is 4.44 eV, (i.e. the NHE is 4.44 eV below the vacuum level) [43,44].

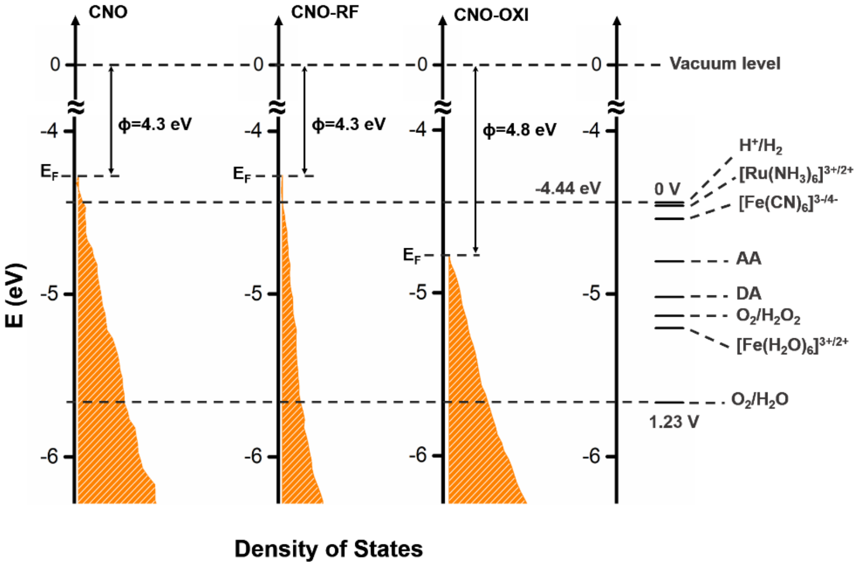

Figure 3.4. Interfacial energy diagrams for CNO, CNO-RF and CNO-OXI (left) and the relative position for different redox species (right). E_F: Fermi level, ϕ: work function, AA: ascorbic acid, DA: dopamine.

Figure 3.4 is helpful to explain the electrochemical activities of CNO, CNO-RF and CNO-OXI [45]. According to the Marcus–Hush–Chidsey theory of heterogeneous electron transfer (HET), the HET rate (k^0) might be dominated by the DOS of the electrode material [46]. Thus, k^0 increases when there are sufficient electronic states in the electrode with energies near the formal potential level of the redox probe involved [47]. From the formal potential level of the redox probes showed in Figure 3.4 and the available DOS of CNO, CNO-RF or CNO-OXI at these energy values, it could be expected that electron transfer takes place between these redox species and the CNO, CNO-RF or CNO-OXI electrodes. We have observed well-defined and peak-shaped redox waves in the cyclic voltammograms of these redox probes recorded at CNO, CNO-RF or CNO-OXI electrodes indicating a relatively fast electron transfer kinetics (see next Chapter or reference [48]). This clearly indicates that the relatively high DOS of these materials facilitates the direct electron transfer with the redox probe, in correspondence with the response observed in the cyclic voltammograms.

To further illustrate the applicability of the interfacial diagrams, we analyzed the redox probes $[Fe(CN)_6]^{3-}$ (inner-sphere) and $[Ru(NH_3)_6]^{3+}$ (outer-sphere) which are commonly used to benchmark different electrode materials [49]. In the case of $[Fe(CN)_6]^{3-}$, the DOS at the formal potential level of the redox couple follows the order CNO > CNO-RF > CNO-OXI. Thus, it would be expected that the electron transfer kinetics also follows this trend. Cyclic voltammograms (CVs) of 1 mmol L^{-1} $[Fe(CN)_6]^{3-}$ in 1 mol L^{-1} KCl recorded at CNO, CNO-RF or CNO-OXI modified electrodes presented anodic-to-cathodic peak separations of 67, 71 and 82 mV, respectively (Table 3.4). As result, the k^0 for $[Fe(CN)_6]^{3-}$ at CNO, CNO-RF or CNO-OXI also follows the trend CNO > CNO-RF > CNO-OXI with a slower electron transfer kinetics at CNO-OXI. It is interesting to note that the electron transfer kinetics of $[Fe(CN)_6]^{3–}$ might be influenced by the DOS of the electrode materials and its defect density [49]. However, in our case it seems that the DOS of the electrodes play a more important role in the electron-transfer kinetics than the defect density.

Table 3.4. Cyclic voltammetric data and calculated apparent heterogeneous electron transfer constants for $[Fe(CN)_6]^{3-}$ and $[Ru(NH_3)_6]^{3+}$ redox species.*

Parameter	**GCE/CNO**	**GCE/CNO-RF**	**GCE/CNO-OXI**
	1 mmol L^{-1} $[Fe(CN)_6]^{3-}$		
ΔE_p (mV)	67	71	82
k^0 (cm s^{-1})	0.0457	0.0361	0.0247
	1 mmol L^{-1} $[Ru(NH_3)_6]^{3+}$		
ΔE_p (mV)	60	68	52
k^0 (cm s^{-1})	0.0769	0.0365	0.0677

*ΔE_p: anodic-to-cathodic peak separation, k^0: apparent heterogeneous electron transfer rate constant calculated from the intercept of the Tafel plot of the anodic brand of the cyclic voltammogram. The supporting electrolyte was 1 mol L^{-1} KCl. Scan rate: 0.1 V s^{-1}. The geometric area of the electrode ($A_{electrode}$ = 0.070 cm^2).

On the other hand, in the case of the outer-sphere redox system $[Ru(NH_3)_6]^{3+}$, its electron transfer kinetics depends mainly on the DOS near the Fermi level of the electrode material [49]. From Figure 3.4, the DOS near the Fermi level follows the order CNO > CNO-OXI > CNO-RF. Thus, it would be expected that the k^0 values should also follow this order indicating the most sluggish kinetic at the CNO-RF surface. The kinetic data extracted from CVs of 1 mmol L^{-1} $[Ru(NH_3)_6]^{3+}$ in 1 mol L^{-1} KCl at CNO, CNO-RF and CNO-OXI modified electrodes were also listed in Table 3.4. It is observed that k^0 decreases from CNO (0.0769 cm s^{-1}) to CNO-OXI (0.0677 cm s^{-1}) and to CNO-RF (0.0365 cm s^{-1}). This is consistent with the decreasing DOS near the Fermi level from CNO to CNO-OXI and to CNO-RF and confirms the sluggish heterogeneous electron kinetics of $[Ru(NH_3)_6]^{3+}$ at CNO-RF in comparison with the other two materials.

These examples further demonstrate the applicability of the interfacial energy diagrams to explain the electrochemical properties of a material in the absence of other process like adsorption or specific chemical interactions with the electrode surface [50,51]. Additionally, these diagrams could be also employed to study the photophysical properties of these carbon nanomaterials [32,52].

3.4. Conclusions

In this Chapter, the electronic structure of CNOs and its oxidation products obtained by Ar/O_2 RF plasma and acid oxidation has been studied for the first time using ultraviolet and X-ray photoelectron spectroscopies. The as-prepared CNOs presented hydroxyl and carboxylic acid groups on the graphite shells and its electronic structure corresponds to a metallic state with a work function of 4.3 eV. The Ar/O_2 RF plasma oxidation of CNO introduces mainly hydroxyl and carbonyl groups and changes the electronic state to a semiconductor with a work function of 4.3 eV and a valence band located 0.2 eV below the Fermi level. The oxidation of CNO with a HNO_3/H_2SO_4 mixture resulted in visible morphological changes of the outer shells of CNO with the preferential introduction of hydroxyl and carboxylic acid moieties and an increase on the work functions (4.8eV) while preserving the metallic behavior. The changes in the electronic structures were explained in terms of a reduction of DOS π_{p_z}-derived valence band due to the elimination/generation of structural defects on the outer shells of CNO and the electronic effects that resulted from the introduction of different oxygen-containing functional groups.. The interfacial energy diagrams for CNO, CNO-RF and CNO-OXI were constructed and used to explain the electrochemical properties of these materials. These results provide new information about the properties of carbon nano-onions that could be useful in the design of novel electrochemical or photovoltaic devices.

References

[1] K. Ozawa, Ultraviolet Photoelectron Spectroscopy, in: Compend. Surf. Interface Anal., Springer Singapore, 2018: pp. 783–790.

[2] A. V. Okotrub, L.G. Bulusheva, V.L. Kuznetsov, A. V. Gusel'Nikov, A.L. Chuvilin, *Electronic state of nanodiamond/graphite interfaces*, Appl. Phys. A Mater. Sci. Process. 81 (2005) 393–398.

[3] L.G. Bulusheva, A. V. Okotrub, V.L. Kuznetsov, D. V. Vyalikh, *Soft X-ray spectroscopy and quantum chemistry characterization of defects in onion-like carbon produced by nanodiamond annealing*, Diam. Relat. Mater. 16 (2007) 1222–1226.

[4] A. V. Okotrub, L.G. Bulusheva, V.L. Kuznetsov, Y. V. Butenko, A.L. Chuvilin, M.I. Heggie, *X-ray emission studies of the valence band of nanodiamonds annealed at different temperatures*, J. Phys. Chem. A. 105 (2001) 9781–9787.

[5] Y. V. Butenko, S. Krishnamurthy, A.K. Chakraborty, V.L. Kuznetsov, V.R. Dhanak, M.R.C. Hunt, L. Šiller, *Photoemission study of onionlike carbons produced by annealing nanodiamonds*, Phys. Rev. B. 71 (2005) 075420.

[6] A. Palkar, F. Melin, C.M. Cardona, B. Elliott, A.K. Naskar, D.D. Edie, A. Kumbhar, L. Echegoyen, *Reactivity differences between carbon nano onions (CNOs) prepared by different methods*, Chem. – An Asian J. 2 (2007) 625–633.

[7] J.C. Zuaznabar-Gardona, A. Fragoso, *Determination of the Hansen solubility parameters of carbon nano-onions and prediction of their dispersibility in organic solvents*, J. Mol.

Liq. 294 (2019) 111646.

[8] O. V. Kharissova, C.M. Oliva González, B.I. Kharisov, *Solubilization and dispersion of carbon allotropes in water and non-aqueous solvents*, Ind. Eng. Chem. Res. 57 (2018) 12624–12645.

[9] J. Bartelmess, S. Giordani, *Carbon nano-onions (multi-layer fullerenes): chemistry and applications*, Beilstein J. Nanotechnol. 5 (2014) 1980–1998.

[10] J.P. Bartolome, A. Fragoso, *Preparation and characterization of carbon nano-onions by nanodiamond annealing and functionalization by radio-frequency Ar/O_2 plasma*, Fullerenes, Nanotub. Carbon Nanostructures. 25 (2017) 327–334.

[11] E. Wajs, A. Molina-Ontoria, T.T. Nielsen, L. Echegoyen, A. Fragoso, *Supramolecular solubilization of cyclodextrin-modified carbon nano-onions by host–guest interactions*, Langmuir. 31 (2015) 535–541.

[12] J. Xiao, G. Ouyang, P. Liu, C.X. Wang, G.W. Yang, *Reversible nanodiamond-carbon onion phase transformations*, Nano Lett. 14 (2014) 3645–3652.

[13] V. Datsyuk, M. Kalyva, K. Papagelis, J. Parthenios, D. Tasis, A. Siokou, I. Kallitsis, C. Galiotis, *Chemical oxidation of multiwalled carbon nanotubes*, Carbon. 46 (2008) 833–840.

[14] G. Moussa, C. Matei Ghimbeu, P.-L. Taberna, P. Simon, C. Vix-Guterl, *Relationship between the carbon nano-onions (CNOs) surface chemistry/defects and their capacitance in aqueous and organic electrolytes*, Carbon N. 105 (2016) 628–637.

[15] H. Estrade-Szwarckopf, *XPS photoemission in carbonaceous materials: A "defect" peak beside the graphitic asymmetric peak*, Carbon. 42 (2004) 1713–1721.

[16] D. Codorniu Pujals, D. Rodríguez Garcés, O. Arias de Fuentes, L.F. Desdín García, *XPS of carbon nanostructures obtained by underwater arc discharge of graphite electrodes*, Nucleus. (2011) 15–18.

[17] D. Codorniu Pujals, O. Arias de Fuentes, L.F. Desdín García, E. Cazzanelli, L.S. Caputi, *Raman spectroscopy of polyhedral carbon nano-onions*, Appl. Phys. A. 120 (2015) 1339–1345.

[18] R. Schlgl, M. Che, O. Clause, C. Marcilly, C. Louis, H. Kninger, E. Teglauer, W. Keim, B. Drieben-Hlscher, J.W.

Geus, A.J. van Dillen, J. Barbier, Preparation of solid catalysts: sections 2.1.9– 2.2.1.6, in: Handb. Heterog. Catal., Wiley-VCH Verlag GmbH, Weinheim, Germany, 1997: pp. 138–264.

[19] I.M. Rocha, O.S.G.P. Soares, J.L. Figueiredo, C. Freire, M.F.R. Pereira, *Bifunctionality of the pyrone functional group in oxidized carbon nanotubes towards oxygen reduction reaction*, Catal. Sci. Technol. 7 (2017) 1868–1879.

[20] E.J. Park, J.-H. Jin, J.H. Kim, N.K. Min, *Surface activation of plasma-patterned carbon nanotube based DNA sensing electrodes*, Microchim. Acta. 174 (2011) 231–238.

[21] M.E. Plonska-Brzezinska, M. Lewandowski, M. Błaszyk, A. Molina-Ontoria, T. Luciński, L. Echegoyen, *Preparation and characterization of carbon nano-onion/PEDOT:PSS composites*, ChemPhysChem. 13 (2012) 4134–4141.

[22] A. Bianconi, S.B.M. Hagström, R.Z. Bachrach, *Photoemission studies of graphite high-energy conduction-band and valence-band states using soft-X-ray synchrotron radiation excitation*, Phys. Rev. B. 16 (1977) 5543–5548.

[23] S. Sek, J. Breczko, M.E. Plonska-Brzezinska, A.Z. Wilczewska, L. Echegoyen, *STM-based molecular junction of carbon nano-onion*, ChemPhysChem. 14 (2013) 96–100.

[24] M. Pudlak, R. Pincak, *Energy gap between highest occupied molecular orbital and lowest unoccupied molecular orbital in multiwalled fullerenes*, Phys. Rev. A - At. Mol. Opt. Phys. 79 (2009) 033202.

[25] Y.L. Lin, F. Nori, *Electronic structure of single- and multiple-shell carbon fullerenes*, Phys. Rev. B. 49 (1994) 5020–5023.

[26] R. Pincak, V. V. Shunaev, J. Smotlacha, M.M. Slepchenkov, O.E. Glukhova, *Electronic properties of bilayer fullerene onions*, Fullerenes, Nanotub. Carbon Nanostructures. 25 (2017) 607–612.

[27] P. Ganesh, P.R.C. Kent, V. Mochalin, *Formation, characterization, and dynamics of onion-like carbon structures for electrical energy storage from nanodiamonds using reactive force fields*, J. Appl. Phys. 110 (2011) 073506.

[28] H.K. Jeong, C. Yang, B.S. Kim, K. Kim, *Valence band of graphite oxide*, Europhys. Lett. 92 (2010) 37005.

[29] J. Zhang, H. Zou, Q. Qing, Y. Yang, Q. Li, Z. Liu, X. Guo, Z. Du, *Effect of chemical oxidation on the structure of single-*

walled carbon nanotubes, J. Phys. Chem. B. 107 (2003) 3712–3718.

[30] S.A. Shamsuddin, M.N. Derman, U. Hashim, M. Kashif, T. Adam, N.H.A. Halim, M.F.M. Tahir, *Nitric acid treated multi-walled carbon nanotubes optimized by Taguchi method*, AIP Conf. Proc. 1756 (2016) 090002.

[31] D. Löffler, S. Ulas, S.S. Jester, P. Weis, A. Böttcher, M.M. Kappes, *Properties of non-IPR fullerene films versus size of the building blocks*, Phys. Chem. Chem. Phys. 12 (2010) 10671–10684.

[32] H. Ishii, K. Sugiyama, E. Ito, K. Seki, *Energy level alignment and interfacial electronic structures at organic/metal and organic/organic interfaces*, Adv. Mater. 11 (1999) 605–625.

[33] H.K. Jeong, L. Hong, X. Zhang, E. Vega, P.A. Dowben, *Evidence of band bending and surface Fermi level pinning in graphite oxide*, Carbon. 57 (2013) 227–231.

[34] A. Ganguly, S. Sharma, P. Papakonstantinou, J. Hamilton, *Probing the thermal deoxygenation of graphene oxide using high-resolution in situ X-ray-based spectroscopies*, J. Phys. Chem. C. 115 (2011) 17009–17019.

[35] E. Wimmer, A.J. Freeman, Fundamentals of the electronic structure of surfaces, in: Handb. Surf. Sci., Elsevier, 2000: pp. 1–91.

[36] S.K. Kurinec, Metal oxide–semiconductor field effect transistors, in: Encycl. Mater. Sci. Technol., 2nd ed., Elsevier, 2001: pp. 5461–5475.

[37] L.M. Porter, K. Das, Y. Dong, J.H. Melby, A.R. Virshup, Contacts to wide-band-gap semiconductors, in: Compr. Semicond. Sci. Technol., Elsevier Inc., 2011: pp. 44–85.

[38] G.D. Mahan, Thermionic refrigeration, in: Semicond. Semimetals, Academic Press Inc., 2001: pp. 157–174.

[39] C.T. Chan, K.M. Ho, K.P. Bohnen, Surface reconstruction: Metal surfaces and metal on semiconductor surfaces, in: Handb. Surf. Sci., Elsevier, 1996: pp. 101–136.

[40] H. Ago, T. Kugler, F. Cacialli, W.R. Salaneck, M.S.P. Shaffer, A.H. Windle, R.H. Friend, *Work functions and surface functional groups of multiwall carbon nanotubes*, J. Phys. Chem. B. 103 (1999) 8116–8121.

[41] X. Lu, Z. Chen, *Curved Pi-conjugation, aromaticity, and the related chemistry of small fullerenes (>C_{60}) and single-walled*

carbon nanotubes, Chem. Rev. 105 (2005) 3643–3696.

[42] C.G. Zoski, Handbook of Electrochemistry, 1st ed., Elsevier, 2007.

[43] S. Trasatti, *The absolute electrode potential: an explanatory note (Recommendations 1986)*, Pure Appl. Chem. 58 (1986) 955–966.

[44] V. Tripkovic, M.E. Björketun, E. Skúlason, J. Rossmeisl, *Standard hydrogen electrode and potential of zero charge in density functional calculations*, Phys. Rev. B - Condens. Matter Mater. Phys. 84 (2011) 115452.

[45] M.C. Granger, M. Witek, J. Xu, J. Wang, M. Hupert, A. Hanks, M.D. Koppang, J.E. Butler, G. Lucazeau, M. Mermoux, J.W. Strojek, G.M. Swain, *Standard electrochemical behavior of high-quality, boron-doped polycrystalline diamond thin-film electrodes*, Anal. Chem. 72 (2000) 3793–3804.

[46] M.C. Henstridge, E. Laborda, N. V. Rees, R.G. Compton, *Marcus-Hush-Chidsey theory of electron transfer applied to voltammetry: A review*, Electrochim. Acta. 84 (2012) 12–20.

[47] Y. Song, H. Hu, M. Feng, H. Zhan, *Carbon nanotubes with tailored density of electronic states for electrochemical applications*, ACS Appl. Mater. Interfaces. 7 (2015) 25793–25803.

[48] J.C. Zuaznabar-Gardona, A. Fragoso, *Electrochemistry of redox probes at thin films of carbon nano-onions produced by thermal annealing of nanodiamonds*, Electrochim. Acta. 353 (2020) 136495.

[49] R.L. McCreery, *Advanced carbon electrode materials for molecular electrochemistry*, Chem. Rev. 108 (2008) 2646–2687.

[50] R.H. Wopschall, I. Shain, *Adsorption effects in stationary electrode polarography with a chemical reaction following charge transfer*, Anal. Chem. 39 (1967) 1535–1542.

[51] P. Chen, R.L. McCreery, *Control of electron transfer kinetics at glassy carbon electrodes by specific surface modification*, Anal. Chem. 68 (1996) 3958–3965.

[52] D.M. Bobrowska, H. Zubyk, E. Regulska, E. Romero, L. Echegoyen, M.E. Plonska-Brzezinska, *Carbon nanoonion-ferrocene conjugates as acceptors in organic photovoltaic devices*, Nanoscale Adv. 1 (2019) 3164–3176.

Chapter 4

Electrochemistry of redox probes at thin films of carbon nano-onions produced by thermal annealing of nanodiamonds[3]

4.1. Introduction

Research in the electrochemistry of CNOs have been mainly focused on their capacitive properties for applications in supercapacitors. Most of these works dealt with methods to enhance the capacitive properties of CNOs by using chemical activation [1], pseudocapacitive metal oxides [2], or electrochemical oxidation [3]. On the other hand, few reports have explored other aspects of the electrochemistry of CNOs. The electrocatalytic activities of CNOs (25-35 nm) produced by arch-discharge have been investigated using coordination compounds ($[Fe(CN)_6]^{3-/4-}$, $[IrCl_6]^{2-/3-}$ and $[Fe(H_2O)_6]^{3+/2+}$) and neurotransmitters (dopamine, serotonin and norepinephrine) as electrochemical redox probes [4]. More recently, the electrochemical properties of composites of poly(diallyldimethylammonium chloride) (PDDA) and CNOs produced by annealing of nanodiamonds were compared with other carbon nanomaterials [5]. However, the electrochemical properties of CNOs without PDDA were not addressed nor the effect of the chemical functional groups of CNOs on their redox properties.

---

[3] *This Chapter is part of a published work in J.C. Zuaznabar-Gardona, A. Fragoso, Electrochimica Acta, 353 (2020) 136495.*

In this Chapter, we address the electroactivity of charged and neutral redox probes at electrodes modified with thin films of different CNOs produced by annealing of nanodiamonds. We also studied the effect of oxidation degree of CNOs on the redox activities of standard outer- and inner-sphere redox probes.

4.2. Materials and methods

$K_3[Fe(CN)]_6$, $(NH_4)_2Fe(SO_4)_2 \cdot 6H_2O$, $[Ru(NH_3)_6]Cl_3$, $HClO_4$ (60%), $FcCH_2OH$, nitric acid, sulfuric acid, KCl, and dimethylformamide (DMF) were purchased from Sigma-Aldrich (Spain) and were used as received. All solutions were prepared with double distilled water (18.2 MΩ cm) obtained from a Milli-Q® system (Millipore, Madrid, Spain). CNOs were prepared by thermal annealing of nanodiamonds and further oxidized by radio frequency Ar/O_2 plasma, and chemically oxidized as previously reported [6,7].

All electrochemical measurements were obtained using a PC-controlled CHI 660A electrochemical workstation (CH Instruments, Austin, USA) with a three-electrode cell configuration. A platinum wire was used as counter electrode and a commercial Ag/AgCl (sat) electrode serves as reference electrode. Glassy carbon electrodes (CH Instruments model CHI104, 3.0 mm diameter, 0.07 cm^2 geometric area) coated with pristine CNO, radio frequency Ar/O_2 plasma oxidized CNO (CNO-RF) or chemically oxidized CNO (CNO-OXI) films were used as working electrodes.

4.2.1. Electrode preparation

Prior to modification, bare GC electrodes (GCE) were first manually smoothed with emery paper # 600 followed by polishing to a mirror finish with 0.3 μm alumina slurries. The polished GCE were sonicated in Milli-Q® water for 5 min and dried under a stream of nitrogen. GCE were modified by drop-casting a homogeneous dispersion of CNO, CNO-RF or CNO-OXI in DMF (4 mg mL^{-1}) prepared using an ultrasonic-bath for 30 minutes. To obtain a thin layer of CNO, CNO-RF or CNO-OXI, 1 µL of the dispersion was cast twice on the surface of the electrodes and dried in an oven at 80ºC under DMF atmosphere for 30 minutes. This procedure was used to avoid the formation of the so called coffee-ring effect which results in non-homogeneous films [8].

4.2.2. Surface analysis of CNO, CNO-RF and CNO-OXI modified GC electrodes

The surface of GC electrodes modified with CNO, CNO-RF and CNO-OXI were examined by environmental scanning electron microscopy (ESEM) and X-ray photoemission spectroscopy (XPS) conducted at Catalan Institute of Nanoscience and Nanotechnology (ICN2) facilities in Barcelona, Spain. ESEM images were recorded in a Quanta 600 microscope (FEI Company, Inc.) under high vacuum at 25 kV. Samples were analyzed at a 10-mm working distance. XPS experiments were performed at room temperature with a SPECS PHOIBOS 150 hemispherical analyzer at 10 eV pass energy using monochromatic Al Kα (1486.74 eV) radiation as excitation source in a base pressure of 10^{-10} mbar. High-resolution XPS spectra were deconvoluted using CasaXPS v 2.3.19 processing software.

4.2.3. Electrochemistry at CNO, CNO-RF and CNO-OXI modified GC electrodes

The intrinsic electrochemical properties of GC electrodes modified with CNO, CNO-RF and CNO-OXI were investigated by means of cyclic voltammetry (CV) and electrochemical impedance spectroscopy (EIS) in 0.2 mol L^{-1} $HClO_4$ solutions as electrolyte. The electrolytes were deoxygenated by purging pure N_2 gas for about 20 min, and the gas was kept flowing over the liquids during the electrochemical measurements. CV was performed in different potential windows in the range of -1 to 1 V at a scan rate of 0.1V s^{-1}. EIS measurements were done at a constant frequency (400 Hz) by scanning the dc potential from -0.5 to 0.9 V at a scan rate of 0.01 V s^{-1} and a sinusoidal ac potential with 10 mV amplitude was superimposed on dc potential. From the EIS data, the value of the double layer capacitance (C_d) at the electrode-electrolyte interface was derived using the following equation [9]:

$$C_d = -\frac{1}{2\pi f Z"} \qquad (1)$$

where f is the frequency used in the EIS measurement and $Z"$ is the imaginary component of impedance. The resulting dependence of C_d on electrode potential E (i.e. C_d vs E curves) of all surfaces under study were deconvoluted using the peak-fitting software Fityk v1.3.1 as was recently reported [10].

Furthermore, the voltammetric responses of GC electrodes modified with CNO, CNO-RF and CNO-OXI were also assessed by means of CV using 1 mmol L^{-1} $[Fe(CN)_6]^{3-}$, 1 mmol L^{-1} $[Ru(NH_3)_6]^{3+}$ and 0.16 mmol L^{-1} $FcCH_2OH$, all in 1 mol L^{-1} KCl and 1 mmol L^{-1}

$[Fe(H_2O)_6]^{2+}$ in 0.2 mol L^{-1} $HClO_4$. The peak-to-peak separation (ΔE_p), anodic and cathodic peak current density ratio (j_{pa}/j_{pc}) and anodic peak current density (j_{pa}) were extracted from cyclic voltammograms recorded at $0.1 Vs^{-1}$ of scan rate. No correction was made for double-layer or iR effects. The apparent heterogeneous electron transfer constants (k^o) for the redox probes were calculated from the intercept of the linear part of the Tafel plot according to the following equation [11]:

$$\ln(I) = \frac{\alpha F\left(E - E_f^0\right)}{RT} + \ln(AFk^0 c(X)) \qquad (2)$$

where I is the current from the anodic brand of the voltammogram, α is the anodic transfer coefficient, F is the Faraday constant (96 485 C mol^{-1}), E is the potential of the working electrode, E_f^0 is the formal potential, R is the gas constant (8.314 J mol^{-1} K^{-1}), T is the absolute temperature, A is the geometric area of the electrode in cm^2, k^0 is the standard rate constant and c(X) is the concentration of the redox species in mol L^{-1}.

4.3. Results and discussion

4.3.1. ESEM and XPS analysis of GC surfaces modified with CNO, CNO-RF and CNO-OXI

CNO, CNO-RF and CNO-OXI dispersions were deposited by casting an aliquot on the surface of the GC electrodes. The stationary air-drying of these dispersions resulted in non-uniform films due to the manifestation of the so-called ‘coffee-ring’ effect [12]. To obtain uniform films of CNO, CNO-RF and CNO-OXI, we adapted a procedure to deposit Pt/C catalyst dispersions on electrode surfaces

[8]. It consisted in drying the aliquot of the dispersions on the electrode surface in an oven at 80 ^{0}C under DMF atmosphere. Figure 4.1(a-c) depicts ESEM images of CNO, CNO-RF and CNO-OXI films on GC electrodes. The films prepared using this procedure did not present appreciable coffee-ring effect and their microscopic topographies were markedly rough as observed in the ESEM images.

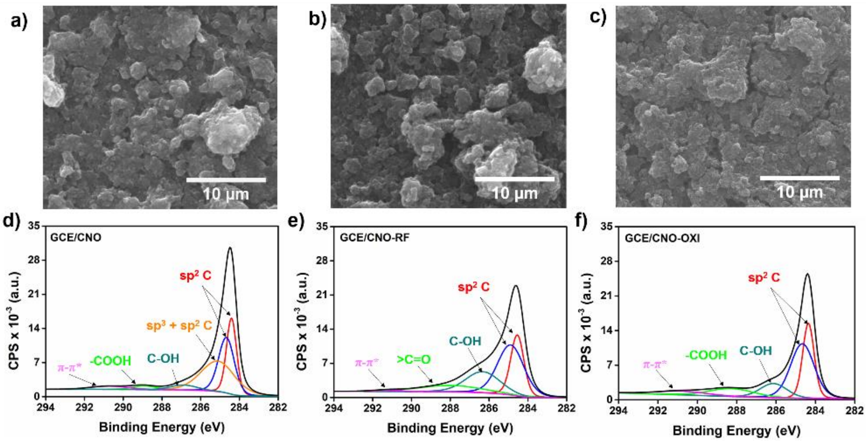

Figure 4.1. ESEM images (top) and high resolution XPS spectra in the C 1s region (bottom) of GCE/CNO (a, d), GCE/CNO-RF (b, e) and GCE/CNO-OXI (c, f).

XPS analysis was also carried out to estimate the chemical composition and identify the possible functional groups present on the surface of CNO, CNO-RF and CNO-OXI deposited on GC electrodes. Figures 4.1d-f present the high-resolution XPS C1s spectra and the fit components into which the spectra were deconvoluted for the modified surfaces. The energy positions and the percentages of each component of the spectrum deconvolution are summarized in Table 4.1. In general, phenol groups and sp^2 hybridized carbon atoms in strained C=C bonds due to the curvature of the onions were identified in all samples [13]. Additionally, carboxylic groups were detected in the GCE/CNO and in higher proportion (ca. 4 times) in the GCE/CNO-OXI surfaces. In contrast, carbonyl groups were found in the GCE/CNO-RF surface. Similar XPS features have been previously described for pristine and oxidized CNOs [14]. This indicates that different oxidation procedures result in the introduction of different oxygenated species on the CNO surface.

Table 4.1. Curve fitting results of XPS C 1s spectra of GC surface modified with CNO, CNO-RF and CNO-OXI.

		Sample		
		CNO	CNO-RF	CNO-OXI
Binding Energy (eV) / fractional area (%) of the fit components	**O/C ratio**	0.029	0.045	0.064
	$\boldsymbol{sp_a^{2*}}$	284.4/25.4	284.5/24.5	284.4/28.0
	$\boldsymbol{sp_b^{2*}}$	284.7/28.9	284.9/40.3	284.7/42.0
	$\boldsymbol{sp^2 + sp^3}$	285.1/34.3	-	-
	>C-OH	286.8/4.3	286.1/22.2	286.1/12.4
	>C=O	-	288.1/12.1	-
	-COOH	288.9/3.1	-	288.3/11.5
	$\boldsymbol{\pi\text{-}\ \pi^*}$	290.7/4.1	291.4/0.8	291.3/6.1

*sp_a^2 and sp_b^2 refer to sp^2 hybridized carbon atoms in non- and strained C=C bonds due to the curvature of graphene sheets in the CNOs, respectively.

4.3.2. Electrochemical properties of GC surfaces modified with CNO, CNO-RF and CNO-OXI

As mentioned before, research works on the electrochemistry of CNO have been mainly focused on their capacitive properties. The inherent electrochemistry as well as the effect oxygen containing groups on the redox responses of CNO have not been fully addressed. Thus, here we attempt to overcome this studying the electrochemical response of GC electrodes modified with CNO, CNO-RF and CNO-OXI toward different electroactive species.

Figure 4.2a shows cyclic voltammograms (CVs) at CNO, CNO-RF and CNO-OXI modified GC electrodes in 0.2 mol L^{-1} $HClO_4$ solution. All CVs exhibit a pseudo-rectangular shape which is characteristic of the electric double layer capacitive behavior of CNOs [15]. The capacitive current increases with the oxidation degree of CNO due to the presence of functional groups on their surface as reported previously and confirmed by XPS analysis [3]. In addition to the capacitive current, anodic and cathodic peaks at 0.37 and 0.30 V (vs. Ag/AgCl), respectively, are also observed in the CVs of electrodes modified with CNO-OXI. The peak currents were found to vary linearly with the scan rate, indicating that the redox process was due to redox species confined on the surface of CNO-OXI (Figure 4.2b). This faradaic process was also observed at electrodes modified with CNO and CNO-RF, but with much lower current intensity than that for CNO-OXI.

The effect of pH on the electrochemical behavior of CNO-OXI film was also investigated by recording cyclic voltammograms at different pH (Figure 4.2c). Cathodic and anodic peak potentials shifted negatively with increasing pH. It was found that the peak position of both peaks depended linearly on the pH according to the equations: $E_{pa}=0.41-0.061\times pH$ and $E_{pc}=0.35-0.064\times pH$. E_{pa} and E_{pc} are the peak position for anodic and cathodic signal, respectively (Figure 4.2d). The slopes of the plots of E_{pa} (0.061 V pH^{-1}) and E_{pc} (0.064 V pH^{-1}) vs pH were very close to the theoretical values of 0.059 V pH^{-1} at 25°C for a redox process involving as many protons as electrons. The number of electrons involved on the redox process was estimated by the approximation proposed by Laviron [16]. It assumes that for a surface confined redox specie, the width at mid-height of the redox peaks tends towards 90.6/n mV at low scan rates, where n is the total number of electrons involved in the redox process. Thus, from a CV recorded at 25 mV s^{-1}, n was estimated to be 4.3 electrons. According to the results mentioned above, the peaks observed at GCE/CNO-OXI electrodes might correspond to a redox process where carboxylic acid groups are the electroactive species.

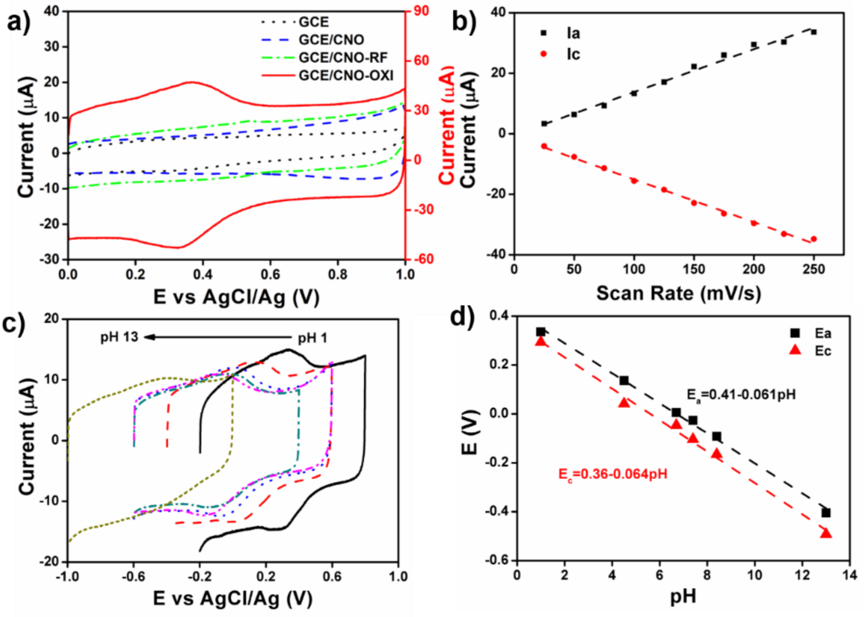

Figure 4.2. a) Cyclic voltammograms for GCE modified with CNO, CNO-RF and CNO-OXI recorded in 0.2 mol L^{-1} $HClO_4$. Scan rate: 0.1 V s^{-1}. b) Dependence of anodic and cathodic peak currents with scan rate of the redox couple observed for GCE/CNO-OXI in 0.2 mol L^{-1} $HClO_4$. c) Cyclic voltammograms of GCE/CNO-OXI at pH 1, 4.5, 6.7, 7.4, 8.5 and 13. d) Plot of oxidation and reduction peak potentials as a function of pH corresponding to (c).

The -COOH groups are reduced to $-CH_2OH$ in a four-proton/four-electron process (Scheme 4.1). Similar redox pair and identification of the electroactive species were proposed for oxidized single-walled carbon nanotubes and CNO films [1,17,18]. However, it should be mentioned that redox processes of phenolic and pyrone groups probably found in CNO-OXI surface can also occur in the same potential range and have the same pH dependence as the obtained here [3,19]. Thus, it might be possible that the redox peaks showed in Figure 4.2a were the result of simultaneous redox processes involving different oxygenated functional groups.

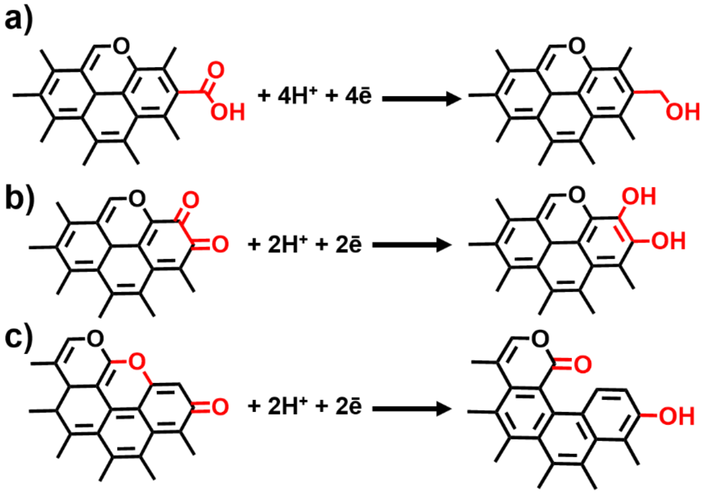

Scheme 4.1. Half-equations for the reduction of a) carboxylic, b) hydroquinoid/quinoid and c) pyrone groups present in carbon materials.

To go further on this aspect, the dependence of the capacitance of the double layer (C_d) on the applied potential (i.e. C_d vs E curves) were determined by means of EIS at fixed frequency in a potential window between -0.5 and 0.9 V in 0.1 mol L^{-1} $HClO_4$ (Figure 4.3). The purpose of these measurements was to determine the presence of individual electroactive functional groups (e.g. phenol, carbonyl, carboxyl, quinoid, etc.) from the shape of C_d vs. E curves as reported recently [10,20]. Figure 4.3a shows the C_d vs. E curves for bare, CNO, CNO-RF and CNO-OXI modified electrodes. The C_d value increases with the degree of oxidation of CNO and the occurrence of a pseudo-capacitance maximum around 0.30 V confirmed the presence of electroactive functional groups on all CNO surfaces [20,21]. Moreover, each peak consists of several overlapping peaks which indicates the contribution of functional groups of different types on C_d. Gaussian peak deconvolution of the pseudo-capacitance maximum of the C_d vs E curves resulted in two main redox responses present in all electrode surfaces (Figure 4.3b-d). This is in agreement with the XPS results, that reveal the presence of two different oxygenated groups on each of the modified surfaces, i.e phenol and carboxylic on CNO and CNO-OXI and phenol and carbonyl on CNO-RF. The deconvoluted peak at higher potential (peak A) is centered at 0.30 V for all surfaces. In contrast, the peak at lower potential (peak B) is centered at the same potential (0.18 V) for CNO and CNO-OXI modified electrodes while for CNO-RF modified electrodes the peak is shifted to more cathodic potentials (0.0 V). This indicates that peak B might correspond to different electroactive species. Accordingly, peak A could be fairly assigned to the response of the phenolic groups which are present on all modified surfaces [20] while peak B could be assigned to the carboxylic moieties present in CNO and CNO-OXI modified electrodes and to the carbonyl groups present in CNO-RF.

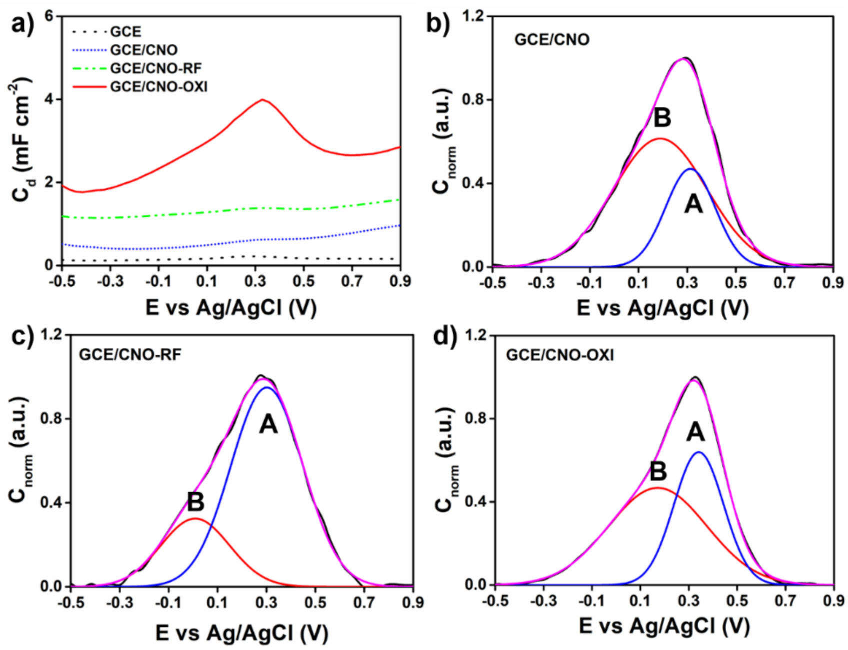

Figure 4.3. a) Capacitance of the double layer (C_d) vs applied potential (E) for bare, CNO, CNO-RF and CNO-OXI modified glassy carbon electrodes measured in 0.1 mol L^{-1} $HClO_4$ by EIS at 400 Hz from -0.5 to 0.9 V. b-d) Normalized capacitance (C_{norm}) and Gaussian deconvolution fits of the pseudo-capacitance maximum for CNO, CNO-RF and CNO-OXI modified electrodes, respectively. The C_{norm} vs E curves were obtained by normalizing the C_d values to its corresponding pseudo-capacitance maximum.

4.3.3. Voltammetry of redox probes at CNO, CNO-RF and CNO-OXI modified GC electrodes

The electrochemical responses of 1 mmol L^{-1} $[Fe(CN)_6]^{3-}$, 1 mmol L^{-1} $[Ru(NH_3)_6]^{3+}$, 0.16 mmol L^{-1} $FcCH_2OH$ in 1 mol L^{-1} KCl and for 1 mmol L^{-1} $[Fe(H_2O)_6]^{2+}$ in 0.2 mol L^{-1} $HClO_4$ on bare and CNO, CNO-RF and CNO-OXI modified electrodes were studied by cyclic voltammetry (Figure 4.4). These redox probes were chosen to assess the effect of the oxidation degree of CNO on their electrochemical properties. The peak-to-peak separation (ΔE_p), anodic and cathodic peak current density ratios (j_{pa}/j_{pc}), anodic current density

($j_a = I_{pa}/A_{electroactive}$) and apparent heterogeneous electron transfer rate constants (k^0) for the different redox probes are summarized in Table 4.2. Rate constants were calculated from the intercept of the Tafel plot in the current range from 1% to 99% of the anodic peak current [11].

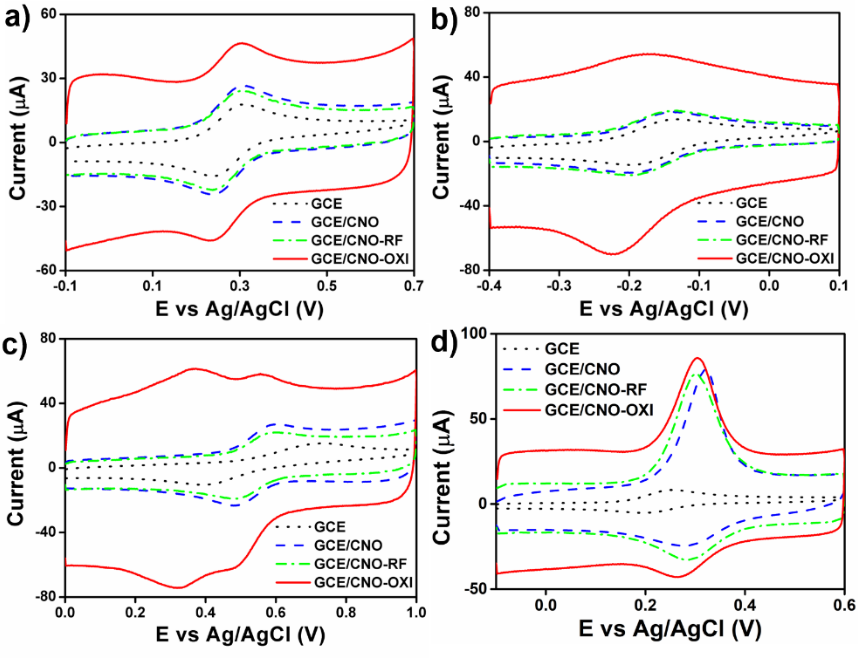

Figure 4.4. Cyclic voltammograms of a) 1 mmol L^{-1} $[Fe(CN)_6]^{3-}$ in 1 mol L^{-1} KCl, b) 1 mmol L^{-1} $[Ru(NH_3)_6]^{3+}$ in 1 mol L^{-1} KCl, c) 1 mmol L^{-1} $[Fe(H_2O)_6]^{2+}$ in 0.2 mol L^{-1} $HClO_4$, and d) 0.16 mmol L^{-1} $FcCH_2OH$ in 1 mol L^{-1} KCl at GCE, GCE/CNO, GCE/CNO-RF and GCE/CNO-OXI electrodes. Scan rate: 0.1 V s^{-1}.

Table 4.2. Cyclic voltammetry data and calculated apparent heterogeneous electron transfer constants for $[Fe(CN)_6]^{3-}$, $[Ru(NH_3)_6]^{3+}$, $[Fe(H_2O)_6]^{2+}$ and $FcCH_2OH$ redox probes.*

Parameter	GCE	GCE/CNO	GCE/CNO-RF	GCE/CNO-OXI
1 mmol L^{-1} $[Fe(CN)_6]^{3-}$				
ΔE_p (mV)	68	67	71	82
j_{pa}/j_{pc}	1.0	1.0	0.9	0.8
j_a (mA cm^{-2})	0.7	0.7	0.6	0.5
k^0 (cm s^{-1})	0.0295	0.0457	0.0361	0.0247
1 mmol L^{-1} $[Ru(NH_3)_6]^{3+}$				
ΔE_p (mV)	68	60	68	52
j_{pa}/j_{pc}	1.0	1.0	0.9	0.2
j_a (mA cm^{-2})	0.6	1.0	0.7	0.3
k^0 (cm s^{-1})	0.0333	0.0769	0.0365	0.0677
1 mmol L^{-1} $[Fe(H_2O)_6]^{2+}$				
ΔE_p (mV)	320	120	132	46
j_{pa}/j_{pc}	1.1	1.0	0.9	0.3
j_a (mA cm^{-2})	0.3	0.6	0.5	0.2
k^0 (cm s^{-1})	0.0084	0.0282	0.0224	0.0517
0.16 mmol L^{-1} $FcCH_2OH$				
ΔE_p (mV)	58	42	14	40
j_{pa}/j_{pc}	1.5	5.9	3.3	2.8
j_a (mA cm^{-2})	0.3	2.6	2.7	1.9
k^0 (cm s^{-1})	0.0164	0.1192	0.1862	0.1530

* The supporting electrolyte was 1 mol L^{-1} KCl for $[Fe(CN)_6]^{3-}$, $[Ru(NH_3)_6]^{2+}$ and $FcCH_2OH$ and 0.2 mol L^{-1} $HClO_4$ for $[Fe(H_2O)_6]^{2+}$. Scan rate: 0.1 V s^{-1}. k^o values determined from the intercept of the Tafel plot of the anodic brand of the cyclic voltammogram. Oxidation peak currents are normalized to the electroactive area of the electrodes which are 0.0215, 0.0257, 0.0241 and 0.0289 cm^2 for GCE, GCE/CNO, GCE/CNO-RF and GCE/CNO-OXI electrodes respectively.

For $[Fe(CN)_6]^{3-}$ (Figure 4.4a), the main difference observed was the higher ΔE_p value of the $[Fe(CN)_6]^{3-/4-}$ redox pair at the GCE/CNO-OXI electrodes in comparison with the other modified surfaces. This increase in the ΔE_p might be due to repulsive interactions between the $[Fe(CN)_6]^{3-}$ anions and the carboxylate groups on the surface of the GCE/CNO-OXI electrodes which result in a hindered electron transfer. On the other hand, the electrochemical responses of $[Fe(CN)_6]^{3-}$ on CNO, CNO-RF and CNO-OXI were lower than CNOs prepared by arc-discharge methods [4]. The electron transfer of $[Fe(CN)_6]^{3-}$ is sensitive to the density of exposed edge planes of the electrode material [22]. CNOs prepared by arc-discharge method possess a higher density of exposed edge-planes and defects than the CNO prepared here. Thus, it would be expected that CNOs prepared by annealing of nanodiamonds induce a lower electrochemical response of the $[Fe(CN)_6]^{3-/4-}$ redox pair than arc-discharge CNOs.

The $[Ru(NH_3)_6]^{3+}$ complex was employed as outer sphere redox probe (Figure 4.4b). A small peak separation (60 mV) near the ideal value (59 mV) was obtained with GCE/CNO electrodes in comparison to those obtained with GCE and GCE/CNO-RF electrodes. The electron transfer kinetics of $[Ru(NH_3)_6]^{3+}$ is primarily affected by the electronic properties of the electrode, specifically the density of electronic states (DOS) near the formal potential of the redox system [22]. Thus, the improved electron transfer kinetics for GCE/CNO electrodes might be the result of a higher DOS of the CNO in comparison with the other two materials as it was described in Chapter 3. Previous X-ray emission studies of the valence band of CNO prepared by annealing of nanodiamonds also revealed an increase in the DOS of CNOs when compared to HOPG [23]. In the case of the GCE/CNO-OXI, the response of $[Ru(NH_3)_6]^{3+}$ was mainly influenced by the attractive electrostatic interactions between the carboxylic moieties on GCE/CNO-OXI and the positive charge probe. As a result, an asymmetric voltammogram with a j_{pc} higher than j_{pa} and a $\Delta E_p < 59$ mV was observed. This asymmetry in the voltammograms is characteristic when redox species are physisorbed on the electrode surface [24].

Figure 4.4c shows cyclic voltammograms for the $[Fe(H_2O)_6]^{2+}$ redox probe. The modification of the GC electrodes with CNO, CNO-RF and CNO-OXI resulted in significantly smaller ΔE_p in comparison with a bare GC electrode. The electron transfer kinetics of the $[Fe(H_2O)_6]^{2+/3+}$ redox couple is very sensitive to the presence of oxygenated species on the surface due to their oxophylic character [25]. Hence, the k^0 values increased about 3 (at GCE/CNO and GCE/CNO-RF) and 6 times (at GCE/CNO-OXI) with respect to GCE, consistent with an increase in the number of oxygenated functional groups on the modified surfaces. In the case of GCE/CNO-OXI electrodes, ΔE_p was 46 mV with a j_{pa}/j_{pc} equal to 0.3 which indicates that the $[Fe(H_2O)_6]^{2+}$ cations were physisorbed on the surface probably by electrostatic interactions as in the case of $[Ru(NH_3)_6]^{3+}$. This peak is overlapped in part with the organic redox pair at 0.3 V observed for the CNO-OXI surface.

$FcCH_2OH$ was also studied, in this case as a neutral redox probe (Figure 4.4d). Considerably higher peak current values were obtained with the CNO, CNO-RF and CNO-OXI modified electrodes respect to unmodified GC electrodes. This increase was also higher than those obtained when metal complexes were employed as redox probes. The asymmetric shape of the voltammograms with $\Delta E_p < 59$ mV and $j_{pa}/j_{pc} \neq 1$ for all modified electrodes also indicated interfacial adsorption. In particular, the high current values of the anodic peaks respect to the cathodic peak suggest weak adsorption of the reduced molecular form of $FcCH_2OH$ on the electrode surface. Interestingly, the j_{pa}/j_{pc} ratio decreases as the oxygen content increases. Additionally, anodic peaks were also widened in the same trend. This widening is due to the reduction of attractive forces between the molecules of the reduced form of $FcCH_2OH$ on the electrode surface [26]. The differences between CNO, CNO-RF and CNO-OXI might be explained in terms of the π-π interaction between the $FcCH_2OH$ molecules and the surface of CNO. The oxidation of CNO results in the partial rupture of the sp^2 framework of the graphene outer-shell. This rupture reduces the number of contact points for effective π-π interactions taking place. Thus, weaker interactions would be expected between the cyclopentadienyl rings of $FcCH_2OH$ and the surface of oxidized CNO in comparison with pristine CNOs. As a result, the j_{pa}/j_{pc} would be expected to decrease as the oxidation degree of CNOs increases.

The voltammetric data presented above reveal that the electroactivity of $[Fe(CN)_6]^{3-/4-}$ and $[Ru(NH_3)_6]^{2+/3+}$ redox pairs were enhanced at the CNO, CNO-RF and CNO-OXI modified electrodes. In both cases, the j_a/j_c values decrease in the order GCE/CNO < GCE/CNO-RF < GCE/CNO-OXI and correlate well with the Raman I_D/I_G band intensity ratios [16,17], which also decrease in the same order and suggests that the adsorption of these two redox labels was favored by increasing the defect density and functional groups on the electrode surface. The k^o for each probe are in the order or greater than unmodified GC electrodes or other carbon-based nanomaterials [27,28]. Relative fast electron transfer kinetics was also obtained for the $[Fe(H_2O)_6]^{3+/2+}$ redox pair due to the presence of oxygen containing functional groups on the surface of CNO, CNO-RF and CNO-OXI. On the other hand, the electrochemical response of $FcCH_2OH$ was dictated by the adsorption of its reduced form which was favored at the less polar GCE/CNO electrodes than at GCE/CNO-RF and GCE/CNO-OXI. This behavior of $FcCH_2OH$ at the GCE/CNO surface will be discussed in more details in the next chapter.

4.4. Conclusions

In summary, we investigated and compared the electrochemical properties of pristine CNOs, radio frequency Ar/O_2 plasma oxidized CNO (CNO-RF) and chemically oxidized CNO (CNO-OXI) deposited on glassy carbon electrodes (GCE). The intrinsic electrochemical properties of CNO, CNO-RF and CNO-OXI modified electrodes were markedly influenced by the presence of different oxygenated functional groups as confirmed by XPs analysis and pseudo-capacitance measurements. CNO, CNO-RF and CNO-OXI modified electrodes exhibit fast electron transfer to $[Fe(CN)_6]^{3-}$, $[Ru(NH_3)_6]^{3+}$, $[Fe(H_2O)_6]^{2+}$ and $FcCH_2OH$ redox probes. The electrode kinetics for $[Fe(CN)_6]^{3-}$ and $[Ru(NH_3)_6]^{3+}$ probes at CNO and CNO-RF modified electrodes were sensitive to the relative density of state of the electrodes while at CNO-OXI electrodes, the electrode kinetics was affected by the electrostatic interactions between the redox probes and the functional groups on the surface of CNO-OXI. Relative fast electron transfer kinetics was also obtained for the $[Fe(H_2O)_6]^{3+/2+}$ redox pair due to the presence of oxygen containing functional groups on the surface of CNO, CNO-RF and CNO-OXI. For $FcCH_2OH$ the electrochemical response was dictated by the adsorption of its reduced form $[FcCH_2OH]^0$. Such adsorption was more favored at the GCE/CNO electrodes than at GCE/CNO-RF and GCE/CNO-OXI. The electrochemical data obtained here can serve as an all-important benchmark for CNO modified electrode performance.

References

[1] M.E. Plonska-Brzezinska, A.T. Dubis, A. Lapinski, A. Villalta-Cerdas, L. Echegoyen, *Electrochemical properties of oxidized carbon nano-onions: DRIFTS-FTIR and Raman spectroscopic analyses*, ChemPhysChem. 12 (2011) 2659–2668.

[2] R. Borgohain, J. Li, J.P. Selegue, Y.T. Cheng, *Electrochemical study of functionalized carbon nano-onions for high-performance supercapacitor electrodes*, J. Phys. Chem. C. 116 (2012) 15068–15075.

[3] Y. Liu, D.Y. Kim, *Enhancement of capacitance by electrochemical oxidation of nanodiamond derived carbon nano-onions*, Electrochim. Acta. 139 (2014) 82–87.

[4] R. Borgohain, J. Yang, J.P. Selegue, D.Y. Kim, *Controlled synthesis, efficient purification, and electrochemical characterization of arc-discharge carbon nano-onions*, Carbon. 66 (2014) 272–284.

[5] J. Yang, Y. Zhang, D.Y. Kim, *Electrochemical sensing performance of nanodiamond-derived carbon nano-onions: comparison with multiwalled carbon nanotubes, graphite nanoflakes, and glassy carbon*, Carbon. 98 (2016) 74–82.

[6] J.P. Bartolome, A. Fragoso, *Preparation and characterization of carbon nano-onions by nanodiamond annealing and*

functionalization by radio-frequency Ar/O$_2$ plasma, Fullerenes, Nanotub. Carbon Nanostructures. 25 (2017) 327–334.

[7] E. Wajs, A. Molina-Ontoria, T.T. Nielsen, L. Echegoyen, A. Fragoso, *Supramolecular solubilization of cyclodextrin-modified carbon nano-onions by host–guest interactions*, Langmuir. 31 (2015) 535–541.

[8] K. Shinozaki, J.W. Zack, S. Pylypenko, B.S. Pivovar, S.S. Kocha, *Oxygen reduction reaction measurements on platinum electrocatalysts utilizing rotating disk electrode technique*, J. Electrochem. Soc. 162 (2015) F1384–F1396.

[9] A.J. Bard, L.R. Faulkner, Electrochemical methods : fundamentals and applications, 2nd ed., Wiley, 2001.

[10] S. Hasoň, V. Ostatná, M. Fojta, *Simultaneous voltammetric determination of free tryptophan, uric acid, xanthine and hypoxanthine in plasma and urine*, Electrochim. Acta. 329 (2020) 135132.

[11] D. Li, C. Lin, C. Batchelor-McAuley, L. Chen, R.G. Compton, *Tafel analysis in practice*, J. Electroanal. Chem. 826 (2018) 117–124.

[12] R.D. Deegan, O. Bakajin, T.F. Dupont, G. Huber, S.R. Nagel, T.A. Witten, *Capillary flow as the cause of ring stains from dried liquid drops*, Nature. 389 (1997) 827–829.

[13] D. Codorniu Pujals, D. Rodríguez Garcés, O. Arias de Fuentes, L.F. Desdín García, *XPS of carbon nanostructures obtained by underwater arc dis- charge of graphite electrodes*, Nucleus. (2011) 15–18.

[14] M.E. Plonska-Brzezinska, M. Lewandowski, M. Błaszyk, A. Molina-Ontoria, T. Luciński, L. Echegoyen, *Preparation and characterization of carbon nano-onion/PEDOT:PSS composites*, ChemPhysChem. 13 (2012) 4134–4141.

[15] E. Frackowiak, K. Metenier, V. Bertagna, F. Beguin, *Supercapacitor electrodes from multiwalled carbon nanotubes*, Appl. Phys. Lett. 77 (2000) 2421–2423.

[16] E. Laviron, *General expression of the linear potential sweep voltammogram in the case of diffusionless electrochemical systems*, J. Electroanal. Chem. Interfacial Electrochem. 101 (1979) 19–28.

[17] H. Luo, Z. Shi, N. Li, Z. Gu, Q. Zhuang, *Investigation of the electrochemical and electrocatalytic behavior of single-wall carbon nanotube film on a glassy carbon electrode*, Anal.

Chem. 73 (2001) 915–920.

[18] M.E. Plonska-Brzezinska, A. Palkar, K. Winkler, L. Echegoyen, *Electrochemical properties of small carbon nano-onion films*, Electrochem. Solid-State Lett. 13 (2010) K35.

[19] Y.J. Oh, J.J. Yoo, Y. Il Kim, J.K. Yoon, H.N. Yoon, J.-H. Kim, S. Bin Park, *Oxygen functional groups and electrochemical capacitive behavior of incompletely reduced graphene oxides as a thin-film electrode of supercapacitor*, Electrochim. Acta. 116 (2014) 118–128.

[20] S.I. Stevanović, V. V. Panić, A.B. Dekanski, A. V. Tripković, V.M. Jovanović, *Relationships between structure and activity of carbon as a multifunctional support for electrocatalysts*, Phys. Chem. Chem. Phys. 14 (2012) 9475–9485.

[21] J.F. Evans, T. Kuwana, *Introduction of functional groups onto carbon electrodes via treatment with radio-frequency plasmas*, Anal. Chem. 51 (1979) 358–365.

[22] M.C. Granger, M. Witek, J. Xu, J. Wang, M. Hupert, A. Hanks, M.D. Koppang, J.E. Butler, G. Lucazeau, M. Mermoux, J.W. Strojek, G.M. Swain, *Standard electrochemical behavior of high-quality, boron-doped polycrystalline diamond thin-film electrodes*, Anal. Chem. 72 (2000) 3793–3804.

[23] A. V. Okotrub, L.G. Bulusheva, V.L. Kuznetsov, Y. V. Butenko, A.L. Chuvilin, M.I. Heggie, *X-ray emission studies of the valence band of nanodiamonds annealed at different temperatures*, J. Phys. Chem. A. 105 (2001) 9781–9787.

[24] R.H. Wopschall, I. Shain, *Effects of adsorption of electroactive species in stationary electrode polarography*, Anal. Chem. 39 (1967) 1514–1527.

[25] P. Chen, M.A. Fryling, R.L. McCreery, *Electron transfer kinetics at modified carbon electrode surfaces: the role of specific surface sites*, Anal. Chem. 67 (1995) 3115–3122.

[26] N. Kurapati, P. Pathirathna, R. Chen, S. Amemiya, *Voltammetric measurement of adsorption isotherm for ferrocene derivatives on highly orientedpyrolytic graphite*, Anal. Chem. 90 (2018) 13632–13639.

[27] K. Matsubara, K. Waki, *The effect of O-functionalities for the electrochemical reduction of oxygen on MWCNTs in acid media*, Electrochem. Solid-State Lett. 13 (2010) F7.

[28] H.-J. Zhang, H. Li, X. Li, B. Zhao, J. Yang, *Electrocatalysis of oxygen reduction on carbon nanotubes with different*

surface functional groups in acid and alkaline solutions, Int. J. Hydrogen Energy. 39 (2014) 16964–16975.

Chapter 5

Electrochemical characterization of the adsorption of ferrocenemethanol on carbon nano-onion modified electrodes[4]

5.1. Introduction

Carbon based materials are ubiquitous in modern electrochemistry [1,2]. Glassy carbons, carbon fibres and cloths, nanotubes, graphene, diamond-like carbons, nanodiamonds or carbon-dots are intensively studied for applications in electroanalysis, electrocatalysis, fuel cells, supercapacitor, electronics, etc [3,4]. Despite the extensive available literature on the structural, chemical and electrochemical properties of these materials ([4] and references therein), it is often difficult to understand the relationship between properties and applications due to the complexity of these systems. This is more difficult in the case of less studied carbon allotropes like the family of multilayer fullerenes also known as carbon nano-onions (CNOs). These materials show interesting properties for different electrochemical applications. For example, CNOs have been used as metal-free electrocatalysts for the reduction of oxygen and hydrogen peroxide [5,6]. They exhibit high capacity and excellent cycling performance as anode materials in lithium-ion batteries and electrochemical supercapacitors [7,8]. These properties of CNOs stem from their exohedral structure (convex curvature) that facilitates the access of

---

[4] *This Chapter was published in J.C. Zuaznabar-Gardona, A. Fragoso, Journal of Electroanalytical Chemistry, 871 (2020) 114314.*

the electrolyte ions and the formation of the double layer on the outer-shell of CNOs instead of pores as in other materials [9]. Our group has applied CNO-modified electrodes in the construction of a sensitive biosensors to detect Human Papilloma Virus and IgA antibodies [10,11]. In both cases, a marked increase in amperometric response and biosensor sensitivity has been observed when compared with analogous systems without CNOs. The origin of this sensitivity enhancement has been explained in terms of an increased surface area and improved electron transfer provided by the immobilized CNOs. However, it could be possible that the redox mediators or the products of the enzymatic reactions used as analytical signals interact to some extent with the CNO layer resulting in an enhanced sensitivity. Thus, further studies are required to explain this phenomenon.

Ferrocene and its derivatives are popular as benchmark redox systems to assess the electroactivity of electrodes [12], and as redox mediators in several electrochemical biosensors [13]. This popularity relies on the fact that these metallocenes undergo fast outer-sphere electron transfer on noble metal electrodes [14]. In water, the redox process of ferrocene is not as simple as in organic solvents as it involves a weak electrode and electrolyte dependent adsorption on glassy carbon electrode (GCE) surfaces [15]. Evidence of ferrocene adsorption has also been found on GC electrodes modified with multiwalled carbon nanotubes [16]. Moreover, recent works demonstrated that (ferrocenylmethyl)trimethylammonium ions, ferrocenecarboxylic acid and ferrocenemethanol ($FcCH_2OH$) can also adsorb up to a monolayer onto highly oriented pyrolytic graphite

(HOPG) surfaces [12]. The adsorption of $FcCH_2OH$ onto chemical vapour deposited graphene and mildly oxidized graphene has been also reported [17,18]. In the case of the mildly oxidized graphene, the adsorption of $FcCH_2OH$ induces an enhancement of the heterogeneous electron transfer rate [18]. Hence, the adsorption of ferrocene and its derivatives onto electrode surfaces has a clear impact on their voltammetric responses [19], and it is a parameter to take into account in order to understand the electrochemistry of nanocarbon-based electrodes. In this Chapter, we present a cyclic voltammetry (CV) and double step chronocoulometry study of the electrochemical response of $FcCH_2OH$ on GC electrodes modified with carbon nano-onions (GCE/CNO) and compare its behaviour with $[Fe(CN)_6]^{3-}$ as inner-sphere redox probe in an attempt to explain the sensitivity enhancement observed in the presence of CNOs.

5.2. Materials and methods

Dimethylformamide (DMF), $FcCH_2OH$, $K_3[Fe(CN)_6]$, and KCl were purchased from Sigma-Aldrich (Spain) and were used as received. Nanodiamonds (particle size: 2-8 nm) were obtained from TCI Europe BV and used as received. All solutions were prepared with double distilled water (18.2 MΩ cm) obtained from a Milli-Q® system (Millipore, Madrid, Spain). CNOs were prepared by thermal annealing of nanodiamonds under inert atmosphere as reported elsewhere [20].

5.2.1. Electrode preparation

Prior to modification, bare GC electrodes (GCE) were first manually smoothed with emery paper # 600 followed by polishing to a mirror finish with 0.3 μm alumina slurries. The polished GCE were sonicated in Milli-Q® water for 5 min and dried under a stream of nitrogen. GCE were modified by drop-casting a homogeneous dispersion of CNOs in DMF (4 mg mL^{-1}) prepared using an ultrasonic-bath for 30 minutes. To obtain a thin layer of CNO, 1 µL of the dispersion was cast twice on the surface of the electrodes and dried in an oven at 80ºC under DMF atmosphere for 30 minutes. This procedure was used to avoid the formation of the so called coffee-ring effect which results in non-homogeneous films [21].

5.2.2. Cyclic voltammetry and chronocoulometry measurements

Electrochemical measurements were obtained using a PC-controlled CHI 660A electrochemical workstation (CH Instruments, Austin, USA) with a three-electrode cell configuration. A platinum wire was used as counter electrode and a commercial Ag/AgCl (sat) electrode serves as reference electrode. Glassy carbon electrodes (CH Instruments model CHI104, 3.0 mm diameter, 0.07 cm^2 geometric area) coated with CNO films were used as working electrodes.

Cyclic voltammetry (CV) and double potential step chronocoulometry (DPSC) were used to quantify the adsorption of the redox species at CNO modified GC electrodes (GCE/CNO). CV at different scan rates (0.025 to 2 V s^{-1}) and DPSC (pulse width = 100 milliseconds) were performed from -0.1 to 0.6 V in 1 mol L^{-1} KCl containing $[Fe(CN)_6]^{3-}$ or $FcCH_2OH$ as redox probes. Simulations of cyclic voltammetry experiments were performed using the in-built CV simulator implemented in the controlling software for the CHI 660A potentiostat.

5.3. Results and discussion

Figure 5.1 shows the CVs of $[Fe(CN)_6]^{3-}$ and $FcCH_2OH$ at bare and CNO modified GC electrodes. For $[Fe(CN)_6]^{3-}$, identical peak-to-peak separation ($\Delta E_p = 65$ mV), similar peak current intensities and equal anodic and cathodic peak current ratios ($I_a/I_c = 1$) are observed on both GCE and GCE/CNO electrodes. On the other hand, CVs of $FcCH_2OH$ recorded at GCE/CNO show a markedly higher peak current (ca. 9 times) and lower ΔE_p (42 mV) than those at unmodified GC electrodes. Additionally, the CV presented an increased anodic peak with respect to the cathodic peak with an I_a/I_c ratio equal to 5.9. This voltammetric behaviour of $FcCH_2OH$, is a clear signature of adsorption of its reduced form with the oxidized form ($[FcCH_2OH]^+$) diffusing into solution as evidenced by the much smaller cathodic peak [19].

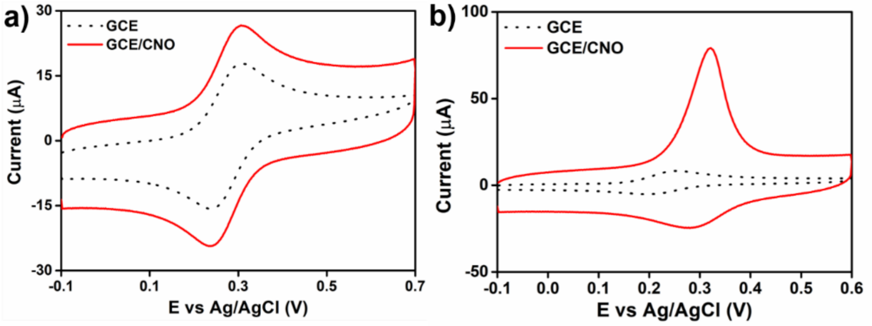

Figure 5.1. Cyclic voltammograms of a) 1 mmol L^{-1} $[Fe(CN)_6]^{3-}$ and b) 0.16 mmol L^{-1} $FcCH_2OH$ in 1 mol L^{-1} KCl at GCE and GCE/CNO electrodes. Scan rate: 0.1 V s^{-1}

Cyclic voltammetry is very useful to determine whether and to what extension redox probes adsorb on the surface of electrodes. In the presence of strongly adsorbed molecules, a separate adsorption peak may occur prior to or after the normal peak observed for a fully diffusion-controlled process. On the other hand, when redox probes are weakly adsorbed on the electrode surface, the CVs may exhibit an enhancement of the peak currents where the I_a/I_c ratio differs from unity [19]. According to this and the results showed in Figure 5.1, we could qualitatively infer that the electrochemistry of $FcCH_2OH$ probe is affected by the adsorption of its reduced form on GCE and GCE/CNO electrodes, while the electrochemistry of $[Fe(CN)_6]^{3-}$ is a fully diffusion-controlled process at these two surfaces. To address qualitatively this problem, we carried out voltammetric and chronocoulometric analysis to corroborate the adsorption of $FcCH_2OH$ on GCE/CNO and GC electrodes.

Scan rate is the most useful parameter to differentiate the effect due to species arriving at the electrode by diffusion and those adsorbed on the surface [19]. In a diffusion-controlled process, the ratio of anodic to cathodic peak currents (I_a/I_c) is equal to 1 and remains constant for increasing values of the scan rates. Conversely, if redox species adsorb on the electrode, the values of I_a/I_c will be different than unity and vary with the scan rates due to the different behaviour of the adsorbed oxidised and reduced forms. The CVs at increasing scan rates of 1 mmol L^{-1} $[Fe(CN)_6]^{3-}$ and 0.16 mmol L^{-1} $FcCH_2OH$ in 1 mol L^{-1} KCl at GCE/CNO are shown in Figures 5.2a and 5.2b, respectively. In both cases, I_a and I_c increase with the scan rate up to 2 V s^{-1}. For $FcCH_2OH$, I_a and I_c are shifted anodically and cathodically, respectively, which is a signature of the adsorption of $FcCH_2OH$ on the GCE/CNO surface. The variations of the I_a/I_c ratio with the square root of the scan rate ($\upsilon^{1/2}$) for $[Fe(CN)_6]^{3-}$ and $FcCH_2OH$ are presented in Figure 5.2c. For $[Fe(CN)_6]^{3-}$, I_a/I_c is independent on $\upsilon^{1/2}$ as expected for a fully diffusion-controlled process. In contrast, the I_a/I_c ratio for $FcCH_2OH$ decreases with $\upsilon^{1/2}$, indicating a voltammetric process regulated by the adsorption of the reduced form of $FcCH_2OH$ and the diffusion of its oxidized form $[FcCH_2OH]^+$ into solution [19]. This behaviour has also been reported on other carbon-based electrodes and point out the necessity to take adsorption into account when studying the electrochemical properties in these systems [12,18].

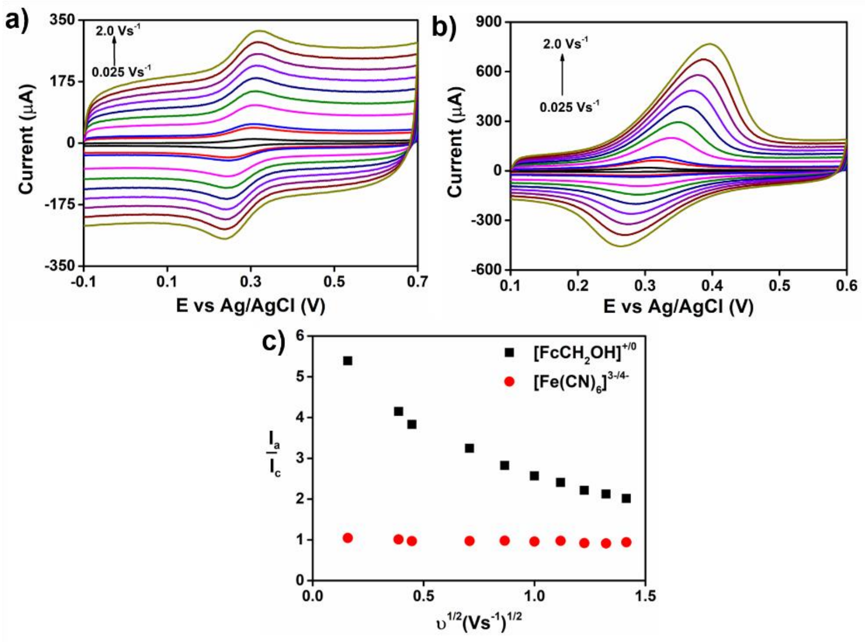

Figure 5.2. CVs of a) 1 mmol L^{-1} $[Fe(CN)_6]^{3-}$ and b) 0.16 mmol L^{-1} $FcCH_2OH$ in 1 mol L^{-1} KCl at the GCE/CNO electrode at increasing scan rates. b) Anodic peak to cathodic peak ratio (I_a/I_c) plotted vs the square root of scan rate ($\upsilon^{1/2}$) for the CVs shown in panels a) and b). Scan rates: 0.025, 0.15, 0.2, 0.5, 0.75, 1, 1.25, 1.5, 1.75 and 2 V s^{-1}.

The surface concentration of $FcCH_2OH$ (Γ) on GCE and GCE/CNO was estimated using the methodology proposed by Unwin et al [12]. It considers that Γ of a weakly adsorbed redox specie can be estimated from the difference between the experimental peak current density (j_{exp}) of a forward voltammetric wave and the simulated (j_{sim})

value based on a diffusion-controlled redox reaction as expressed by equation 1:

$$j_{exp} - j_{sim} = \Delta I_p = \frac{n^2 F^2 \Gamma}{4RT} \nu \qquad (1)$$

where n is the number of transferred electrons (n = 1 for the $[FcCH_2OH]^{+/0}$ redox pair), F is the Faraday constant (96 485 C mol^{-1}), R is the gas constant (8.314 J mol^{-1} K^{-1}), T is the absolute temperature and υ is the scan rate in V s^{-1}. Thus, Γ is estimated from the slope of a Δj_p *vs.* ν plot. The peak current difference (Δj_p) plotted vs scan rate (ν) for the voltammetric data shown in Figure 5.2b is given in Figure 5.3.

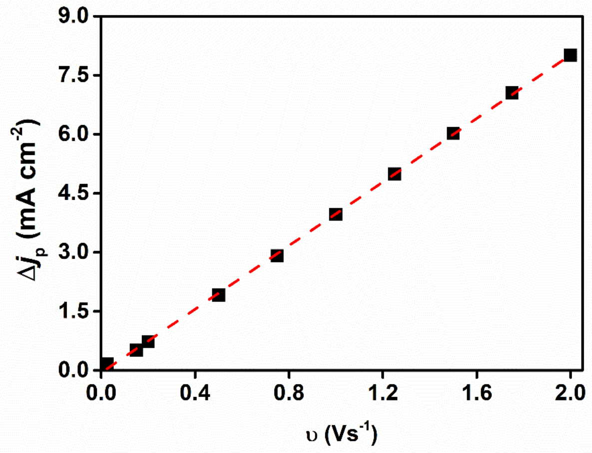

Figure 5.3. Peak current density difference ($\Delta j_p = j_{exp} - j_{sim}$) for the anodic wave of 0.16 mmol L^{-1} $FcCH_2OH$ at GCE/CNO electrode plotted versus scan rate (ν). Scan rates: 0.025, 0.15, 0.2, 0.5, 0.75, 1, 1.25, 1.5, 1.75 and 2 V s^{-1}.

The obtained dependency between Δj_p and ν was lineal as predicted by equation 1 and Γ was estimated to be 4.3×10^{-9} mol cm^{-2}. In contrast, the value of Γ on GC was 14-times smaller (3.0×10^{-10} mol cm^{-2}). From crystallographic data and assuming a closed-packed arrangement, the maximum surface coverage of the reduced form of $FcCH_2OH$ was estimated as 3.5×10^{-10} mol cm^{-2} [22]. This indicates that adsorbed $FcCH_2OH$ form a multilayered arrangement on the GCE/CNO surface. Interestingly, this value is higher than the coverage found previously for thionine on GCE/CNO ($\Gamma=2.7\times10^{-9}$ mol cm^{-2}) [23], and for ferrocene adsorbed in GC electrodes modified with multi-walled carbon nanotubes ($\Gamma=1.7\times10^{-9}$ mol cm^{-2}) [16].

The surface concentration of $FcCH_2OH$ on the GCE/CNO surface suggests the occurrence of intermolecular lateral interactions that favour the adsorption process. Lateral interactions can be estimated from the voltammetric peak width at half height (FWHM) as described by Laviron [24]. The relation is expressed as:

$$FWHM = \frac{2RT}{nF}\left[ln\left(\frac{1+\beta}{1-\beta}\right) - vG\theta_T\beta\right] \quad (2)$$

$$\beta = \sqrt{\frac{2-vG\theta_T}{4-vG\theta_T}} \quad (3)$$

where R, T, n, F have their usual meaning, v is the number of water molecules displaced by one adsorbed molecule, θ_T corresponds to the total fractional surface coverage and G comprises all possible interactions between the adsorbed molecules in the different redox states. The term $vG\theta_T$ in equations 2 and 3 is known as Laviron's interaction parameter. It expresses the overall interactions of adsorbed molecules on the electrode surface and define the shape of the voltammetric peaks. If $vG\theta_T < 0$ repulsive forces predominate which results in a wide, flat and round voltammetric peak, whereas if $0 < vG\theta_T < 2$ attractive forces are dominant and the peak is high, sharp and narrow. The values for $vG\theta_T$ were estimated by numeric solution of equation 2 using the *vpasolve* function implemented in MATLAB®. The values of FWHM for the anodic peak were extracted from the voltammograms given in Figure 5.1b. For the $FcCH_2OH$ adsorbed on GC surface, the $vG\theta_T$ parameter had a marked negative value (-1.7) indicative of the presence of strong repulsive lateral interactions between $FcCH_2OH$ molecules on the GC surface. Meanwhile, in the case of the GCE/CNO surface, the $vG\theta_T$ was 0.21, indicative of attractive forces.

To further study $FcCH_2OH$ adsorption on GCE/CNO and GC electrodes, double potential step chronocoulometry (DPSC) was used to obtain the respective empirical adsorption isotherms. DPSC allows to estimate the surface coverage of adsorbed redox molecules from the intercept of the Anson plots for the forward and reverse potential step, according to the equation:

$$\Gamma = \frac{Q_f - Qr}{nFA} \quad (4)$$

where Q_f and Q_r are the intercept of the Anson plot for the forward and reverse potential step of DPSC, respectively, n is the number of electrons transferred in the redox reaction, F is the Faraday constant and A is the geometric surface area of the electrode [25]. DPSC at increasing bulk concentration of $FcCH_2OH$ in 1 mol L^{-1} KCl recorded at GCE/CNO electrodes are presented in Figure 5.4a. The charge consumed for the oxidation and reduction of $FcCH_2OH$ increases with the bulk concentration. Chronocoulograms with similar trend but with smaller charges were obtained at GC electrodes (data not shown).

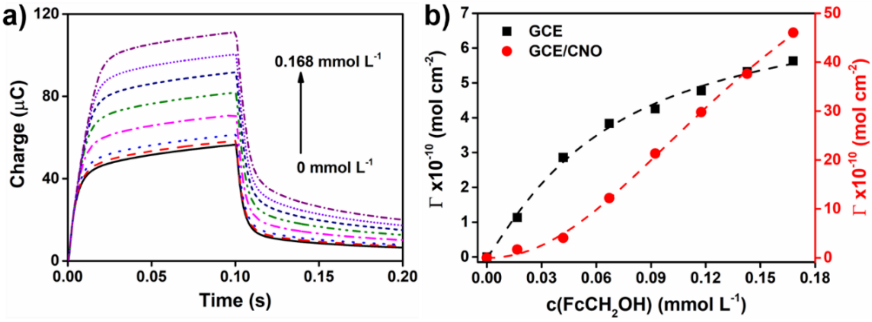

Figure 5.4. a) Double potential step chronocoulometry at increasing concentrations of FcCH$_2$OH recorded at GCE/CNO electrode in 1 mol L^{-1} KCl. b) Empirical adsorption isotherm of FcCH$_2$OH on GC and GCE/CNO electrode surfaces. Bulk concentrations: 0, 0.016, 0.042, 0.067, 0.092, 0.117, 0.143, 0.168 mmol L^{-1}.

The empirical adsorption isotherms (surface concentration vs. bulk concentration (c_0)) calculated from the DPSC experiments in the range 0-0.168 mmol L^{-1} are presented in Figure 5.4b. As expected, the surface coverage of FcCH$_2$OH increases with c_0 but in different way at GCE/CNO and GC electrode surfaces. On the GC surface, the variation of Γ with c_0 seems to have a concave shape typical for Langmuir or Temkin isotherms. In contrast, for the GCE/CNO surface, the isotherm has a convex shape. This is a signature of attractive interactions between adsorbate molecules on the surface and it is in line with the positive values obtained for the Laviron's interaction parameter ($vG\theta_T = +0.21$) obtained for FcCH$_2$OH on GCE/CNO [12]. As can be seen, the Γ values obtained by DPSC correlate very well with the results by CV at the same concentration of FcCH$_2$OH in solution.

The empirical isotherms were fitted to the Sips model given by equation 5:

$$\Gamma = \frac{\Gamma_{max} K_e c_0^h}{1 + K_e c_0^h} \quad (5)$$

where Γ_{max} is the maximum surface coverage, K_e is the Sips's equilibrium constant, c_0 is the bulk concentration and h is a term that is related with surface heterogeneity and increases with surface roughness. If h = 1, the model turns into a Langmuir isotherm [26]. Figure 5.4b illustrates the good agreement between the Sips model and the experimental surface coverage of $FcCH_2OH$ on GC and GCE/CNO surfaces. Further, the residual plots (data not shown) showed randomly dispersed points around the x axis indicating that the model was appropriated to explain the experimental data. The values of Γ_{max}, K_e and h for the adsorption of $FcCH_2OH$ on GCE/CNO and GCE surfaces obtained from the fitting of equation 5 with the experimental data are presented in Table 5.1. On GCE/CNO electrodes, the h value (2.1) is almost twice as compared with GCE (h = 1.2) and suggests that adsorption of the redox species on a rough surface can create higher current densities as compared with GCE. Additionally, the K_e value for GCE/CNO was almost twice as greater than for GCE, indicating a favoured adsorption of $FcCH_2OH$. These results are in correspondence with those obtained by cyclic voltammetry.

Table 5.1. Parameters for the Sips equation obtained from the fitting of the data of $FcCH_2OH$ adsorption on GCE/CNO and GCE surfaces.

	Γ_{max} (mol cm^{-2})	**K_e (L mol^{-1})**	**h**
GCE	7.5×10^{-10}	23	1.2
GCE/CNO	8.8×10^{-9}	44	2.1

The interfacial parameters of $FcCH_2OH$ on the CNO surface can be explained considering the occurrence of π-π and CH-π interactions between the cyclopentadienyl rings and the fullerenic structure of CNOs. It is also possible that intermolecular CH-π and H-bonding interactions between the adsorbed $FcCH_2OH$ molecules and polar groups on the surface play an important role (Scheme 5.1) [27,28]. In fact, X-ray photoelectron spectroscopy analysis indicate that the CNO layer has an oxygen content of 2.86% in the form of hydroxyl and carboxylic functional groups (see Chapter 3) which might favour H-bonding interactions with $FcCH_2OH$ molecules similar to what has been observed for $FcCH_2OH$ adsorbed on 3-mercaptopropanoic acid self-assembled monolayers [29,30]. In addition, the surface roughness estimated by the root mean square height deviation (R_q) [31] has a value of 18.6 for GCE/CNO and 6.9 for GCE. Therefore, the intermolecular interactions can also be favoured by the roughness of the surface that allows multiple orientations of the $FcCH_2OH$ molecules (Scheme 5.1). In the case of GC, the absorption of $FcCH_2OH$ is considerably lower due to the absence of aromatic structure and polar functional groups and its low roughness as compared to GCE/CNO.

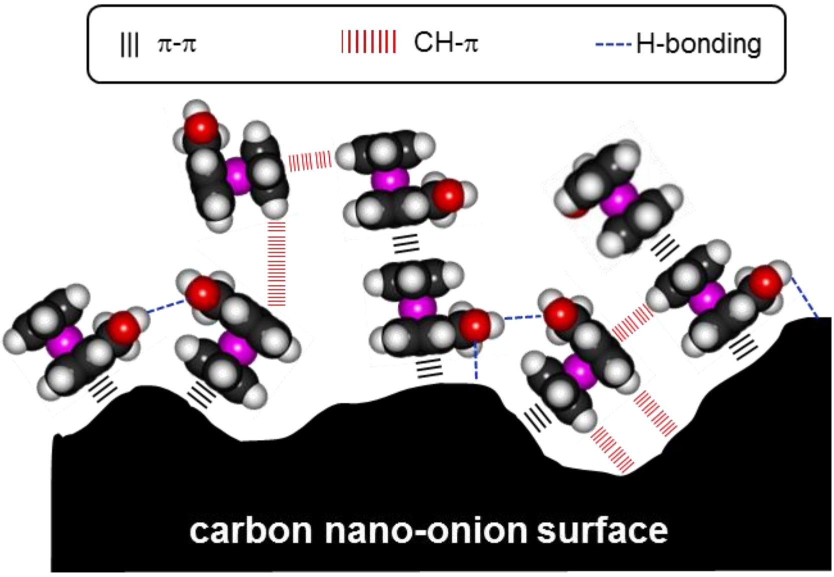

Scheme 5.1. Possible modes of interaction of $FcCH_2OH$ with the GCE/CNO surface.

5.4. Conclusions

In conclusion, in this Chapter, we demonstrated the distinct electrochemical behaviour of $[Fe(CN)_6]^{3-}$ and $FcCH_2OH$ redox probes at glassy carbon electrodes modified with CNOs. Cyclic voltammetry analysis indicated a weak adsorption of the reduced form of $FcCH_2OH$ takes place on the GCE/CNO electrodes and at higher extension than on bare GCE. The surface coverage of $FcCH_2OH$ on GCE/CNO was found to be 4.3×10^{-9} mol cm^{-2} indicating the formation of a multilayered arrangement and was 14-times greater than on GCE. The positive Laviron's lateral interaction parameters ($vG\theta_T = 0.21$) and high heterogeneity factor according to the Sips model (h = 2.1) are indicative of the adsorption of $FcCH_2OH$ on a rough surface, which was explained considering π-π and perpendicular CH-π interactions between the cyclopentadienyl rings and the fullerenic structure of CNOs and hydrogen bonding interactions between the oxygen containing groups of CNOs and $FcCH_2OH$. Our results highlight the importance of considering the adsorption of the redox species to interpret the physical and kinetic parameters of these systems. They could also help to explain the signal enhancements observed in electrochemical CNO-based (bio)analytical systems. This enhancement has been associated with the increase in surface area, semi-metal properties and the presence of structural defects on the CNOs that enhance electron transfer process without accounting the adsorption of the redox organic labels.

References

[1] R.L. McCreery, *Advanced carbon electrode materials for molecular electrochemistry*, Chem. Rev. 108 (2008) 2646–2687.

[2] P.R. Unwin, A.G. Güell, G. Zhang, *Nanoscale electrochemistry of sp^2 carbon materials: from graphite and graphene to carbon nanotubes*, Acc. Chem. Res. 49 (2016) 2041–2048.

[3] D. Tománek, Guide through the nanocarbon jungle, 1st ed., Morgan & Claypool, San Rafael, CA, 2014.

[4] T. Laurila, S. Sainio, M. Caro, *Hybrid carbon based nanomaterials for electrochemical detection of biomolecules*, Prog. Mater. Sci. 88 (2017) 499–594.

[5] K. Chatterjee, M. Ashokkumar, H. Gullapalli, Y. Gong, R. Vajtai, P. Thanikaivelan, P.M. Ajayan, *Nitrogen-rich carbon nano-onions for oxygen reduction reaction*, Carbon. 130 (2018) 645–651.

[6] O. Mykhailiv, H. Zubyk, K. Brzezinski, M. Gras, G. Lota, M. Gniadek, E. Romero, L. Echegoyen, M.E. Plonska-Brzezinska, *Improvement of the structural and chemical properties of carbon nano-onions for electrocatalysis*, ChemNanoMat. 3 (2017) 583–590.

[7] F.D. Han, B. Yao, Y.J. Bai, *Preparation of carbon nano-onions and their application as anode materials for rechargeable lithium-ion batteries*, J. Phys. Chem. C. 115

(2011) 8923–8927.
[8] M.E. Plonska-Brzezinska, L. Echegoyen, *Carbon nano-onions for supercapacitor electrodes: Recent developments and applications*, J. Mater. Chem. A. 1 (2013) 13703–13714.
[9] J.K. McDonough, A.I. Frolov, V. Presser, J. Niu, C.H. Miller, T. Ubieto, M. V. Fedorov, Y. Gogotsi, *Influence of the structure of carbon onions on their electrochemical performance in supercapacitor electrodes*, Carbon. 50 (2012) 3298–3309.
[10] J.P. Bartolome, L. Echegoyen, A. Fragoso, *Reactive carbon nano-onion modified glassy carbon surfaces as DNA sensors for human papillomavirus oncogene detection with enhanced sensitivity*, Anal. Chem. 87 (2015) 6744–6751.
[11] J.C. Zuaznabar-Gardona, A. Fragoso, *Development of highly sensitive IgA immunosensors based on co-electropolymerized L-DOPA/dopamine carbon nano-onion modified electrodes*, Biosens. Bioelectron. 141 (2019) 111357.
[12] A.S. Cuharuc, G. Zhang, P.R. Unwin, *Electrochemistry of ferrocene derivatives on highly oriented pyrolytic graphite (HOPG): quantification and impacts of surface adsorption*, Phys. Chem. Chem. Phys. 18 (2016) 4966–4977.
[13] A. Chaubey, B.D. Malhotra, *Mediated biosensors*, Biosens. Bioelectron. 17 (2002) 441–456.
[14] J. Velmurugan, P. Sun, M. V. Mirkin, *Scanning electrochemical microscopy with gold nanotips: the effect of electrode material on electron transfer rates*, J. Phys. Chem. C. 113 (2009) 459–464.
[15] A.M. Bond, E.A. McLennan, R.S. Stojanovic, F.G. Thomas, *Assessment of conditions under which the oxidation of ferrocene can be used as a standard voltammetric reference process in aqueous media*, Anal. Chem. 59 (1987) 2853–2860.
[16] D. Zheng, H. Li, B. Lu, Z. Xu, H. Chen, *Electrochemical properties of ferrocene adsorbed on multi-walled carbon nanotubes electrode*, Thin Solid Films. 516 (2008) 2151–2157.
[17] W. Li, C. Tan, M.A. Lowe, H.D. Abruña, D.C. Ralph, *Electrochemistry of individual monolayer graphene sheets*, ACS Nano. 5 (2011) 2264–2270.
[18] Q. Zheng, H. Shao, *Correlation between redox species adsorption and electron transfer kinetics of mildly oxidized graphene: A chronocoulometry and SECM study*,

Electrochem. Commun. 103 (2019) 83–87.

[19] R.H. Wopschall, I. Shain, *Effects of adsorption of electroactive species in stationary electrode polarography*, Anal. Chem. 39 (1967) 1514–1527.

[20] J.P. Bartolome, A. Fragoso, *Preparation and characterization of carbon nano-onions by nanodiamond annealing and functionalization by radio-frequency Ar/O_2 plasma*, Fullerenes, Nanotub. Carbon Nanostructures. 25 (2017) 327–334.

[21] K. Shinozaki, J.W. Zack, S. Pylypenko, B.S. Pivovar, S.S. Kocha, *Oxygen reduction reaction measurements on platinum electrocatalysts utilizing rotating disk electrode technique*, J. Electrochem. Soc. 162 (2015) F1384–F1396.

[22] G. Gasser, A.J. Fischmann, C.M. Forsyth, L. Spiccia, *Products of hydrolysis of (ferrocenylmethyl)trimethylammonium iodide: Synthesis of hydroxymethylferrocene and bis(ferrocenylmethyl) ether*, J. Organomet. Chem. 692 (2007) 3835–3840.

[23] J.P. Bartolome, A. Fragoso, *Electrochemical detection of nitrite and ascorbic acid at glassy carbon electrodes modified with carbon nano-onions bearing electroactive moieties*, Inorganica Chim. Acta. 468 (2017) 223–231.

[24] E. Laviron, *Surface linear potential sweep voltammetry: Equation of the peaks for a reversible reaction when interactions between the adsorbed molecules are taken into account*, J. Electroanal. Chem. Interfacial Electrochem. 52 (1974) 395–402.

[25] F.C. Anson, *Innovations in the study of adsorbed reactants by chronocoulometry*, Anal. Chem. 38 (1966) 54–57.

[26] D.D. Do, Adsorption analysis: equilibria and kinetics, Imperial College Press, 1998.

[27] N.A. Wasio, R.C. Quardokus, R.P. Forrest, C.S. Lent, S.A. Corcelli, J.A. Christie, K.W. Henderson, S.A. Kandel, *Self-assembly of hydrogen-bonded two-dimensional quasicrystals*, Nature. 507 (2014) 86–89.

[28] D. Zhong, K. Wedeking, T. Blömker, G. Erker, H. Fuchs, L. Chi, *Multilevel supramolecular architectures self-assembled on metal surfaces*, ACS Nano. 4 (2010) 1997–2002.

[29] Q. Zheng, X. Huang, Y. Liu, X. Fang, J. Zhang, H. Shao, *Electrochemical quantification of intermolecular hydrogen bonding between ferrocenemethanol and 3-*

mercaptopropanoic acid on gold, J. Phys. Chem. C. 121 (2017) 22123–22129.

[30] X. Huang, J. Chen, X. Fang, C. Yan, H. Shao, *Exploring the enhancement of electron tunneling induced by intermolecular interactions on surface of self-assembled monolayer*, J. Electroanal. Chem. 837 (2019) 143–150.

[31] G. Chinga, P. Johnsen, R. Dougherty, E.L. Berli, J. Walter, *Quantification of the 3D microstructure of SC surfaces*, J. Microsc. 227 (2007) 254–265.

Chapter 6

Electrocatalytic properties of thin films of pristine and oxidized carbon nano-onions[5]

6.1. Introduction

Carbon materials (CMs) are promising candidates for many (electro)catalytic applications [1,2]. Their structural and surface functional group diversity result in excellent catalytic activities as compared to some industrial transition-metal based catalysts [3]. Additionally, CMs are more abundant, have low cost, and present relatively high chemical stability and tunable properties [4]. Thus, for the seek of sustainability in energy conversion systems and chemical industry, CMs are intensely studied to replace transition-metal based catalysts.

Like other CMs, CNOs are also competitive candidates as metal-free (electro)catalysts for different chemical and technological process. For example, CNOs have been applied as catalyst to the ethylbenzene dehydrogenation and phenolic oxidation, showing better catalytic performance than other CMs [5,6]. Nitrogen and boron doped CNOs have been used as electrocatalyst for the oxygen reduction reaction which is a very important reaction in fuel cell technologies [7,8]. More recently, CNOs modified with nitrogen and sulfur demonstrated enhanced enzymatic-like electrocatalytic activity toward hydrogen peroxide compared to the activity of pristine CNOs

---

[5] *This Chapter is part of a published work in J.C. Zuaznabar-Gardona, A. Fragoso, Electrochimica Acta, 353 (2020) 136495.*

[9]. On the other hand, the electrocatalytic properties of CNOs have been explored to the simultaneous detection of dopamine, uric acid [10] and nitrite ions [11] in presence of ascorbic acid. Despite these achievements, the origin of the catalytic behavior of CNOs remain elusive and controversial [3]. Thus, new studies to address in more details the structure-properties relationship of these materials are required.

In this Chapter, we studied the electrocatalytic properties for the reduction of O_2 to H_2O_2 and the oxidation of H_2O_2, ascorbic acid (AA), dopamine (DA) and uric acid (UA) at CNO, CNO-RF and CNO-OXI modified electrodes. We compared the resulting electrocatalytic properties of these surfaces and correlated them with their surface chemistry.

6.2. Materials and methods

H_2O_2 (30%), NaH_2PO_4, $HClO_4$ (60%), nitric acid, sulfuric acid, KCl, dimethylformamide (DMF), dopamine hydrochloride, uric acid sodium salt and sodium ascorbate were purchased from Sigma-Aldrich (Spain), and were used as received. All solutions were prepared with double distilled water (18.2 MΩ cm) obtained from a Milli-Q® system (Millipore, Madrid, Spain). CNOs were prepared by thermal annealing of nanodiamonds and further oxidized by radio frequency Ar/O_2 plasma, and chemically oxidized as previously reported [12,13].

All electrochemical measurements were obtained using a PC-controlled CHI 660A electrochemical workstation (CH Instruments, Austin, USA) with a three-electrode cell configuration. A platinum wire was used as counter electrode and a commercial Ag/AgCl (sat) electrode serves as reference electrode. Glassy carbon electrodes (CH Instruments model CHI104, 3.0 mm diameter, 0.07 cm^2 geometric area) coated with pristine CNO, radio frequency Ar/O_2 plasma oxidized CNO (CNO-RF) or chemically oxidized CNO (CNO-OXI) films were used as working electrodes.

6.2.1. Electrode preparation

Prior to modification, bare GC electrodes (GCE) were first manually smoothed with emery paper # 600 followed by polishing to a mirror finish with 0.3 μm alumina slurries. The polished GCE were sonicated in Milli-Q® water for 5 min and dried under a stream of nitrogen. GCE were modified by drop-casting a homogeneous dispersion of CNO, CNO-RF or CNO-OXI in DMF (4 mg mL^{-1}) prepared using an ultrasonic-bath for 30 minutes. To obtain a thin layer of CNO, CNO-RF or CNO-OXI, 1 μL of the dispersion was cast twice on the surface of the electrodes and dried in an oven at 80ºC under DMF atmosphere for 30 minutes. This procedure was used to avoid the formation of the so called coffee-ring effect which results in non-homogeneous films [14].

6.2.2. Oxygen reduction at CNO, CNO-RF and CNO-OXI modified electrodes

Linear sweep voltammetry (LSV) was used to study the oxygen reduction reaction (ORR) at the CNO, CNO-RF and CNO-OXI modified electrodes in $HClO_4$ (0.1 mol L^{-1}) as supporting electrolyte. The potential was scanned from 0.6 V to -1 V at 10 mV s^{-1}. The

$HClO_4$ solution was saturated with N_2, air and pure O_2 for background and faradaic measurements, respectively.

6.2.3. Amperometric detection of hydrogen peroxide at CNO, CNO-RF and CNO-OXI modified electrodes

The determination of H_2O_2 was performed in 15 mL phosphate buffer (PB) (0.1 mol L^{-1}, pH 7) with constant stirring at a potential of 0.7 V and 25 °C. After the current reached steady state, increasing amounts of H_2O_2 were added to PB every 1 minute. The current vs c(H_2O_2) calibration curves were constructed from triplicate measurements.

6.2.4. Electrocatalytic oxidation of ascorbic acid, dopamine and uric acid at GC surfaces modified with CNO, CNO-RF and CNO-OXI

The electrocatalytic oxidation of ascorbic acid, dopamine and uric acid was assessed by CV and differential pulse voltammetry (DPV) in the potential range between −0.2 V to 0.6 V in 0.1 mol L^{-1} PB pH 7. CV were performed at 50 mV s^{-1}. DPV parameters were set as follows: increment potential of each pulse= 0.005 V, amplitude= 0.05 V, pulse width= 0.05 s, sample width = 0.025 s and pulse period = 0.2 s. The calibration plots were constructed from the DPV peak responses at -0.05, 0.15 and 0.28 V for AA, DA and UA, respectively at increasing concentrations of the three analytes.

6.3. Results and discussion

6.3.1. Oxygen reduction reaction at GC surfaces modified with CNO, CNO-RF and CNO-OXI

Oxygen reduction reaction (ORR) is an important reaction involved in many (bio)electrocatalytic processes and proton-exchange-membrane fuel cells. Although platinum-based catalysts are used to improve the kinetics of ORR, the high cost, low stability, CO poisoning and scarcity of platinum limit the practical and commercial applications of these catalysts. Alternatively, carbon-based materials are interesting alternatives because of their abundance, low cost, chemical stability and tunable properties which in turns can greatly reduce the cost and increase the efficiency of energy storage devices like fuel cells [4]. Thus, we examined the electrocatalytic activity of CNO, CNO-RF and CNO-OXI for ORR in acidic media. Linear sweep voltammograms (LSVs) at 10 mV s^{-1} in N_2 and O_2 saturated 0.1 mol L^{-1} $HClO_4$ solutions were recorded at unmodified and CNO, CNO-RF, CNO-OXI modified GC electrodes. Figure 6.1a summarizes the results acquired in O_2 saturated 0.1 mol L^{-1} $HClO_4$. Experiments in N_2 saturated solutions gave no response except for the breakdown of solvent (see inset of Figure 6.1a). GCE and GCE/CNO electrodes showed little responses for ORR at -0.48 and -0.40 V, respectively, which occurred very close to the breakdown of solvent at -0.60 V. In contrast, GCE/CNO-RF and GCE/CNO-OXI electrodes presented a defined peak at -0.38 and -0.16 V, respectively, corresponding to the reaction:

$$O_2 + 2H^+ + 2\bar{e} \rightarrow H_2O_2$$

This represents a 0.10 and 0.32 V decrease in the ORR overpotential with respect to the GCE surface, which indicates a better electrocatalytic activity of these surfaces.

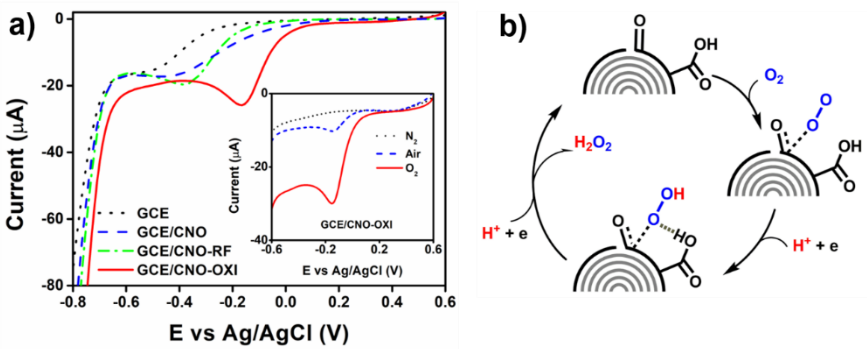

Figure 6.1. a) Linear sweep voltammograms (LSVs) of O_2 saturated 0.1 mol L^{-1} $HClO_4$ solution at CNO, CNO-RF and CNO-OXI modified GC electrodes. The potential was swept from 0.6 to -0.8 V at 10 mV s^{-1}. Inset: LSVs at GCE/CNO-OXI electrode recorded in N_2, air and O_2 saturated $HClO_4$. b) Schematic representation of the steps involved on the oxygen reduction at GCE/CNO-OXI electrodes.

From Figure 6.1a, it could be inferred that the oxidation of CNO facilitates the reduction of O_2 to H_2O_2 in acid media. It has been demonstrated that the presence of oxygen containing groups on carbon materials favor their electrocatalytic activity for ORR in acidic media [15–17]. Carbonyl groups favor O_2 adsorption on the carbon catalyst surface because of the electrophilic character of their carbonyl carbon atoms resulting in the formation of $C_{surface}$-OOH adducts. Carboxylic groups form hydrogen bonds with the oxygen atoms that are directly bound to the catalyst surface which in turn weakens the $C_{surface}$-OOH bonds (Figure 6.1b). As a result, O_2 reduction goes through a two-electron pathway with the formation of H_2O_2 rather that the four-electron pathway leading to reduction to water [18].

The reduction of O_2 at GCE/CNO-OXI occurred at a more positive potential (-0.16 V), than at other carbon materials such as MWCNT (-0.35 V), CNO polymeric composites (-0.30 V), graphene nanoflakes (-0.40 V) and pyrolytic graphite (-0.40 V) [19,20]. These results suggest that oxidized CNO might have great promise as metal-free electrocatalyst for the electrogeneration of H_2O_2 at low potentials as well as for O_2 sensing [21,22].

6.3.2. Electrochemical detection of H_2O_2 at GC surfaces modified with CNO, CNO-RF and CNO-OXI

H_2O_2 is widely used in pharmaceutical, environmental, industrial and academic research. In the field of enzymatic biosensors, the detection of H_2O_2 is very important since it is the by-product of reactions catalyzed by oxidase enzymes.

GC electrodes modified with CNO, CNO-RF and CNO-OXI were tested as new platform to detect H_2O_2 in solution. The electrochemical oxidation of H_2O_2 at bare and modified electrodes was investigated by cyclic voltammetry and chronoamperometry. Figure 6.2a shows cyclic voltammograms recorded in 1.2 mmol L^{-1} H_2O_2 in 0.1 mol L^{-1} PB pH 7 at GC, GCE/CNO, GCE/CNO-RF and GCE/CNO-OXI electrodes. In all modified electrodes, the oxidation current at about 0.7 V was higher than at bare GCE. In the case of GCE/CNO-OXI, a clear anodic peak at 0.58 V was observed. The lower oxidation potential of H_2O_2 at GCE/CNO-OXI indicates an electrocatalytic effect of CNO-OXI toward oxidation of H_2O_2. It has been demonstrated that increasing the amount of oxygen functional groups on carbon materials, in particular carboxylic acid moieties, leads to an improved analytical performance toward the electrochemical oxidation of H_2O_2 [23]. Additionally, the adsorption of H_2O_2 on the electrode surface also influences its electrochemical oxidation [24]. This was corroborated by further experiments where carboxylic moieties were modified with ethanolamine and Methylene Blue was adsorbed on the surface of GCE/CNO-OXI electrodes. Each modification resulted in a reduction of about 40% the sensitivity toward H_2O_2.

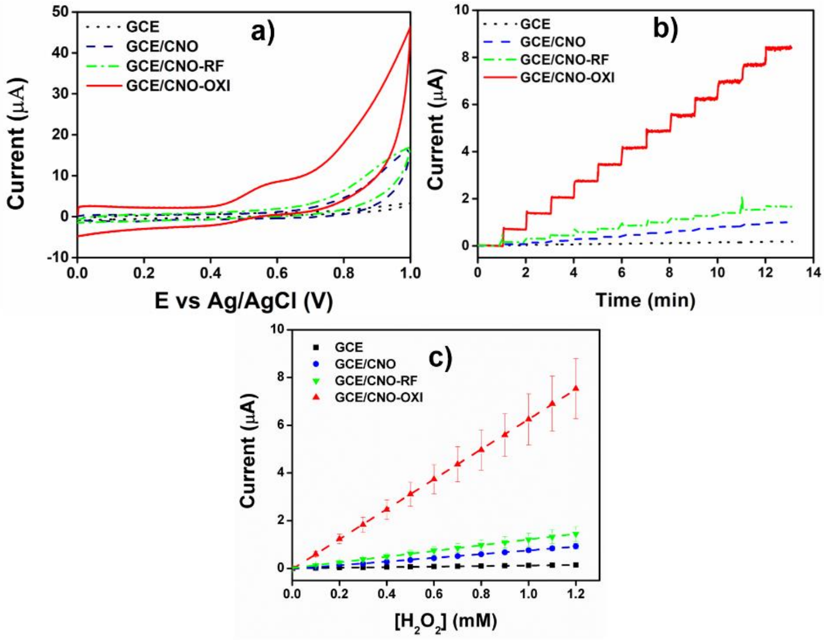

Figure 6.2. a) CVs of 1.2 mmol L^{-1} H_2O_2 using unmodified and CNO, CNO-RF, CNO-OXI modified GC electrodes at 10 mV s^{-1}. b) Chronoamperometric response at 0.7 V (vs. Ag/AgCl) to consecutive H_2O_2 additions under steady-state conditions using the indicated electrodes. c) Calibration plot obtained from the chronoamperometric experiments. Measurements were taken in 0.1 mol L^{-1} PB pH 7.

The analytical performance of CNO modified electrodes to detect H_2O_2 was further studied by chronoamperometry. Figure 6.2b shows the current responses at 0.7 V of unmodified and CNO, CNO-RF, CNO-OXI modified GC electrodes toward different H_2O_2 additions. All modified electrodes presented an enhanced electrochemical response compared to the unmodified GCE. The analytical sensitivity (taken as the slope of the calibration curve shown in Figure 6.2c) increased from 20.4 ± 0.3 μA μmol^{-1} L cm^{-2} at GCE to 120 ± 1 μA μmol^{-1} L cm^{-2} at GCE/CNO. Further sensitivity enhancement was achieved by using GCE/CNO-RF (197 ± 1 μA μmol^{-1} L cm^{-2}) to reach a value of 1000 ± 3 μA μmol^{-1} L cm^{-2} at GCE/CNO-OXI. This means that the modification of GCE with CNO-OXI led to a 50-fold signal enhancement toward H_2O_2. These sensitivity values are considerably higher than those recently reported for H_2O_2 detection using activated screen-printed electrodes [23].

6.3.3. Electrocatalytic oxidation of ascorbic acid, dopamine and uric acid at GC surfaces modified with CNO, CNO-RF and CNO-OXI

Ascorbic acid (AA), dopamine (DA) and uric acid (UA) are biomolecules that undergo two-proton/two-electron oxidation reactions that take place at almost the same potential at the surface of conventional electrodes. The individual resolution of these redox processes is frequently used to assess the electroactivity and quality of carbon-based electrodes. Thus, we also investigated for the first time the electrocatalytic oxidation of AA, DA and UA at CNO, CNO-RF and CNO-OX modified electrodes.

Figure 6.3 shows CVs and DPVs for the oxidation of AA, DA and UA in 0.1 mol L^{-1} PB pH 7 containing 0.5 mmol L^{-1} AA, 0.1 mmol L^{-1} DA and 0.2 mmol L^{-1} UA at bare and CNO modified electrodes.

Overall, the anodic peak currents obtained at GCE/CNO, GCE/CNO-RF and GCE/CNO-OXI were higher than those at bare GCE, indicating a better electrocatalytic activity toward these molecules. The best resolved response for AA, DA and UA was obtained at GCE/CNO electrodes in comparison with the other tested electrodes. The peak separations of AA-DA and DA-UA were 200 mV and 133 mV, respectively. The electrooxidation of AA, DA and UA at GCE/CNO electrodes occurs at ~0.0, 0.20 and 0.33 V vs Ag/AgCl, respectively. These values are shifted to lower potentials than the obtained using other modification strategies[25,26]. In the case of DA, the anodic and cathodic peak separation was reduced in 10 mV, indicating an enhanced electron transfer at CNO modified GC electrodes. On the other hand, the peaks obtained at GCE/CNO-OXI electrodes presented certain degree of overlapping which hinders the resolution of the individual redox process of AA, DA and UA.

The differences in the electrochemical activity of DA, UA and AA over the CNO electrode surfaces can be explained by the modes of molecular interaction of the analytes and the electrode surface. AA molecules interact through H-bond formation with the oxygenated groups presented in the CNO and CNO-RF [12]. These functional groups make feasible the electron transfer process [25]. Thus, the AA oxidation is observable and occurs at lower potential than at GC electrodes. For DA and UA π–π interactions with the sp^2 network of CNO are also possible [27]. Thus, the availability of DA and UA near or on the electrode surface is increased and the peak currents also increase. However, the peak position was similar than that at GC electrodes, indicating that the electron transfer was not altered.

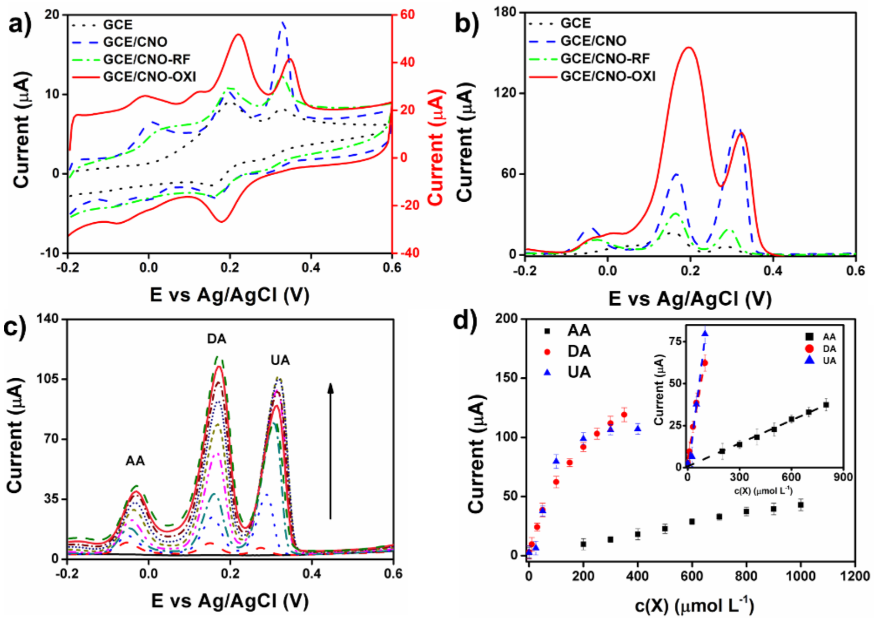

Figure 6.3. a) CVs and b) DPV responses at GCE, GCE/CNO, GCE/CNO-RF and GCE/CNO-OXI electrodes in 0.1 mol L^{-1} phosphate buffer pH 7 containing 0.5 mmol L^{-1} AA, 0.1 mmol L^{-1} DA and 0.2 mmol L^{-1} UA. c) DPV response at GCE/CNO electrodes to simultaneous addition of AA, DA and UA in 0.1 mol L^{-1} phosphate buffer pH 7. d) Corresponding calibration plots with increasing AA, DA and UA concentration. Inset: linear relationship between the oxidation peak current and the concentration of AA, DA and UA obtained from curve d).

At the GCE/CNO-OXI surface, DA molecules can experience electrostatic attraction with the carboxylate ions anchored on the electrode surface since the amine group of DA (pK_a = 10.5) is positively charged at pH 7 [28]. Thus, the amount of DA on the electrode surface is increased. As a result, the peak current for the oxidation of DA enhances ~10 , 5- and 2.5-times respect to GCE, GCE/CNO-RF and GCE/CNO electrodes, respectively. The overlapping of the DA and UA oxidation peaks is an undesirable side-effect of the increment of the number of DA molecules on the GCE/CNO-OXI electrode surface. The closer the DA molecules are, the higher repulsive intermolecular interactions, and then, a broader peak is observed [26]. As a result, the individual redox process of DA and UA are not well-resolved at the GCE/CNO-OXI electrode surface.

It is known that AA, DA and UA are important molecules in neurochemistry and , pharmaceutical and food industry. Thus, we explore the possibility to detect simultaneously AA, DA and UA using the GCE/CNO electrode, in which the best separation between the individual redox processes of AA, DA and UA is observed. Since the DPV method exhibits a much higher current sensitivity and better resolution than cyclic voltammetry, it was used in the determination of the three analytes [29]. As shown in the Figure 6.3c, on successive addition of AA, DA and UA, the corresponding oxidation peaks remained well resolved and the peak currents increased with an increase in the concentration of the three molecules. The proportionality of the peak current with respect to the concentration in simultaneous addition of AA, DA and UA are shown in Figure 6.3d. Electrochemical signals were tolerated with each other up to 800 µmol L^{-1} AA , 100 µmol L^{-1} DA and 100 µmol L^{-1} UA. After this concentration the peak current response became nonlinear due to the saturation of the electrode surface.

The linear calibration plot for AA, DA and UA are presented in the inset of Figure 6.3d. The calibration plots followed the regression equations j_{AA} (mA cm^{-2}) = $0.00175c_{AA}$ (µmol L^{-1}) + 0.027, j_{DA} (mA cm^{-2}) = $0.0228c_{DA}$ (µmol L^{-1}) + 0.21, and j_{UA} (mA cm^{-2}) = $0.0318c_{UA}$ (µmol L^{-1}) − 0.15. The limit of detection (LOD) and limit of quantification (LOQ) were calculated as 3.3×σ/S and 10×σ/S, where σ is the standard deviation in the blank signal and S the sensitivity [30]. Based on this method the theoretical LOD are 1.81, 0.45, 0.32 μmol L^{-1} and LOQ were 5.50, 1.37, 0.96 μmol L^{-1} for AA, DA and UA, respectively. The comparison of the analytical performance at the GCE/CNO electrodes with other reported systems is summarized in Table 6.1. It can be seen that the GCE/CNO electrodes possess improved or comparable analytical performance that other more complex systems. Furthermore, since the physiological range for AA, DA and UA are 28-85 [31], 0.05-0.7 [30], and 240-520 μmol L^{-1} [32] , respectively, the proposed system might be applied to the individual or simultaneous determination of these three analytes in biological samples or other matrixes with high sensitivity and selectivity.

Table 6.1. Comparison of analytical performances of different electrochemical sensors based on carbon nanomaterials for the simultaneous determination of AA, DA and UA.

Electrode	**LDR (*μ*mol L^{-1})**			**LOD (*μ*mol L^{-1})**			**Det**		**Ref.**
	AA	**DA**	**UA**	**AA**	**DA**	**UA**	**B**	**P**	
Pd/CNF	50–4000	0.5–160	2–200	15	0.2	0.7	+	+	[33]
MWCNTs/PEDOT	100–2000	10–330	10–250	100	10	10	-	-	[34]
CCE/MWCNTs	15.0–800	0.50–100	0.55–90	7.7	0.31	0.4	+	+	[35]
GCE/MWCNTs/Fe(III)P	14–2500	0.7–3600	5.8–1300	3.0	0.09	0.3	+	-	[36]
GCE/SWNCTs/PPyox	20–1000	1–50	2–100	4.6	0.38	0.7	-	-	[37]
GCE/SWNCTs/CPB	-	4–1200	2–90	-	0.6	7.0	-	+	[38]

Table 6.1. Comparison of analytical performances of different electrochemical sensors based on carbon nanomaterials for the simultaneous determination of AA, DA and UA (*Continuation*).

Electrode	**LDR (μmol L^{-1})**			**LOD (μmol L^{-1})**			**Det**		**Ref.**
	AA	**DA**	**UA**	**AA**	**DA**	**UA**	**B**	**P**	
GCE/ImAS/erGO	30–2000	0.1–200	20-490	10	0.03	5.0	+	-	[39]
GCE/NG	5–1300	0.5–170	0.1–20	2.2	0.25	-	-	-	[40]
GCE/CNO/PDDA	500–3000	100–4000	500–3000	-	1.0	-	-	+	[41]
GCE/CNO	0–800	0–100	0–100	1.8	0.4	0.3	-	-	**This work**

LDR: linear detection range, LOD: limit of detection, Det: determination B: body fluids, P: pharmaceutical samples, Pd: palladium nanoparticle, CNF: carbon nanofibers, MWCNTs: multiwalled carbon nanotube, PEDOT: poly(3,4-ethylendioxythiophene), CCE: carbon-ceramic electrode, Fe(III)P: chloro[3,7,12,17-tetramethyl-8,13-divinylporphyrin-2,18-dipropanoato (2−)]iron(III), SWNTs: single-walled carbon nanotubes, PPyox: overoxidized polypyrrole, CPB: cetylpyridinium bromide, ImAS: imidazolium alkoxysilane, erGO: electrochemically reduced graphene oxide, NG: nitrogen doped graphene, CNO: carbon nano-onions, PDDA: poly(diallyldimethylammonium chloride).

6.4. Conclusions

In summary, we investigated and compared the electrochemical properties of pristine CNO, radio frequency Ar/O_2 plasma oxidized CNO (CNO-RF) and chemically oxidized CNO (CNO-OXI) deposited on glassy carbon electrodes (GCE). The electrocatalytic response for the reduction of O_2 to H_2O_2 was improved by increasing the amount of oxygenated species on the surface of CNO. In the same way, the sensitivity for the electrochemical detection of H_2O_2 was enhanced up to 50-fold respect to unmodified GC electrode by chemical oxidation of CNO. These results suggest that oxidized CNO might have great promise as metal-free electrocatalyst for different reactions. Simultaneous detection of ascorbic acid, dopamine and uric acid was performed by differential pulse voltammetry at CNO, CNO-RF and CNO-OXI modified electrodes. The best analytical performance in terms of sensitivity and peak separation was achieved by using GCE/CNO electrodes. Moreover, the GCE/CNO electrodes possess improved or comparable analytical performance that other more complex systems used to detect these three analytes. The electrochemical data obtained here can serve as an all-important benchmark for CNO modified electrode performance. These results demonstrated that CNO are very promising materials for the electrochemical detection of different redox analytes.

References

[1] D.S. Su, S. Perathoner, G. Centi, *Nanocarbons for the development of advanced catalysts*, Chem. Rev. 113 (2013) 5782–5816.

[2] H. Jin, C. Guo, X. Liu, J. Liu, A. Vasileff, Y. Jiao, Y. Zheng, S.Z. Qiao, *Emerging two-dimensional nanomaterials for electrocatalysis*, Chem. Rev. 118 (2018) 6337–6408.

[3] Y. Lin, Z. Feng, L. Yu, Q. Gu, S. Wu, D.S. Su, *Insights into the surface chemistry and electronic properties of sp^2 and sp^3 -hybridized nanocarbon materials for catalysis*, Chem. Commun. 53 (2017) 4834–4837.

[4] M. Zhang, L. Dai, *Carbon nanomaterials as metal-free catalysts in next generation fuel cells*, Nano Energy. 1 (2012) 514–517.

[5] J. Zhang, D.S. Su, R. Blume, R. Schlögl, R. Wang, X. Yang, A. Gajović, *Surface chemistry and catalytic reactivity of a nanodiamond in the steam-free dehydrogenation of ethylbenzene*, Angew. Chemie - Int. Ed. 49 (2010) 8640–8644.

[6] Y. Lin, B. Li, Z. Feng, Y.A. Kim, M. Endo, D.S. Su, *Efficient metal-free catalytic reaction pathway for selective oxidation of substituted phenols*, ACS Catal. 5 (2015) 5921–5926.

[7] K. Chatterjee, M. Ashokkumar, H. Gullapalli, Y. Gong, R. Vajtai, P. Thanikaivelan, P.M. Ajayan, *Nitrogen-rich carbon*

nano-onions for oxygen reduction reaction, Carbon. 130 (2018) 645–651.

[8] Y. Lin, Y. Zhu, B. Zhang, Y.A. Kim, M. Endo, D.S. Su, *Boron-doped onion-like carbon with enriched substitutional boron: The relationship between electronic properties and catalytic performance*, J. Mater. Chem. A. 3 (2015) 21805–21814.

[9] O. Butsyk, P. Olejnik, E. Romero, M.E. Plonska-Brzezinska, *Postsynthetic treatment of carbon nano-onions: Surface modification by heteroatoms to enhance their capacitive and electrocatalytic properties*, Carbon. 147 (2019) 90–104.

[10] M.K. Dey, A.K. Satpati, *Functionalised carbon nano spheres modified electrode for simultaneous determination of dopamine and uric acid*, J. Electroanal. Chem. 787 (2017) 95–102.

[11] J.P. Bartolome, A. Fragoso, *Electrochemical detection of nitrite and ascorbic acid at glassy carbon electrodes modified with carbon nano-onions bearing electroactive moieties*, Inorganica Chim. Acta. 468 (2017) 223–231.

[12] J.P. Bartolome, A. Fragoso, *Preparation and characterization of carbon nano-onions by nanodiamond annealing and functionalization by radio-frequency Ar/O_2 plasma*, Fullerenes, Nanotub. Carbon Nanostructures. 25 (2017) 327–334.

[13] E. Wajs, A. Molina-Ontoria, T.T. Nielsen, L. Echegoyen, A. Fragoso, *Supramolecular solubilization of cyclodextrin-modified carbon nano-onions by host–guest interactions*, Langmuir. 31 (2015) 535–541.

[14] K. Shinozaki, J.W. Zack, S. Pylypenko, B.S. Pivovar, S.S. Kocha, *Oxygen reduction reaction measurements on platinum electrocatalysts utilizing rotating disk electrode technique*, J. Electrochem. Soc. 162 (2015) F1384–F1396.

[15] K. Matsubara, K. Waki, *The effect of O-functionalities for the electrochemical reduction of oxygen on MWCNTs in acid media*, Electrochem. Solid-State Lett. 13 (2010) F7.

[16] H.-J. Zhang, H. Li, X. Li, B. Zhao, J. Yang, *Electrocatalysis of oxygen reduction on carbon nanotubes with different surface functional groups in acid and alkaline solutions*, Int. J. Hydrogen Energy. 39 (2014) 16964–16975.

[17] J. Miao, H. Zhu, Y. Tang, Y. Chen, P. Wan, *Graphite felt electrochemically modified in H_2SO_4 solution used as a*

cathode to produce H_2O_2 for pre-oxidation of drinking water, Chem. Eng. J. 250 (2014) 312–318.

[18] R.S. Zhong, Y.H. Qin, D.F. Niu, J.W. Tian, X.S. Zhang, X.G. Zhou, S.G. Sun, W.K. Yuan, *Effect of carbon nanofiber surface functional groups on oxygen reduction in alkaline solution*, J. Power Sources. 225 (2013) 192–199.

[19] M. Gara, R.G. Compton, *Activity of carbon electrodes towards oxygen reduction in acid: A comparative study*, New J. Chem. 35 (2011) 2647.

[20] J. Yang, Y. Zhang, D.Y. Kim, *Electrochemical sensing performance of nanodiamond-derived carbon nano-onions: comparison with multiwalled carbon nanotubes, graphite nanoflakes, and glassy carbon*, Carbon. 98 (2016) 74–82.

[21] G. Li, Y. Zhang, *Highly selective two-electron oxygen reduction to generate hydrogen peroxide using graphite felt modified with N-doped graphene in an electro-Fenton system*, New J. Chem. 43 (2019) 12657–12667.

[22] Y. Xia, H. Shang, Q. Zhang, Y. Zhou, X. Hu, *Electrogeneration of hydrogen peroxide using phosphorus-doped carbon nanotubes gas diffusion electrodes and its application in electro-Fenton*, J. Electroanal. Chem. 840 (2019) 400–408.

[23] M.I. González-Sánchez, B. Gómez-Monedero, J. Agrisuelas, J. Iniesta, E. Valero, *Electrochemical performance of activated screen printed carbon electrodes for hydrogen peroxide and phenol derivatives sensing*, J. Electroanal. Chem. 839 (2019) 75–82.

[24] K. Aoki, M. Ishida, K. Tokuda, K. Hasebe, *Electrode kinetics of the oxidation of hydrogen peroxide at pretreated glassy carbon and carbon fiber electrodes*, J. Electroanal. Chem. Interfacial Electrochem. 251 (1988) 63–71.

[25] C. Costentin, M. Robert, J.-M. Savéant, *Concerted proton−electron transfers: electrochemical and related approaches*, Acc. Chem. Res. 43 (2010) 1019–1029.

[26] E. Laviron, *The use of linear potential sweep voltammetry and of a.c. voltammetry for the study of the surface electrochemical reaction of strongly adsorbed systems and of redox modified electrodes*, J. Electroanal. Chem. Interfacial Electrochem. 100 (1979) 263–270.

[27] D.C. Poudyal, A.K. Satpati, S. Kumar, S.K. Haram, *High sensitive determination of dopamine through catalytic*

oxidation and preconcentration over gold-multiwall carbon nanotubes composite modified electrode, Mater. Sci. Eng. C. 103 (2019) 109788.

[28] S. Schindler, T. Bechtold, *Mechanistic insights into the electrochemical oxidation of dopamine by cyclic voltammetry*, J. Electroanal. Chem. 836 (2019) 94–101.

[29] A.J. Bard, L.R. Faulkner, Electrochemical methods : fundamentals and applications, 2nd ed., Wiley, 2001.

[30] N. Wester, S. Sainio, T. Palomäki, D. Nordlund, V.K. Singh, L.-S. Johansson, J. Koskinen, T. Laurila, *Partially reduced graphene oxide modified tetrahedral amorphous carbon thin-film electrodes as a platform for nanomolar detection of dopamine*, J. Phys. Chem. C. 121 (2017) 8153–8164.

[31] A.F. Hagel, H. Albrecht, W. Dauth, W. Hagel, F. Vitali, I. Ganzleben, H.W. Schultis, P.C. Konturek, J. Stein, M.F. Neurath, M. Raithel, *Plasma concentrations of ascorbic acid in a cross section of the German population.*, J. Int. Med. Res. 46 (2018) 168–174.

[32] A.K. Bhakta, R.J. Mascarenhas, O.J. D'Souza, A.K. Satpati, S. Detriche, Z. Mekhalif, J. Dalhalle, *Iron nanoparticles decorated multi-wall carbon nanotubes modified carbon paste electrode as an electrochemical sensor for the simultaneous determination of uric acid in the presence of ascorbic acid, dopamine and l-tyrosine*, Mater. Sci. Eng. C. 57 (2015) 328–337.

[33] J. Huang, Y. Liu, H. Hou, T. You, *Simultaneous electrochemical determination of dopamine, uric acid and ascorbic acid using palladium nanoparticle-loaded carbon nanofibers modified electrode*, Biosens. Bioelectron. 24 (2008) 632–637.

[34] K.-C. Lin, T.-H. Tsai, S.-M. Chen, *Performing enzyme-free* H_2O_2 *biosensor and simultaneous determination for AA, DA, and UA by MWCNT–PEDOT film*, Biosens. Bioelectron. 26 (2010) 608–614.

[35] B. Habibi, M.H. Pournaghi-Azar, *Simultaneous determination of ascorbic acid, dopamine and uric acid by use of a MWCNT modified carbon-ceramic electrode and differential pulse voltammetry*, Electrochim. Acta. 55 (2010) 5492–5498.

[36] C. Wang, R. Yuan, Y. Chai, S. Chen, Y. Zhang, F. Hu, M. Zhang, *Non-covalent iron(III)-porphyrin functionalized multi-walled carbon nanotubes for the simultaneous determination*

of ascorbic acid, dopamine, uric acid and nitrite, Electrochim. Acta. 62 (2012) 109–115.

[37] Y. Li, P. Wang, L. Wang, X. Lin, *Overoxidized polypyrrole film directed single-walled carbon nanotubes immobilization on glassy carbon electrode and its sensing applications*, Biosens. Bioelectron. 22 (2007) 3120–3125.

[38] Y. Zhang, Y. Pan, S. Su, L. Zhang, S. Li, M. Shao, *A novel functionalized single-wall carbon nanotube modified electrode and its application in determination of dopamine and uric acid in the presence of high concentrations of ascorbic acid*, Electroanalysis. 19 (2007) 1695–1701.

[39] F. Wu, T. Huang, Y. Hu, X. Yang, Y. Ouyang, Q. Xie, *Differential pulse voltammetric simultaneous determination of ascorbic acid, dopamine and uric acid on a glassy carbon electrode modified with electroreduced graphene oxide and imidazolium groups*, Microchim. Acta. 183 (2016) 2539–2546.

[40] Z.-H. Sheng, X.-Q. Zheng, J.-Y. Xu, W.-J. Bao, F.-B. Wang, X.-H. Xia, *Electrochemical sensor based on nitrogen doped graphene: Simultaneous determination of ascorbic acid, dopamine and uric acid*, Biosens. Bioelectron. 34 (2012) 125–131.

[41] J. Breczko, M.E. Plonska-Brzezinska, L. Echegoyen, *Electrochemical oxidation and determination of dopamine in the presence of uric and ascorbic acids using a carbon nano-onion and poly(diallyldimethylammonium chloride) composite*, Electrochim. Acta. 72 (2012) 61–67.

Chapter 7

A wide-range solid state potentiometric pH sensor based on poly-dopamine coated carbon nano-onion electrodes[6]

7.1. Introduction

pH measurements are probably one of the most common and frequent analyses performed for quality control in pharmaceutical, chemical and food industries. In clinical diagnostics, the pH of body fluids is an indicator of how some organs are functioning [1–3], or can be correlated with the healing of wounds [4]. The most common methods to measure pH in aqueous solutions are the pH paper strips, which change their color depending on the pH, and the potentiometric method based on the glass electrode [5]. Other methods such as fluorescence, amperometry and conductimetry have also been reported, but they are less used [6–8].

Despite the glass electrode is the most extended pH sensor, it presents some drawbacks such as fragility, difficulty of miniaturization and frequent recalibration prior to use [9]. To overcome such limitations, new alternatives based on solid state electrodes have been developed [10,11]. They include the use of metal oxide-based electrodes [11–14] and the electrodeposition of polymers on conductive substrates [15–17]. In these approaches, the potentiometric response toward the

---

[6] *This Chapter was published in J.C. Zuaznabar-Gardona, A. Fragoso, Sensors and Actuators B: Chemical, 273 (2018) 664.*

pH is caused by a local variation of electric charges as a result of the proton exchange between the surrounding solution and the surface of the metallic oxide [18], or with the functional groups of the electrodeposited polymers [19].

Polymers possess some advantages over metallic oxides as sensing element in solid state potentiometric pH sensors since their properties can be tuned by changing the functional groups in the backbone or lateral chains [15]. As the thickness of the polymer layers are relatively easy to control, the methods to deposit polymers are compatible with miniaturization and mass production [20]. The first experiments using polymers as potentiometric pH sensor were carried out by Heineman et. al. [10] They reported the electrochemical oxidation of 1,2-diaminobenzene leading to the formation of a polymeric film on platinum electrodes. The coated electrodes showed a near Nernstian response toward pH changes. Since those early experiments, different polymers containing acid or basic moieties have been reported for applications in pH sensing. Polyethylenimine [21], polypropylenimine [22], polyaniline [23] and polypyrrole [19] are the most representative examples. Those polymers were electrodeposited on platinum [22], gold [24], glassy carbon (GC) [15], carbon fibers [25], carbon nanotubes [26], graphene [27], or screen printed electrodes [28].

In 2007, Messersmith et al. reported the self-polymerization of dopamine in basic aqueous media in the presence of air [29]. The reaction leads the formation of a thin film of polydopamine (PDA) on the surface of virtually any material. Metals [30], metal oxides

[31], nanoparticles [32], lipid layers [33] and polymers [34] have been successfully coated with PDA. The main feature of PDA coating is the possibility to anchor different molecules via Schiff-base formation and/or Michael addition in a single step [35]. The huge volume of research work on surface coating with PDA demonstrates its versatility as a tool in materials science, biology, and biomedical fields [36]. In the case of (bio)sensors, it could be considered as a universal platform to anchor enzymes [37], antibodies [38], and nucleic acids [39] on different substrates with better efficiency than conventional immobilization methods (i.e. electrostatic interactions, carbodiimide chemistry, etc) [40].

Substrates can be coated with polydopamine by two general methods: i) immersing the substrates in a basic ($pH = 8.5$) aqueous solution of dopamine in contact with air during a period of time (> 3 hours) [29], and ii) potential sweeping of a conductive material dipped in a buffered ($5 < pH < 7.4$) solution of dopamine [41]. Recently, it was reported the possibility of polymerizing dopamine in acidic media [42] and, most recently, to carry out the reaction in protic organic solvents such as methanol and ethanol [43]. These results widen the application of PDA coatings.

The structure of PDA is still in controversy. However, the most accepted structure is a copolymer containing indole rings with different (un)saturation degrees and open dopamine units (Scheme 7.1a) [44]. Due to the presence of various acid and basic moieties that can be (de)protonated, it could be expected that electrodes modified with PDA are responsive to pH changes. This has been exploited recently to construct a voltammetric pH sensor [45].

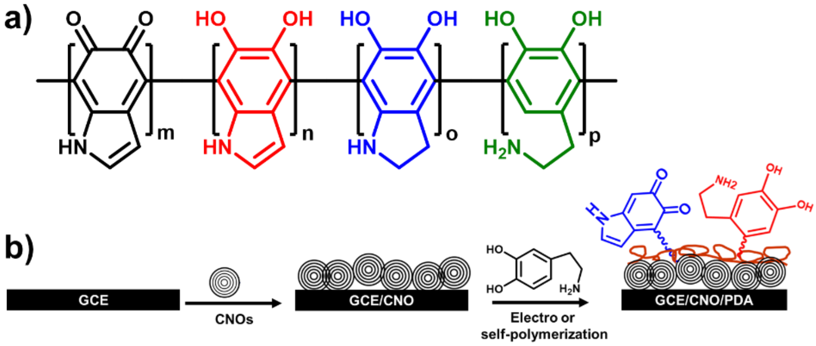

Scheme 7.1. a) Structure of polydopamine; b) General strategy for the modification of glassy carbon electrodes with CNOs and polydopamine.

In this Chapter, we report a novel potentiometric pH sensor based on PDA films coated on carbon nano-onion modified glassy carbon electrodes (GCE/CNO). Polydopamine films were deposited by chemical and electrochemical oxidation of dopamine. The effect of the deposition methods on the potentiometric pH response of the electrodes modified with PDA is addressed and the results are compared with a commercial glass electrode.

7.2. Materials and methods

Dopamine hydrochloride, piperidine, ethanol, methanol (MeOH), dimethylformamide (DMF), KCl, $K_4[Fe(CN)_6]$, $K_3[Fe(CN)_6]$ and all reagents used to prepare buffer solutions were of analytical grade and purchased from Sigma-Aldrich. Solutions were prepared with double distilled water (18.2 MΩcm) obtained from a Milli-Q system (Millipore, Madrid, Spain). CNOs were prepared by annealing of nanodiamonds as previously reported [46].

Universal buffer (UB) solutions were prepared by dissolving appropriated amounts of citric acid, sodium acetate, sodium hydrogen phosphate, sodium tetraborate and boric acid, being each 0.01 mol L^{-1}. Phosphate buffers (PB, 0.01 mol L^{-1}) were prepared by mixing different volumes of 0.01 mol L^{-1} Na_2HPO_4 and 0.1 mol L^{-1} KH_2PO_4 solutions. pH values were adjusted with 2 mol L^{-1} NaOH or 2 mol L^{-1} HCl.

Potentiometric measurements were carried out at room temperature with an electromotive force (EMF) high input impedance EMF16 multichannel data acquisition device from Lawson laboratories, Inc. (Malvern, USA). A double-junction Ag/AgCl (in 3 mol L^{-1} KCl with 1 mol L^{-1} lithium acetate bridge) electrode from Metrohm AG (Herisau, Switzerland) was used as reference electrode. All the experiments were carried out in 0.01 mol L^{-1} UB. Cyclic voltammograms were obtained using a PC-controlled CHI 660A electrochemical workstation (CH Instruments, Austin, USA) with a three-electrode cell configuration. Glassy carbon electrodes (CH Instruments model CHI104, 3.0 mm diameter) coated with CNOs films (GCE/CNO) were used as working electrode. A platinum wire and Ag/AgCl(sat) were used as counter and reference electrodes, respectively.

The pH values of the fabricated sensors were validated by comparison with a commercial combined pH electrode (5015T) coupled to a pH meter (Basic 20), both from Crison Instruments (Barcelona, Spain).

Environmental scanning electron microscopy (ESEM) was recorded in a Quanta 600 microscope (FEI Company, Inc.) under high vacuum at 25 kV. Samples were analyzed at a 10-mm working distance. Raman spectra were acquired with a Renishaw 2003 spectrometer operating at a wavelength of 514 nm) and 10 seconds of exposition time. The spectra were analyzed using Wire 3.2 software (Renishaw plc, United Kingdom). An ultrasonic tip (amplitude 60%, cycle 0.5, Ultraschall processor UP200S) was used to mechanically disperse CNOs. Static contact angles of deionized water on the various electrode surfaces were measured with an OCA15EC instrument equipped with DropImage Standard software. Measurements were made by delivering a 3 µL drop of Milli-Q water from a microsyringe onto the surface of the sample mounted on an illuminated horizontal stage.

7.2.1. Electrode preparation

GC electrodes were modified with CNOs (GCE/CNO) as it was described in Chapter 3 and it is show in Scheme 7.1b.

7.2.2. Electrochemical polymerization of dopamine on GCE/CNO

A PDA film was formed on the surface of GCE/CNO electrodes by electrochemical polymerization of dopamine in a buffer solution as reported previously with minor modifications [47]. Briefly, GCE/CNO electrodes were dipped in a solution containing 5 mmol L^{-1} of dopamine in PB 0.01 mol L^{-1} pH 6.5. Then, different potential cycles were applied to the electrodes between -0.4 to 1.5 V at 20 mV s^{-1}. After that, the modified electrodes (denoted as GCE/CNO/e-

PDA) were thoroughly washed with Milli-Q water, dried and stored at room temperature.

7.2.3. Chemical polymerization of dopamine on GCE/CNO

Modification of GCE/CNO electrodes with PDA film was also carried out by self-polymerization of dopamine in a protic organic solvent as reported recently [43]. GCE/CNO electrodes were immersed for different times in a solution containing 10 mmol L^{-1} of dopamine and 20 mmol L^{-1} of piperidine in methanol. After immersing for the desired time, the electrodes (denoted as GCE/CNO/c-PDA) were thoroughly washed with ethanol, followed by Milli-Q water. The GCE/CNO/c-PDA electrodes were dried and stored at room temperature.

7.3. Results and discussion

7.3.1. Polymerization of dopamine on GCE/CNO surfaces

GCE/CNO electrodes were coated with a film of polydopamine (PDA) following two procedures: i) self-polymerization of dopamine in methanol, and ii) electropolymerization of dopamine using cyclic voltammetry. The self-polymerization procedure consisted in immersing the GCE/CNO electrodes in a mixture containing dopamine and piperidine dissolved in methanol for a defined period of time [43]. Under these conditions, the self-polymerization of dopamine takes places leading to the formation of a PDA film on the substrate. The surface of the GCE/CNO/c-PDA electrodes was remarkably more hydrophilic than that of unmodified GCE/CNO. The contact angle of a water drop on the surface of GCE/CNO/c-PDA was reduced up 70^0 with respect to GCE/CNO (144^0). This is a direct result of the presence of polar groups on the surface of GCE/CNO/c-PDA because of the formation of the polydopamine film.

The electropolymerization of dopamine using cyclic voltammetry at low scan rates was the second procedure used to coat the GCE/CNO electrodes with PDA. Successive voltammograms obtained in 5 mmol L^{-1} dopamine in phosphate buffer pH 6.5 at GCE/CNO electrodes are shown in Figure 7.1a. The different peaks in the voltammograms are related with the redox processes that take place during the electropolymerization of dopamine [48]. The intensity of the peak at about 0.60 V continuously increased with the number of cycles. Such behavior reflects the continuous growth of PDA film on the surface of GCE/CNO. The modified surfaces (GCE/CNO/e-PDA) were also hydrophilic (contact angle = 60^0). These facts indicate the successful coating of GCE/CNO electrodes with PDA film by electropolymerization.

Raman spectroscopy is commonly used to characterize carbon-derived structures [49]. Generally, two peaks are used for most of Raman spectroscopic analyses of carbon materials, the so-called D and G bands. Figure 7.1b shows the Raman spectra of GCE/CNO surfaces before and after modification with PDA. The spectra are dominated by the D and G bands, located at around 1340 and 1580 cm^{-1}, respectively. Both bands are very intense and well-defined which reflects the high quality and compactness of the CNO layer [50]. The ratio between the intensity of D and G bands (I_D/I_G) can be related with the degree of functionalization of CNOs [49]. After the coating with PDA, the I_D/I_G ratio changed from 1.60 (unmodified GCE/CNO) to 1.74 and 1.67, in the case of self- and electropolymerization, respectively. This indicates a higher degree of functionalization in the case of self-polymerization with respect to the electrochemical procedure. ESEM images of PDA films deposited on GCE/CNO electrodes by electro- and self-polymerization are provided in Figure 7.1c and d, respectively. A slightly smoother film is obtained in the case of electropolymerization while self-polymerization provides a rougher coating.

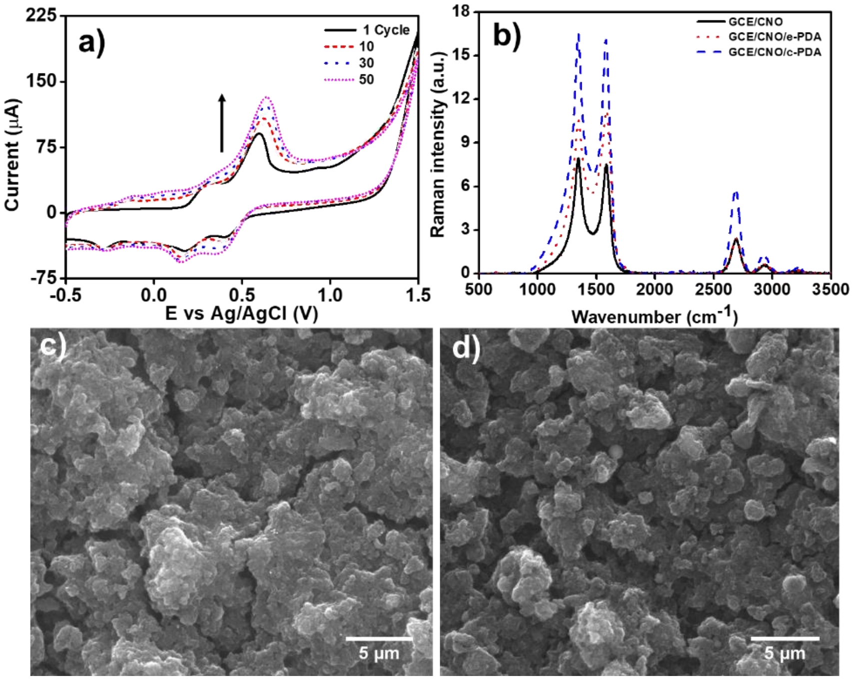

Figure 7.1. a) Cyclic voltammograms for the electropolymerization of 5 mmol L^{-1} dopamine in phosphate buffer pH 6.5 (scan rate was 20 mV/s). b) Raman spectra of GCE/CNO electrodes modified with PDA. ESEM images of PDA films deposited on GCE/CNO electrodes by c) electro- and d) self-polymerization of dopamine.

7.3.2. Potentiometric pH measurements

To evaluate the potentiometric response toward pH changes of GCE/CNO electrodes modified with PDA films, the redox behavior of PDA was investigated by cyclic voltammetry in solutions of universal buffer over a pH range of 1.50 to 10.50. Figures 7.2a and b depict cyclic voltammograms for the redox behavior of the PDA films deposited by electro- and self-polymerization on GCE/CNO electrodes, respectively. In both cases, anodic and cathodic peaks shift to more negative potentials as pH is increased.

Insets of Figure 7.2 correspond to the plot of anodic peak position against pH values, showing a good linear relationship over the pH range studied. Cathodic peaks behaved similar as anodic peaks did. The slope of the plot of peak position against pH values were (58.3 ± 0.9) and (60.1 ± 0.3) mV pH^{-1} for electro- and self-polymerization of dopamine, respectively. Thus, the PDA films deposited on GCE/CNOs electrodes have a Nernstian redox behavior which is pH dependent.

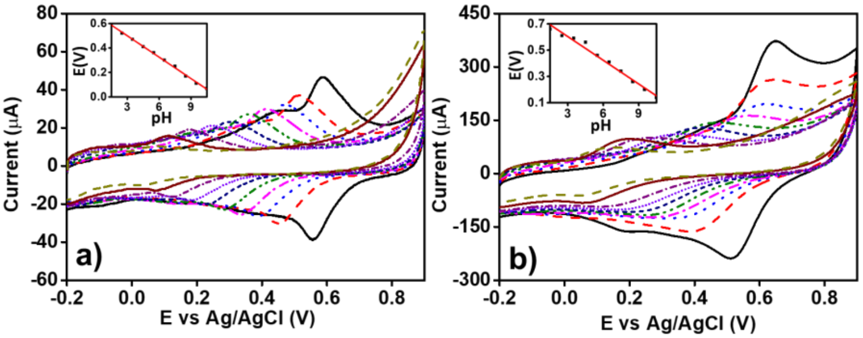

Figure 7.2. Cyclic voltammograms of PDA films deposited by a) electropolymerization and, b) self-polymerization on GCE/CNOs electrodes in different universal buffer solutions at pH ranging from 1.50 to 10.50. Insets: plots of anodic peak positions against pH.

Figures 7.3a and 7.3b depict the variations of electrode sensitivity (ΔEMF/pH) as a function of the self-polymerization time and the number of electropolymerization cycles, respectively. As can be seen, the sensitivity increases as both parameters increase to reach a maximum after 5.5 hours of polymerization or 50 potential cycles. These variations are due to the growth of the PDA film on GCE/CNO that increases the number of reactive groups on the electrode surface, with the corresponding increase in sensitivity. Thus, to obtain the highest sensitivity of the electrodes toward the changes of pH, the above values were used to coat the GCE/CNO electrode with PDA films in the following experiments.

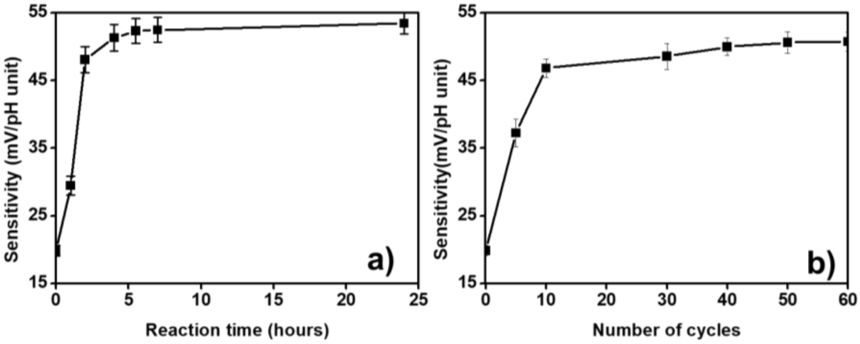

Figure 7.3. Variation of electrode sensitivity with a) the reaction time of self-polymerization, and b) the number of electropolymerization cycles.

The variations of EMF with pH for GCE/CNO and GCE electrodes modified with PDA are shown in Figure 7.4. The pH was varied from 1.7 to 10 by addition of aliquots of NaOH to the Universal Buffer solution. The GCE/CNO/c-PDA electrode showed an almost Nernstian potentiometric response of (53.1 ± 0.3) mV pH^{-1}, a value slightly higher than that of GCE/CNO/e-PDA (51.3 ± 0.4 mV pH^{-1}). Both responses were greater than those of the corresponding GCE/PDA electrodes (42.5 and 36.5 mV pH^{-1} for c- and e-PDA, respectively) and GCE/CNO in the absence of PDA (6.9 mV pH^{-1}). In all cases, the modified electrodes yield a stable signal in less than 15 seconds which is enough for practical purposes. The presence of the CNO layer increases the sensitivity of the sensor, most likely by acting as a high-area conductive support that enhances the response of the PDA coating to pH changes. A comparison between the analytical performance of the proposed pH-sensor and similar in the literature are presented in Table 7.1. The potentiometric response of polydopamine films was similar to those of well-established electrodeposited polymers.

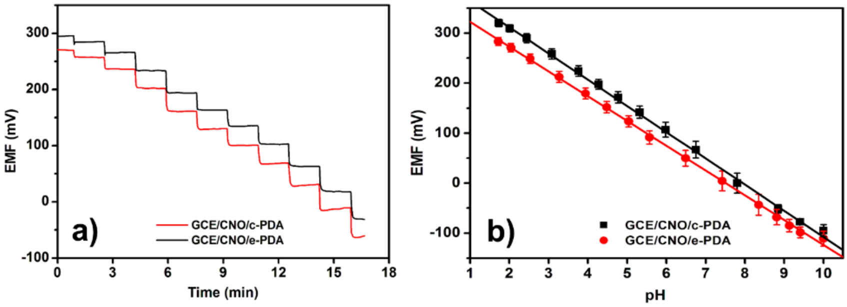

Figure 7.4. a) Typical potentiometric time traces of GCE/CNO/PDA sensors as the pH is increased by addition of NaOH aliquots. b) Calibration plots for GCE/CNO/PDA sensors.

Table 7.1. Comparison of the performance of the presented work and other electrodeposited polymers for pH sensing.

Polymer	**Electrode**	**Coating Method**	**Slope ($mV\ pH^{-1}$)**	**S**	**Ref.**
PDAB	Pt	CV	53	B	[10]
PEI	Pt	CV	42	B	[21]
PPI	Pt	CV	44	B	[22]
PANI	GCE	Drop-casting	53	B	[23]
	CF	CV	60	B	[25]

Table 7.1. Comparison of the performance of the presented work and other electrodeposited polymers for pH sensing (*Continuation*).

Polymer	**Electrode**	**Coating Method**	**Slope ($mV\ pH^{-1}$)**	**S**	**Ref.**
PANI	SWNTs	Potentiostatic	58	B	[26]
	SPE	CV	58	B	[28]
	GOx/G	Drop-casting	40	B	[27]
PDA	GCE	CV	36	B	**This work**
		Self-P	42		
	GCE/CNO	CV	51	B	
		Self-P	53		

S: sample, B: buffered, PDAB: poly-(1,2-diaminobenzene), PEI: polyethylenimine, PPI: polypropylenimine, PANI: polyaniline, PDA: polydopamine, CF: carbon fibers, SWNTs: single-walled carbon nanotubes, SPE: screen-printed electrodes, GOx: graphene oxide, G: graphite, Self-P: self-polymerization.

Repeatability is an important parameter in any sensor. It was addressed by performing different calibration curves using the same GCE/CNO electrodes modified with PDA by electro- or self-polymerization (intrasensor repeatability). The results of three consecutive repetitions yield a sensitivity of (51.2 ± 0.2) mV pH^{-1} and an intercept of (394 ± 8) mV in the case of electropolymerization. In the case of self-polymerization, the same experiment yield sensitivity of (53.4 ± 0.4) mV pH^{-1} and intercept of (360 ± 7) mV. (Figure 7.5a). These results are similar to those reported with other polymers [19].

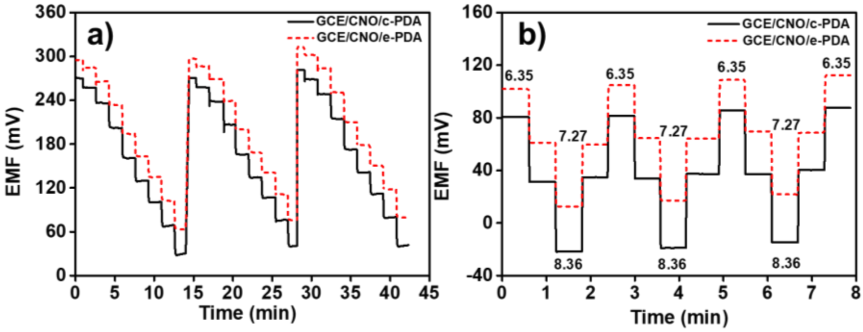

Figure 7.5. a) Repeatability of the GCE/CNO modified with polydopamine films within the pH 1.70 to 6.30 range. b) Carry-over evaluation over pH 6.35 to 8.36.

In general, sensors should respond dynamically toward variations of the target analyte. To evaluate this, GCE/CNO electrodes modified with PDA films were sequentially immersed in solutions with different pH values. The results are shown in Figure 7.5b. The electrodes displayed an almost instantaneous and reversible response toward variation of the pH. No significant differences were observed in the dynamical response between electrodes modified following the two procedures for PDA coating.

For further real applications, it is also necessary to evaluate the interference effect of common ions on the potentiometric response of the GCE/CNO electrodes modified with PDA. Table 7.2 shows the selectivity coefficient for Li^+, Na^+ and K^+ ions calculated by the separated solutions method [51]. These results indicate that these monovalent ions do not affect the potentiometric response of the GCE/CNO/PDA electrodes. The evaluation of the selectivity coefficients for NH_4^+, $Mg^{2+,}$ and Ca^{2+} ions was difficult since they were able to change the pH due to hydrolysis of their corresponding salts.

Table 7.2. Selectivity coefficients calculated by the separated solutions method for the GCE/CNO/PDA electrodes.

	$\log K^{pot}_{H^+,X}$	
Ions (X)	**GCE/CNO/c-PDA**	**GCE/CNO/e-PDA**
Li^+	-5.7 ± 0.1	-6.1 ± 0.1
Na^+	-5.8 ± 0.1	-5.7 ± 0.1
K^+	-5.9 ± 0.1	-6.0 ± 0.1

The stability over time of sensors is another important parameter to take into account. The lifetime of the electrodes modified with PDA was evaluated by measuring their responses (i.e. sensitivity) toward pH variations in universal buffer solutions. The electrodes were stored at room temperature without any light-protection. The sensitivity values measured during four weeks are summarized in Table 7.3. As can be seen, the sensitivity values of the e-PDA film are essentially the same within the experimental error while the values of the c-PDA film show an increase of 5.3% in the first 3 weeks. This could be ascribed to some re-organization of the PDA film with time, although in practice these variations could be compensated with a re-calibration of the sensor before use. In addition, the PDA coatings were stable in water for several months. Only in strong basic media (>1 mol L^{-1} NaOH), the polydopamine coating is destroyed, demonstrating the high stability of the PDA films.

The response of the GCE/CNO electrodes modified with PDA by electropolymerization was quite stable during the period of time analyzed. In the case of the electrodes prepared by self-polymerization, the sensitivity tended to slightly increase (~ 5%) during the period under study. This behavior indicates that the PDA film prepared by self-polymerization is further stabilized.

Table 7.3. Lifetime for the GCE/CNO/PDA electrodes

	Sensitivity (mV pH^{-1})	
Weeks	**GCE/CNO/c-PDA**	**GCE/CNO/e-PDA**
0	52.3 ± 0.8	51.5 ± 0.4
1	53.3 ± 0.4	51.9 ± 0.7
2	54.6 ± 0.5	51.8 ± 0.4
3	55.1 ± 0.7	51.1 ± 0.4
4	53.4 ± 0.3	50.5 ± 0.3

After calibration, the GCE/CNO/PDA electrodes were used to measure the pH of five different buffered samples. The results were compared to the pH values obtained by using a commercial glass electrode. Figure 7.6 depicts a comparison of the results obtained for both methods.

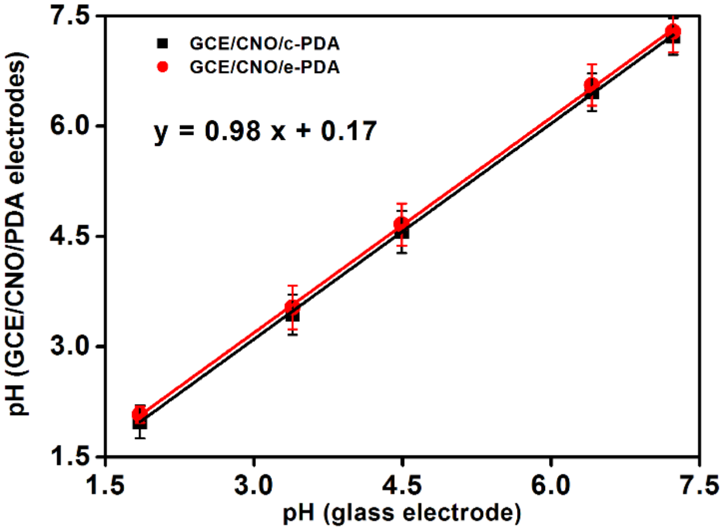

Figure 7.6. Comparison of pH values obtained for five buffered samples using GCE/CNO/PDA electrodes and the glass electrode.

The results show an excellent correspondence between the pH values obtained using the GCE/CNO/PDA electrodes and those measured by the conventional glass electrodes. The effect of the ionic strength and buffer compositions on the performance of the sensor should be addressed in further studies.

7.4. Conclusions

Glassy carbon electrodes were modified with carbon nano-onions and further coated with polydopamine films. Two procedures were employed: electro- and self-polymerization of dopamine. The modified electrodes were characterized by ESEM, Raman spectroscopy and cyclic voltammetry revealing a uniform coating of carbon nano-onions with PDA. The analytical performance of GCE/CNO modified with PDA was evaluated as potentiometric pH sensors. It is demonstrated that the electro- and specially the self-polymerization of dopamine are suitable methods to produced PDA films as potentiometric transducers for pH changes. The CNO layer improves the potentiometric response of the PDA films by providing a high-area conductive support layer. The electrodes displayed an almost Nernstian potentiometric response toward changes of pH. Selectivity, repeatability and time stability were also evaluated as a function of the method to coat the CNO surface with PDA with negligible interference effects from monovalent cations, fast and reversible behavior toward variations of pH and good long-term stability. The sensor responses showed an excellent correspondence between the pH values obtained using the GCE/CNO/PDA electrodes and those measured with glass electrodes. These results are comparable to other reported devices based on electropolymerized amines over graphite and noble metal electrodes and have the advantage of an ease of fabrication and excellent reproducibility. Thus, coating CNOs with electrochemically responsive polymers is a new strategy to develop analytical devices and the results are very promising for the miniaturization and integration of pH sensors in (bio)analytical devices.

References

[1] A.J. Wein, L.R. Kavoussi, A.W. Partin, C.A. Peters, Campbell-Walsh Urology, in: A.J. Wein, L.R. Kavoussi, A.W. Partin, C.A. Peters (Eds.), Campbell-Walsh Urol., 11th ed., Elsevier, Philadelphia, 2015: p. 4176.

[2] M.C. Houston, *Pleural fluid pH: Diagnostic, therapeutic, and prognostic value*, Am. J. Surg. 154 (1987) 333–337.

[3] S. Baliga, S. Muglikar, R. Kale, *Salivary pH: A diagnostic biomarker.*, J. Indian Soc. Periodontol. 17 (2013) 461–5.

[4] L.A. Schneider, A. Korber, S. Grabbe, J. Dissemond, *Influence of pH on wound-healing: a new perspective for wound-therapy?*, Arch. Dermatol. Res. 298 (2007) 413–420.

[5] G. Eisenman, Glass electrodes for hydrogen and other cations, Marcel Dekker Inc., New York, 1967.

[6] M. Kneen, J. Farinas, Y. Li, A.S. Verkman, *Green fluorescent protein as a noninvasive intracellular pH indicator*, Biophys. J. 74 (1998) 1591–1599.

[7] M. Stredanský, A. Pizzariello, S. Stredanská, S. Miertuš, *Amperometric pH-sensing biosensors for urea, penicillin, and oxalacetate*, Anal. Chim. Acta. 415 (2000) 151–157.

[8] A.Q. Contractor, T.N. Sureshkumar, R. Narayanan, S. Sukeerthi, R. Lal, R.S. Srinivasa, *Conducting polymer-based biosensors*, Electrochim. Acta. 39 (1994) 1321–1324.

[9] U. Oesch, D. Ammann, W. Simon, *Ion-selective membrane electrodes for clinical use.*, Clin. Chem. 32 (1986) 1448–1459.

[10] W.R. Heineman, H.J. Wieck, A.M. Yacynych, *Polymer film chemically modified electrode as a potentiometric sensor*, Anal. Chem. 52 (1980) 345–346.

[11] J. Park, J. Kim, H. Quan, *A surface renewable iridium oxide–glass composite hydrogen ion electrode*, Microchem. J. 95 (2010) 102–106.

[12] A. Eftekhari, *pH sensor based on deposited film of lead oxide on aluminum substrate electrode*, Sensors Actuators B Chem. 88 (2003) 234–238.

[13] L. Qingwen, L. Guoan, S. Youqin, *Response of nanosized cobalt oxide electrodes as pH sensors*, Anal. Chim. Acta. 409

(2000) 137–142.

[14] G.K. Mani, M. Morohoshi, Y. Yasoda, S. Yokoyama, H. Kimura, K. Tsuchiya, *ZnO-based microfluidic pH sensor:A versatile approach for quick recognition of circulating tumor cells in blood*, ACS Appl. Mater. Interfaces. 9 (2017) 5193–5203.

[15] T. Lindfors, A. Ivaska, *pH sensitivity of polyaniline and its substituted derivatives*, J. Electroanal. Chem. 531 (2002) 43–52.

[16] B. Lakard, D. Magnin, O. Deschaume, G. Vanlancker, K. Glinel, S. Demoustier-Champagne, B. Nysten, P. Bertrand, S. Yunus, A.M. Jonas, *Optimization of the structural parameters of new potentiometric pH and urea sensors based on polyaniline and a polysaccharide coupling layer*, Sensors Actuators B Chem. 166 (2012) 794–801.

[17] E.E. Stoikova, M.I. Sorvin, D.N. Shurpik, H.C. Budnikov, I.I. Stoikov, G.A. Evtugyn, *Solid-contact potentiometric sensor based on polyaniline and unsubstituted pillar[5]arene*, Electroanalysis. 27 (2015) 440–449.

[18] P. Shuk, *New metal-oxide-type pH sensors*, Solid State Ionics. 86–88 (1996) 1115–1120.

[19] B. Lakard, G. Herlem, S. Lakard, R. Guyetant, B. Fahys, *Potentiometric pH sensors based on electrodeposited polymers*, Polymer. 46 (2005) 12233–12239.

[20] T.V. Shishkanova, P. Matějka, V. Král, I. Šeděnková, M. Trchová, J. Stejskal, *Optimization of the thickness of a conducting polymer, polyaniline, deposited on the surface of poly(vinyl chloride) membranes: A new way to improve their potentiometric response*, Anal. Chim. Acta. 624 (2008) 238–246.

[21] G. Herlem, B. Lakard, M. Herlem, B. Fahys, *pH sensing at Pt electrode surfaces coated with linear polyethylenimine from anodic polymerization of ethylenediamine*, J. Electrochem. Soc. 148 (2001) 435–438.

[22] B. Lakard, G. Herlem, M. de Labachelerie, W. Daniau, G. Martin, J.-C. Jeannot, L. Robert, B. Fahys, *Miniaturized pH biosensors based on electrochemically modified electrodes with biocompatible polymers*, Biosens. Bioelectron. 19 (2004) 595–606.

[23] T. Lindfors, S. Ervelä, A. Ivaska, *Polyaniline as pH-sensitive component in plasticized PVC membranes*, J. Electroanal.

Chem. 560 (2003) 69–78.

[24] G. Herlem, C. Goux, B. Fahys, F. Dominati, A.-M. Gonçalves, C. Mathieu, E. Sutter, A. Trokourey, J.-F. Penneau, *Surface modification of platinum and gold electrodes by anodic oxidation of pure ethylenediamine*, J. Electroanal. Chem. 435 (1997) 259–265.

[25] X. Zhang, B. Ogorevc, J. Wang, *Solid-state pH nanoelectrode based on polyaniline thin film electrodeposited onto ion-beam etched carbon fiber*, Anal. Chim. Acta. 452 (2002) 1–10.

[26] M. Kaempgen, S. Roth, *Transparent and flexible carbon nanotube/polyaniline pH sensors*, J. Electroanal. Chem. 586 (2006) 72–76.

[27] P. Salvo, N. Calisi, B. Melai, B. Cortigiani, M. Mannini, A. Caneschi, G. Lorenzetti, C. Paoletti, T. Lomonaco, A. Paolicchi, I. Scataglini, V. Dini, M. Romanelli, R. Fuoco, F. Di Francesco, *Temperature and pH sensors based on graphenic materials*, Biosens. Bioelectron. 91 (2017) 870–877.

[28] T. Guinovart, G. Valdés-Ramírez, J.R. Windmiller, F.J. Andrade, J. Wang, *Bandage-based wearable potentiometric sensor for monitoring wound pH*, Electroanalysis. 26 (2014) 1345–1353.

[29] H. Lee, S.M. Dellatore, W.M. Miller, P.B. Messersmith, *Mussel-inspired surface chemistry for multifunctional coatings*, Science. 318 (2007) 426–430.

[30] A.W.G. Nijhuis, J.J.J.P. van den Beucken, O.C. Boerman, J.A. Jansen, S.C.G. Leeuwenburgh, *1-step versus 2-step immobilization of alkaline phosphatase and bone morphogenetic protein-2 onto implant surfaces using polydopamine*, Tissue Eng. Part C Methods. 19 (2013) 610–619.

[31] D. He, X. He, X. Yang, H.W. Li, *A smart ZnO@polydopamine-nucleic acid nanosystem for ultrasensitive live cell mRNA imaging by the target-triggered intracellular self-assembly of active DNAzyme nanostructures*, Chem. Sci. 8 (2017) 2832–2840.

[32] M. Martín, P. Salazar, R. Villalonga, S. Campuzano, J.M. Pingarrón, J.L. González-Mora, Z. Huang, B. Xu, H. Lee, S.-W. Cho, *Preparation of core–shell* Fe_3O_4*@poly(dopamine) magnetic nanoparticles for biosensor construction*, J. Mater. Chem. B. 2 (2014) 739–746.

[33] L. Zheng, L. Xiong, D. Zheng, Y. Li, Q. Liu, K. Han, W. Liu, K. Tao, S. Yang, J. Xia, *Bilayer lipid membrane biosensor with enhanced stability for amperometric determination of hydrogen peroxide*, Talanta. 85 (2011) 43–48.

[34] C. Liu, X. Lei, L. Wang, J. Jia, X. Liang, X. Zhao, H. Zhu, *Investigation on the removal performances of heavy metal ions with the layer-by-layer assembled forward osmosis membranes*, Chem. Eng. J. 327 (2017) 60–70.

[35] N. Huang, S. Zhang, L. Yang, M. Liu, H. Li, Y. Zhang, S. Yao, *Multifunctional electrochemical platforms based on the Michael addition/Schiff base reaction of polydopamine modified reduced graphene oxide: construction and application*, ACS Appl. Mater. Interfaces. 7 (2015) 17935–17946.

[36] Y. Liu, K. Ai, L. Lu, *Polydopamine and its derivative materials: synthesis and promising applications in energy, environmental, and biomedical fields*, Chem. Rev. 114 (2014) 5057–5115.

[37] M. Dai, T. Huang, L. Chao, Q. Xie, Y. Tan, C. Chen, W. Meng, *Horseradish peroxidase-catalyzed polymerization of l-DOPA for mono-/bi-enzyme immobilization and amperometric biosensing of H_2O_2 and uric acid*, Talanta. 149 (2016) 117–123.

[38] G.A. Ortega, S. Pérez-Rodríguez, E. Reguera, *Magnetic paper – based ELISA for IgM-dengue detection*, RSC Adv. 7 (2017) 4921–4932.

[39] G. Loget, J.B. Wood, K. Cho, A.R. Halpern, R.M. Corn, *Electrodeposition of polydopamine thin films for DNA patterning and microarrays*, Anal. Chem. 85 (2013) 9991–9995.

[40] G. Ortega, J.C. Zuaznabar-Gardona, O. Morales, E. Reguera, *Immobilization of dengue specific IgM antibodies on magnetite nanoparticles by using facile conjugation strategies*, RSC Adv. 6 (2016) 98457–98465.

[41] K. Liu, W.Z. Wei, J.X. Zeng, X.Y. Liu, Y.P. Gao, *Application of a novel electrosynthesized polydopamine-imprinted film to the capacitive sensing of nicotine*, Anal. Bioanal. Chem. 385 (2006) 724–729.

[42] W. Zheng, H. Fan, L. Wang, Z. Jin, *Oxidative self-polymerization of dopamine in an acidic environment*, Langmuir. 31 (2015) 11671–11677.

[43] I. You, H. Jeon, K. Lee, M. Do, Y.C. Seo, H.A. Lee, H. Lee, *Polydopamine coating in organic solvent for material-independent immobilization of water-insoluble molecules and avoidance of substrate hydrolysis*, J. Ind. Eng. Chem. 46 (2017) 379–385.

[44] J. Liebscher, R. Mrówczyński, H.A. Scheidt, C. Filip, N.D. Hădade, R. Turcu, A. Bende, S. Beck, *Structure of polydopamine: a never-ending story?*, Langmuir. 29 (2013) 10539–10548.

[45] M. Amiri, E. Amali, A. Nematollahzadeh, H. Salehniya, *Poly-dopamine films: voltammetric sensor for pH monitoring*, Sensors Actuators B Chem. 228 (2016) 53–58.

[46] E. Wajs, A. Molina-Ontoria, T.T. Nielsen, L. Echegoyen, A. Fragoso, *Supramolecular solubilization of cyclodextrin-modified carbon nano-onions by host–guest interactions*, Langmuir. 31 (2015) 535–541.

[47] L. Zhang, H. Bin Yin, J.J. Luo, P.H. Yang, J.Y. Cai, *Construction of electrochemical impedance sensor based on poly dopamine-hyaluronic acid composite membrane for detection of hydrogen peroxide*, Chinese J. Anal. Chem. 41 (2013) 534–539.

[48] X. Dong, X. Lu, K. Zhang, Y. Zhang, *Chronocoulometric DNA biosensor based on a glassy carbon electrode modified with gold nanoparticles, poly(dopamine) and carbon nanotubes*, Microchim. Acta. 180 (2013) 101–108.

[49] D. Codorniu Pujals, O. Arias de Fuentes, L.F. Desdín García, E. Cazzanelli, L.S. Caputi, *Raman spectroscopy of polyhedral carbon nano-onions*, Appl. Phys. A. 120 (2015) 1339–1345.

[50] D. Roy, M. Chhowalla, H. Wang, N. Sano, I. Alexandrou, T.. Clyne, G.A.. Amaratunga, *Characterisation of carbon nano-onions using Raman spectroscopy*, Chem. Phys. Lett. 373 (2003) 52–56.

[51] E. Bakker, E. Pretsch, P. Bühlmann, *Selectivity of potentiometric ion sensors*, Anal. Chem. 72 (2000) 1127–1133.

Chapter 8

Development of highly sensitive IgA immunosensors based on co-electropolymerized L-DOPA/dopamine carbon nano-onion modified electrodes[7]

8.1. Introduction

Immunoassays are undoubtedly useful analytical tools in today medical diagnosis and biochemical analysis. They are based on the specific affinity between an antibody and its corresponding antigen (e.g. antibodies, proteins, hormones, viruses, toxins, etc.) [1]. Various assay formats have been developed such as enzyme-linked immunosorbent assays (ELISA) [2], radioimmunoassay [3], time-resolved fluorescence [4], flow injection [5], quartz crystal microbalance [6], surface plasmon resonance [7] and lateral flow [8]. Among them, ELISAs and lateral flow immunoassays are the most popular and widely used in research and medical laboratories.

In recent years, electrochemical immunoassays have attracted great interest among industry and academy [9]. Their working principle relies on monitoring the specific recognition event between the capture antibody and its antigen by using an electrochemical technique [10]. Different reviews have summarized the practical aspects [11] and the various available architectures and transduction strategies to develop electrochemical immunoassays [9]. They are of

---

[7] *This Chapter was published in J.C. Zuaznabar-Gardona, A. Fragoso, Biosensors & Bioelectronics, 141 (2019) 111357.*

particular interest given the combination of specificity and selectivity of the immunoreaction with the sensitivity, short response times, low cost of instrumentation and possibility of lab decentralization offered by electrochemical techniques [12].

Nanomaterials have been successfully applied to develop novel and sensitive electrochemical immunoassays [13]. Noble metal nanoparticles, chalcogenides, metal oxide nanoparticles and carbon-based materials could be used as platform for attaching the capture probes as well as labels of the secondary antibody [14]. The incorporation of nanomaterials in electrochemical immunosensors results in an enhancement of the sensitivity and improvement of the limit of detection.

Carbon nanotubes and graphene are widely used as platforms to anchor biorecognition elements [15,16]. Recent bioanalytical applications of CNOs include their incorporation on a polymeric composite and gold nanoparticles to detect human chorionic gonadotropin [17] and carcinoembryonic antigen [18] have been reported. Additionally, as our group has previously demonstrated, CNOs greatly improve biosensor sensitivity by a combination of enhanced electron transfer rate and adsorption of redox labels [19,20].

An important aspect in the development of electrochemical immunoassays is the immobilization of the biorecognition elements on the electrode surface in a way that provides a large immunoreagent load with optimal orientation and spacing [21]. Polymeric films derived from catecholamines such as dopamine have recently been explored for the immobilization of a wide range of biomolecules [22]. Other catecholamines, such as 3-(3,4-dihydroxyphenyl)-L-alanine) (L-DOPA) which bears a carboxylic acid group have been rarely used for this purpose [23], while the copolymerization of catecholamine mixtures to anchor biomolecules has not been reported.

In this Chapter, we explore the co-electropolymerization of L-DOPA and DA on glassy carbon electrodes covered with a film of oxidized CNOs and apply it to construct a novel and sensitive electrochemical immunosensor for immunoglobulin A (IgA). IgA antibodies are the second most prevalent immunoglobulin in circulation and its deficiency is related with different immune diseases [24]. Furthermore, IgA concentration is an indication of overall body condition and, in pathological situations, it may help in determining cancer staging and other diagnostic conditions [25].

8.2. Materials and methods

Dopamine hydrochloride (DA), 3-(3,4-dihydroxyphenyl)-L-alanine) (L-DOPA), dimethylformamide (DMF), KCl, $K_4[Fe(CN)_6]$, $K_3[Fe(CN)_6]$, 1-ethyl-3-(3-dimethyl-aminopropyl) carbodiimide hydrochloride (EDC), N-hydroxysuccinimide (NHS), sodium acetate, acetic acid, 97% sulfuric acid, ethanolamine, 2-(N-morpholino)ethanesulfonic acid (MES), 3,3′,5,5′-tetramethylbenzidine (TMB), anti-human IgA (μ-chain specific) antibody produced in goat (α-IgA), IgA from human colostrum, anti-human IgA-peroxidase (α-IgA-HRP), human IgG, human IgE, bovine serum albumin (BSA), calf serum and skim milk were obtained from Sigma–Aldrich and were used as received. Solutions were prepared with double distilled water (18.2 MΩ cm) obtained from a Milli-Q® system (Millipore, Madrid, Spain). CNOs were prepared and further oxidized as previously reported [26]. Phosphate-buffered saline (PBS) and PBS with 0.05% v/v Tween 20 were made from tablets purchased from Sigma–Aldrich. Phosphate buffers (PB, 0.01 mol L^{-1}) were prepared by mixing different volumes of 0.01 mol L^{-1} Na_2HPO_4 and 0.01 mol L^{-1} NaH_2PO_4 solutions. pH values were adjusted with 1 mol L^{-1} NaOH or 1 mol L^{-1} HCl.

All electrochemical measurements were obtained using a PC-controlled CHI 660A electrochemical workstation (CH Instruments, Austin, USA) with a three-electrode cell configuration. Glassy carbon electrodes (CH Instruments model CHI104, 3.0 mm diameter) coated with oxidized CNO films (GCE/CNO-OXI) were used as working electrode. A platinum wire and Ag/AgCl(sat) were used as counter and reference electrodes, respectively.

8.2.1. Electrode preparation

GC electrodes were modified with CNO-OXI (GCE/CNO-OXI) as it was described in Chapter 3 and it is show in Scheme 8.1a.

8.2.2. Electrochemical co-polymerization of catecholamines on GCE/CNO-OXI

A poly(L-DOPA/DA) film was formed on the surface of GCE/CNO-OXI electrodes by electrochemical polymerization of L-DOPA and DA mixtures (Scheme 8.1a). Briefly, GCE/CNO-OXI electrodes were dipped in a solution containing different molar ratios of L-DOPA and DA in 0.01 mol L^{-1} PB pH 6.5. Then, 10 potential cycles were applied to the electrodes between -0.5 to 1.5 V at 0.1 V s^{-1}. After that, the modified electrodes (denoted as GCE/CNO-OXI/poly(L-DOPA/DA) were stabilized by cycling 20 times the potential between -0.2 to 0.9 V at 0.1 V s^{-1} in 0.01 mol L^{-1} PB pH 6.5. Finally, the electrodes were thoroughly washed with Milli-Q® water, dried and stored at room temperature.

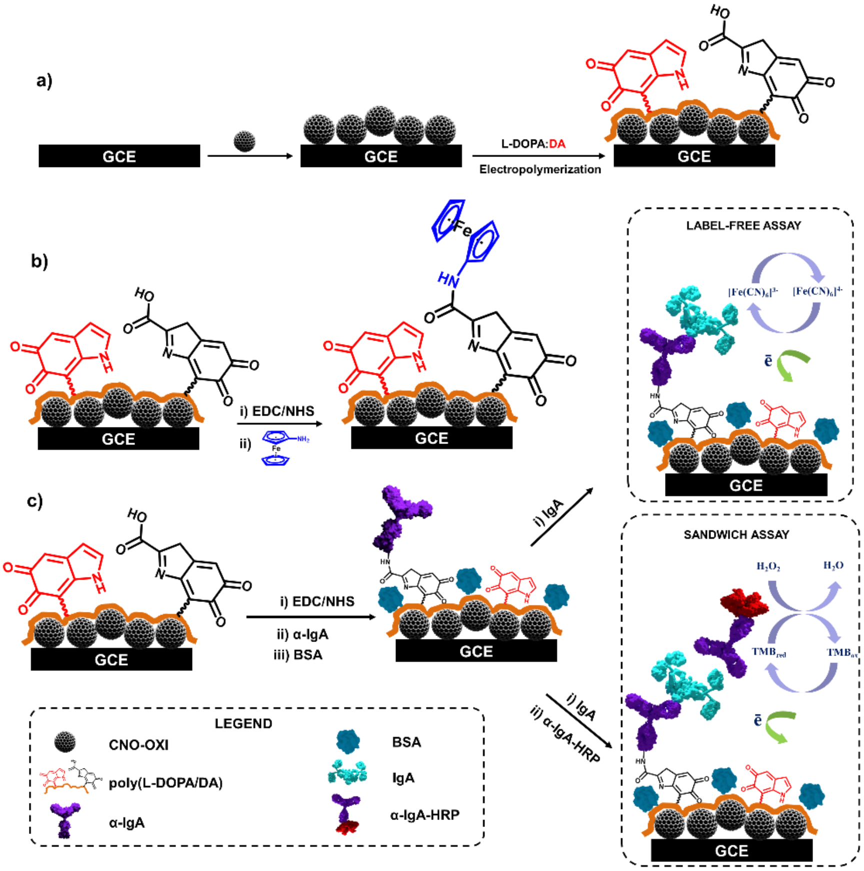

Scheme 8.1. Schematic representation of the steps involved in: a) the modification of the GCE surfaces with CNO-OXI and poly(L-DOPA/DA) film, b) the attachment of aminoferrocene and, c) the construction of the two assay formats for the electrochemical detection of IgA antibodies.

8.2.3. Aminoferrocene modified GCE/CNO-OXI/poly(L-DOPA/DA)

GCE/CNO-OXI/poly(L-DOPA/DA) electrodes were immersed in a stirring solution containing 5 mmol L^{-1} of EDC and NHS in 0.1 mol L^{-1} MES buffer pH 5 for 30 min to activate the COOH groups of the poly(L-DOPA/DA) films. Then, the electrodes were stirred for 1 hour in 250 µmol L^{-1} aminoferrocene ($FcNH_2$) solution in PBS containing 10% v/v DMSO (Scheme 8.1b). The modified electrodes were thoroughly washed with Milli-Q water, dried with N_2 and stored at room temperature.

8.2.4. IgA immunosensor

The carboxylic acid moieties of the GCE/CNO-OXI/poly(L-DOPA/DA) were activated with EDC and NHS followed by immersion in 100 µg mL^{-1} α-IgA in PBS pH 7.4 for 1.5 hours at room temperature followed by 1% BSA in PBS pH 7.4 for 30 minutes (Scheme 8.1c). After washing with PBS solution to remove unbound molecules, electrodes were dried and stored at 4^0C before being used.

8.2.4.1. Detection of IgA antibodies

Label-free assay: The immunosensors were incubated with 200 µL IgA target in PBS pH 7.4 at different concentrations for 1 hour and rinsed with PBS. Differential pulse voltammograms were recorded between -0.2 and +1 V (vs. Ag/AgCl reference electrode) in 1 mmol L^{-1} $[Fe(CN)_6]^{3-/4-}$ in PBS pH 7.4. A calibration curve was constructed from the change in the DPV peak current before and after the antigen-antibody reaction at different IgA concentrations.

Sandwich type assay: In this case, after the capture of IgA, the immunosensors were incubated with HRP-labeled anti-human IgA (1:1000 dilution) for 15 minutes followed by rinsing with PBS. Amperometric measurements were carried out at 0.2 V in a 5 mL electrochemical cell containing TMB liquid substrate in 0.1 mol L^{-1} PB pH 6 (1:10 v/v) under stirring conditions at room temperature. Current values *vs.* IgA concentration were used to obtain the calibration plots.

In all cases, control measurements were carried out with electrodes prepared in the absence of CNOs (GCE/poly(L-DOPA/DA).

8.2.5. Colorimetric detection of IgA

Nunc® 96-well polypropylene plates from Thermo Fisher Scientific (Madrid, Spain) were incubated overnight at 4°C with 100 µL of 10 µg mL^{-1} α-IgA in carbonate buffer pH 9.6. After washing, the remaining active sites were blocked with 1% BSA in PBS at 37ºC for 1 hour. After rinsing, 100 µL of IgA standards were added, incubated for 1 hour and washed. Detection was carried out by addition of 100 µL of anti-human IgA HRP-conjugate (1:10 000 in PBS) for 15 minutes. After washing and incubation with 100 µL of TMB for 10 min, the reaction was stopped with 1 mol L^{-1} H_2SO_4 and the absorbance of each well was measured at 450 nm in a Wallac Victor2 1420 multiplate reader from Perkin-Elmer. The washing steps consisted in soaking four times the wells with 200 µL of PBS with 0.05% v/v Tween 20.

8.2.6. Analysis of spiked serum samples and stability study of GCE/CNO-OXI/poly(L-DOPA/DA)/α-IgA

A calf serum sample was diluted with PBS pH 7.4 (1:100 v/v) and spiked with 70 and 1000 ng mL^{-1} of IgA and the current response was measured as described for the sandwich type assay. Recoveries were calculated by dividing the obtained currents with those expected from the corresponding calibration curve (Figure 8.4b).

For the stability study, the biosensors were stored in StabilCoat® Plus Stabilizer (from Surmodics) for one week at 4ºC and 37ºC in order to test their stability in real time and under accelerated conditions. The sandwich assay was then constructed using 1000 ng mL^{-1} of IgA in PBS pH 7.4 and the current was measured and compared with the calibration curve.

All measurements were carried out in triplicate in three freshly prepared biosensors.

8.3. Results and discussion

8.3.1. Electrochemical copolymerization of L-DOPA and DA mixtures on GCE/CNO-OXI

CNO-OXI were prepared by nanodiamond annealing followed by acid oxidation and consist in ~5 nm nanoparticles with 5-6 graphitic layers (Figure 8.1a). The GCE/CNO-OXI electrodes were coated with a film of poly(L-DOPA/DA) by oxidative co-electropolymerization of a mixture of L-DOPA and DA in a buffer solution using cyclic voltammetry. The ESEM image of the GCE/CNO-OXI/poly(L-DOPA/DA) electrode (Figure 8.1b) shows a markedly rough surface due to the CNO-OXI layer. The presence of the poly(L-DOPA/DA) coating was confirmed by XPS (Figures 8.1c and S1, Supplementary Material). As it can be seen from Figure 8.1c, the C 1s region can be peak-fitted into five components corresponding to C sp^2 (284.4 eV, 11.6%), CHx/C=NH (284.8 eV, 39.3%), C-O/C-NH (286.1 eV, 27.7%), COOH (288.3 eV, 19.4%) and the π-π* relaxation shake-up (291.2 eV, 2%) [27]. This spectrum markedly differs from that of GCE/CNO-OXI, in which C sp^2 (284.3 eV, 88.2%) is the major peak.

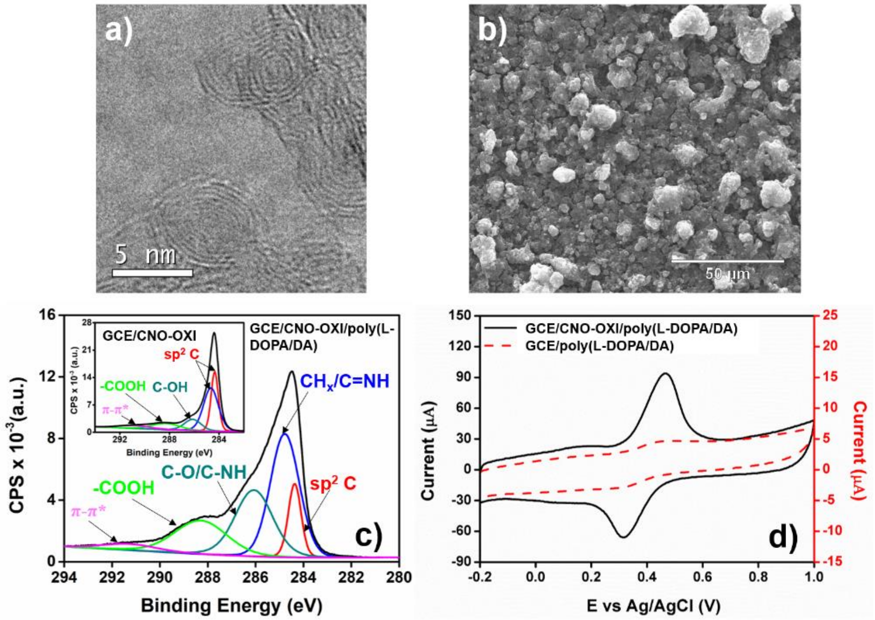

Figure 8.1. a) HRTEM image of CNO-OXI. b) ESEM image of the GCE/CNO-OXI/poly(L-DOPA/DA) surface. c) High resolution XPS spectra in the C 1s region of GCE/CNO-OXI/poly(L-DOPA/DA) and GCE/CNO-OXI (inset). d) Cyclic voltammograms for poly(L-DOPA/DA) films deposited on GC and GCE/CNO-OXI electrodes in 0.1 mol L^{-1} acetate buffer pH 5.0. Scan rate is 0.1 V s^{-1}.

Cyclic voltammograms of the first electropolymerization cycle in 10 mmol L^{-1} phosphate buffer pH 6.5 with 1:0, 1:5, 1:10, 1:20 and 0:1 L-DOPA:DA molar ratios are shown in Figure S2 (Supplementary Material). The peaks in the voltammograms are related with the redox processes that take place during the oxidative electropolymerization of catecholamines. In general, the intensity of the current peaks decreased cycle by cycle indicating a gradual decrease in the electrode activity toward L-DOPA and DA due to the electropolymerization of L-DOPA and DA on the GCE/CNO-OXI surface.

The modified GCE/CNO-OXI/poly(L-DOPA/DA) electrodes display well-defined anodic and cathodic peaks centered at 0.40 V, assigned to a two-electron-two proton oxidation/reduction of quinone/hydroquinone moieties in the deposited film (Figure 8.1d). The pH dependence of the oxidation-reduction peak potential was confirmed by recording cyclic voltammograms at different pH (Figures S3a-b in Supplementary Material). Both peaks shifted to more negative potentials as pH was increased. This kind of pH-dependent redox behavior has been applied for voltammetry and potentiometric determinations of pH [20,28]. The linearity observed between peak current and potential scan rates indicates that the quinone/hydroquinone redox conversion is surface confined, confirming the functionalization of the electrode surface with poly(L-DOPA/DA) films (Figure S4 in Supplementary Material). Remarkably, the peak current intensities of GCE/CNO-OXI/poly(L-DOPA/DA) were ~70-fold higher than those for GCE/poly(L-DOPA/DA) electrodes. This marked difference in current values can be explained considering that CNO-OXI increase the amount of electropolymerized catecholamines on the electrode because of a favorable adsorption of these molecules on the CNO-OXI modified surfaces as it was discussed in Chapter 6. Additionally, the presence of structural defects due to the chemical oxidation of CNOs favor the electron-transfer kinetics [29]. As a result, an enhancement of the current intensity of the electroactive species is observed when CNO-OXI are incorporated as conductive layer on GC surfaces.

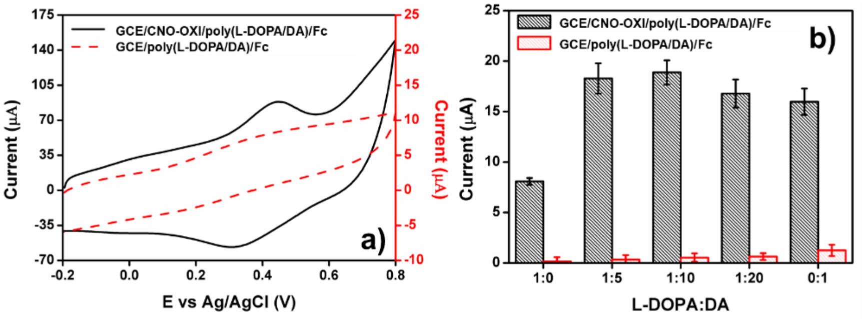

Figure 8.2. a) Cyclic voltammograms of GCE/CNO-OXI/poly(L-DOPA/DA) and GCE/poly(L-DOPA/DA) after covalent attachment of aminoferrocene in 0.1 mol L^{-1} $NaClO_4$ at 0.1 V s^{-1}. b) Plot of the anodic current of ferrocene-modified electrodes at different L-DOPA:DA ratios. All measurements were carried out in triplicate.

Aminoferrocene ($FcNH_2$) was used to estimate the L-DOPA:DA ratio that results in a poly(L-DOPA/DA) film with the highest number of available carboxylic acid moieties by attaching $FcNH_2$ via carbodiimide chemistry (Scheme 8.1b). Cyclic voltammograms recorded in 0.1 mol L^{-1} $NaClO_4$ showed a pair of anodic and cathodic peaks assigned to the ferrocenium/ferrocene (Fc^+/Fc^0) redox couple centered at 0.4 V (Figure 8.2a). The current intensities were also much higher in the case of electrodes incorporating CNO-OXI in comparison to GCE. The linear dependence of the current intensity with the scan rate indicates that the Fc^+/Fc^0 redox couples was attached to the electrode surface (Figure S5 in Supplementary Material).

Increasing the L-DOPA:DA molar ratio leads to increased anodic peak currents with a maximum at 1:10 L-DOPA:DA molar ratio followed by a further current as the L-DOPA:DA ratio increases (Figure 8.2b). This is explained considering that the DA residues spatially separate the carboxylic acid groups in the electropolymerized film up to an optimal ratio after which reducing the steric hindrance hampers further reactions. The interfacial concentration of immobilized ferrocene for this composition was (11.3 ± 0.4) nmol cm^{-2}. This value is 4.7 times higher than that obtained for ferrocenehexanethiol immobilized on a maleimide-CNO surface [19] and only 30% lower to that reported for Fc covalently grafted to a three-dimensional poly(aminoethylphenylene)/MWCNT surface [30]. This indicates that the surface resulting from the co-electropolymerization of the catecholamine mixture on the CNO surface contains a very large number of accessible carboxylate groups, at least for a small molecule like aminoferrocene. Thus, the 1:10 L-DOPA:DA ratio was used in the further construction of the immunosensors.

8.3.2. Fabrication of the electrochemical immunosensors for IgA detection

The GCE/CNO-OXI/poly(L-DOPA/DA) electrodes were used as a platform to construct a label-free and a sandwich type electrochemical immunoassay to detect IgA antibodies based on immobilized anti-human IgA antibodies (Scheme 1c).

Different blocking agents (1% BSA, 1% skim milk and 1 mol L^{-1} ethanolamine) were initially tested in order to minimize non-specific adsorption. The influence of the tested blocking agents on the signal response of the immunosensor in presence of $[Fe(CN)_6]^{3-/4-}$ before and after incubation of 500 ng mL^{-1} IgA is shown in Figure 8.3a. It is observed that the largest target/non-target current ratio was measured when 1% BSA was used and thus, it was selected as blocking agent for further work. Figure 8.3b shows the cyclic voltammograms in $[Fe(CN)_6]^{3-/4-}$ of the sequential steps leading to the preparation of the biosensor and after interaction with IgA. The CV of the GCE/CNO-OXI/poly(L-DOPA/DA) surface showed well-defined anodic and cathodic peaks corresponding to the $[Fe(CN)_6]^{3-/4-}$ redox pair. These peaks are overlapped with the redox peaks of the quinone groups of the polymer, are slightly more intense and are displaced 20 mV to lower potentials with respect to GCE/CNO-OXI (see Figure S3c in Supplementary Material), indicating a more favored electron transfer process presumably due to the conjugated character of the polymer and the existence of protonated amino groups at pH 7.4. The immobilization of α-IgA antibodies followed by the blocking step using BSA caused a decrease in the current peaks due to steric hindrance from the immobilized α-IgA and BSA layer. A further decrease in peak currents was observed after incubation with IgA, suggesting the formation of the immunocomplex onto the electrode.

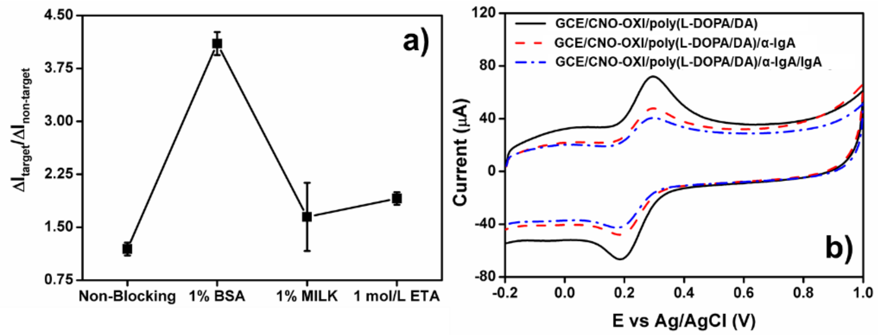

Figure 8.3. a) Effect of blocking agents on the DPV peak current of 1 mmol L^{-1} $[Fe(CN)_6]^{3-/4-}$ in PB before ($\Delta I_{non\text{-}target}$) and after ($\Delta I_{target}$) incubation with 500 ng mL^{-1} IgA on GCE/CNO-OXI/poly(L-DOPA/DA)/α-IgA electrodes (BSA: bovine serum albumin, MILK: skim milk, ETA: ethanolamine). All measurements were carried out in triplicate. b) Cyclic voltammograms for the steps involved in the construction of the IgA immunosensors in PBS containing 1 mmol L^{-1} $[Fe(CN)_6]^{3-/4-}$.

8.3.2.1. Analytical performance of the IgA immunosensors

The GCE/CNO-OXI/poly(L-DOPA/DA)/α-IgA and GCE/poly(L-DOPA/DA)/α-IgA immunosensors were incubated with standard IgA solutions in concentrations ranging from 0 to 5000 ng mL^{-1}. In the case of the label-free assay format, the change in the DPV peak current before and after the antigen/antibody immunoreaction (ΔI) was used as analytical output. For the sandwich assay format, the formation of immunocomplex was detected using HRP-labeled anti-IgA conjugate, followed by the measurement of the anodic current produced during the oxidation of TMB.

Figure 8.4 shows the calibration plots for IgA detection obtained with both formats in the presence and in the absence of CNO-OXI. A saturation of the immobilized capture antibody takes place at 5000 and 1000 ng mL^{-1} of IgA for the label-free and sandwich assays, respectively.

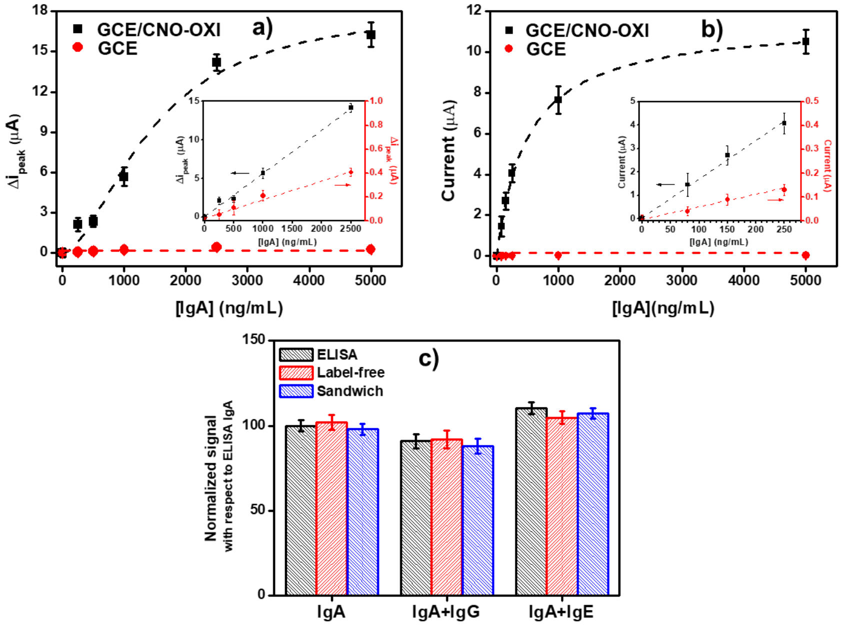

Figure 8.4. Calibration curves for IgA obtained with GCE/CNO-OXI/poly(L-DOPA/DA)/α-IgA and GCE/poly(L-DOPA/DA)/α-IgA immunosensors using a) the label-free, and b) the sandwich assay formats. c) Normalized response of the GCE/CNO-OXI/poly(L-DOPA/DA)/α-IgA immunosensor toward 40 ng mL^{-1} IgA, 40 ng mL^{-1} IgA+250 ng mL^{-1} IgG and 40 ng mL^{-1} IgA+20 ng mL^{-1} IgE. Each point is the average of the response obtained with three different biosensors.

For both assay formats, the incorporation of CNO-OXI results in a 3-order of magnitude enhancement of the assay sensitivity in comparison with the control surface in the absence of CNO-OXI. Assuming a linear behavior between 0–2500 ng mL^{-1} IgA, the sensitivity of the label-free biosensor was 5.6 nA·ng·mL^{-1}, with a detection limit of 48 ng mL^{-1}. In the case of sandwich format, the linear range was up to 250 ng mL^{-1} IgA, with a sensitivity of 16.1 nA·ng·mL^{-1}and LOD of 19 ng mL^{-1}. These values are well below the clinically relevant lower cut-off value for the determination of severe serum IgA immunodeficiencies, which is when the IgA concentration is lower than 70 µg mL^{-1} [31]. The measurements were also very reproducible, with standard deviations between 7 and 12% for measurements with three different sensors (inter-sensor reproducibility). A comparison between the analytical performances of reported IgA immunosensors with the proposed here is presented in Table 8.1. Compared with the ELISA assay and other reported sensors using the same immunoreagents, the proposed immunosensors exhibited an excellent sensitivity and linear range.

To monitor the selectivity of the immunosensor, IgG and IgE antibodies that are naturally found in body fluids were investigated for their influence on the IgA detection at the usual concentrations they are found in the serum of healthy individuals. The results were compared with an IgA ELISA assay and are shown in Figure 8.4c. IgG resulted in ~8% lower signals while IgE gave slightly increased signals (7%) and in both cases the immunosensor responses to IgA were practically not affected by the presence of the tested interferences with respect to the ELISA assay. Other metabolites such as glucose (5 mmol L^{-1}) and ascorbic acid (1 mmol L^{-1}) did not interfere in the measurements. Calf serum samples spiked with 70 and 1000 ng mL^{-1} of IgA gave signal recoveries of (96 ± 5) and (104 ± 5)% with respect to the value calculated from the calibration curve using the sandwich assay. This indicates that the proposed immunosensors are selective for IgA and are able to work in a complex matrix such as serum with minimal matrix effect.

Table 8.1. Comparison of the performance of the presented work with other IgA immunoassays

SP	SS	MD	LR (μg mL^{-1})	LOD (ng mL^{-1})	AT (h)		Ref.
					P	Det	
PAN	Nepm	Nepy	4 – 10.3	450	0	0.2	[32]
SPE/ AuNP-PEG	$[Fe(CN)_6]^{3-}$	SWV	0.087 – 1	0.5	15	0.75	[33]
Au/ SAM	HRP	CA	0.5 – 5	170	4	0.5	[34]
In-house ELISA	HRP	UV-Vis	0.0016 – 0.1	4.2	15	1.25	**This work**
GCE/ CNO-OXI/ poly(L-DOPA-DA)	$[Fe(CN)_6]^{3-}$	DPV	0-2.5	48	4.5	0.5	**This work**
	HRP	CV	0 – 0.25	19	4.5	1.25	

SP: sensing platform, SS: signal source, MD: methodology LR: linear range, AT: assay time, P: preparation, Det: detection, PAN: particle-enhanced nephelometry, Nepm: nephelometer, Nepy: nephelometry CA: choronoamperometry.

Finally, storage stability was studied for GCE/CNO-OXI/poly(L-DOPA/DA)/α-IgA biosensors stored in a microarray stabilizer (StabilCoat® Plus) at 4ºC (real time) and 37ºC (under accelerated conditions). After one week, the biosensors stored at 4ºC resulted in essentially the same initial response within the experimental error, while those stored at 37ºC gave 90% of the initial signal. Extrapolating the stability under accelerated conditions to real time using an Arrhenius kinetic model [35], this indicates that the biosensors stored at 4ºC need 39 weeks (~10 months) to decrease their affinity by 10% in this buffer. Therefore, this novel surface chemistry and the storage conditions used preserve antibody affinity facilitating long time storage and is in line with the stabilization observed for enzymes conjugated to CNOs [30].

8.4. Conclusions

In this Chapter, we have developed a novel electrochemical immunosensor for the detection of IgA antibodies based on the co-electropolymerization of L-DOPA and dopamine on CNO-OXI modified glassy carbon electrodes with label-free and sandwich detection. This novel surface provides a surface concentration of reactive carboxylic acid groups comparable to MWCNT-containing three-dimensional matrices, as evidenced by the immobilization of aminoferrocene by amidation reactions. The presence of the CNOs on the electrode surface in combination with the poly-catecholamine thin film increased the sensitivity of the developed electrochemical immunosensors by three orders or magnitude with respect to a poly-catecholamine-only surface. This enhanced sensitivity has been attributed to a combination of high loading of immunoreagents and increased electron transfer rates provided by the CNO layer. The wide linear range and low limits of detection obtained with the two studied immunoassay formats allow the detection of serum IgA in healthy people as well as in IgA deficient patients with the additional advantage of an ease of fabrication and assay simplicity with respect to a classical ELISA assay. These interesting features make the GCE/CNO-OXI/poly(L-DOPA/DA) surface a convenient immobilization platform extensible to the analysis of other relevant biomarkers.

References

[1] D. Wild, *The immunoassay handbook : theory and applications of ligand binding, ELISA and related techniques*, 4th edition, Elsevier B.V., Oxford, 2013.

[2] S. Leonardo, A. Toldrà, M. Rambla-Alegre, M. Fernández-Tejedor, K.B. Andree, L. Ferreres, K. Campbell, C.T. Elliott, C.K. O'Sullivan, Y. Pazos, J. Diogène, M. Campàs, *Self-assembled monolayer-based immunoassays for okadaic acid detection in seawater as monitoring tools*, Mar. Environ. Res. 133 (2018) 6–14.

[3] S.J. Goldsmith, *Radioimmunoassay: Review of basic principles*, Semin. Nucl. Med. 5 (1975) 125–152.

[4] E.P. Diamandis, T.K. Christopoulos, *Europium chelate labels in time-resolved fluorescence immunoassays and DNA hybridization assays*, Anal. Chem. 62 (1990) 1149A-1157A.

[5] P. Krämer, R. Schmid, *Flow injection immunoanalysis (FIIA) — a new immunoassay format for the determination of pesticides in water*, Biosens. Bioelectron. 6 (1991) 239–243.

[6] P. Zhang, X. Guo, H. Wang, Y. Sun, Q. Kang, D. Shen, *An electrode-separated piezoelectric immunosensor array with signal enhancement based on enzyme catalytic deposition of palladium nanoparticles and electroless deposition nickel-phosphorus*, Sensors Actuators B Chem. 248 (2017) 551–559.

[7] Q. Wu, D. Song, D. Zhang, H. Zhang, Y. Ding, Y. Yu, Y. Sun, *A highly sensitive SPR biosensor based on a graphene oxide sheet modified with gold bipyramids, and its application to an immunoassay for rabbit IgG*, Microchim. Acta. 182 (2015) 1739–1746.

[8] E.B. Bahadır, M.K. Sezgintürk, *Lateral flow assays: Principles, designs and labels*, TrAC Trends Anal. Chem. 82 (2016) 286–306.

[9] C. Kokkinos, A. Economou, M.I. Prodromidis, *Electrochemical immunosensors: Critical survey of different architectures and transduction strategies*, TrAC Trends Anal. Chem. 79 (2016) 88–105.

[10] B. Piro, S. Reisberg, B. Piro, S. Reisberg, *Recent advances in electrochemical immunosensors*, Sensors. 17 (2017) 794.

[11] F. Ricci, G. Adornetto, G. Palleschi, *A review of experimental aspects of electrochemical immunosensors*, Electrochim. Acta. 84 (2012) 74–83.

[12] P.S. Pakchin, S.A. Nakhjavani, R. Saber, H. Ghanbari, Y. Omidi, *Recent advances in simultaneous electrochemical multi-analyte sensing platforms*, TrAC Trends Anal. Chem. (2017).

[13] E. Valera, A. Hernández-Albors, M.P. Marco, *Electrochemical coding strategies using metallic nanoprobes for biosensing applications*, TrAC Trends Anal. Chem. (2016).

[14] G.A. Ortega, J.C. Zuaznabar-Gardona, E. Reguera, *Electrochemical immunoassay for the detection of IgM antibodies using polydopamine particles loaded with PbS quantum dots as labels*, Biosens. Bioelectron. 116 (2018) 30–36.

[15] M. Sireesha, V. Jagadeesh Babu, A.S. Kranthi Kiran, S. Ramakrishna, *A review on carbon nanotubes in biosensor devices and their applications in medicine*, Nanocomposites. 4 (2018) 36–57.

[16] E.B. Bahadır, M.K. Sezgintürk, *Applications of graphene in electrochemical sensing and biosensing*, TrAC Trends Anal. Chem. 76 (2016) 1–14.

[17] M. Rizwan, M. Hazmi, S.A. Lim, M.U. Ahmed, *A highly sensitive electrochemical detection of human chorionic gonadotropin on a carbon nano-onions/gold nanoparticles/polyethylene glycol nanocomposite modified glassy carbon electrode*, J. Electroanal. Chem. 833 (2019) 462–470.

[18] M. Rizwan, S. Elma, S.A. Lim, M.U. Ahmed, *AuNPs/CNOs/SWCNTs/chitosan-nanocomposite modified electrochemical sensor for the label-free detection of carcinoembryonic antigen*, Biosens. Bioelectron. 107 (2018) 211–217.

[19] J.P. Bartolome, L. Echegoyen, A. Fragoso, *Reactive carbon nano-onion modified glassy carbon surfaces as DNA sensors for human papillomavirus oncogene detection with enhanced sensitivity*, Anal. Chem. 87 (2015) 6744–6751.

[20] J.C. Zuaznabar-Gardona, A. Fragoso, *A wide-range solid state potentiometric pH sensor based on poly-dopamine coated carbon nano-onion electrodes*, Sensors Actuators B Chem. 273 (2018) 664–671.

[21] A.K. Trilling, J. Beekwilder, H. Zuilhof, *Antibody orientation on biosensor surfaces: a minireview*, Analyst. 138 (2013)

1619.

[22] T.G. Barclay, H.M. Hegab, S.R. Clarke, M. Ginic-Markovic, *Versatile surface modification using polydopamine and related polycatecholamines: chemistry, structure, and applications*, Adv. Mater. Interfaces. 4 (2017) 1601192.

[23] M. Dai, L. Sun, L. Chao, Y. Tan, Y. Fu, C. Chen, Q. Xie, *Immobilization of enzymes by electrochemical and chemical oxidative polymerization of L-DOPA to fabricate amperometric biosensors and biofuel cells*, ACS Appl. Mater. Interfaces. 7 (2015) 10843–10852.

[24] J.M. Cruse, R.E. (Robert E. Lewis, Atlas of immunology, CRC Press/Taylor & Francis, 2010.

[25] D. Soo-Quee Koh, G. Choon-Huat Koh, *The use of salivary biomarkers in occupational and environmental medicine.*, Occup. Environ. Med. 64 (2007) 202–10.

[26] E. Wajs, A. Molina-Ontoria, T.T. Nielsen, L. Echegoyen, A. Fragoso, *Supramolecular solubilization of cyclodextrin-modified carbon nano-onions by host–guest interactions*, Langmuir. 31 (2015) 535–541.

[27] M.B. Clark, J.A. Gardella, T.M. Schultz, D.G. Patil, L. Salvati, *Solid-state analysis of eumelanin biopolymers by electron spectroscopy for chemical analysis*, Anal. Chem. 62 (1990) 949–956.

[28] M. Amiri, E. Amali, A. Nematollahzadeh, H. Salehniya, *Poly-dopamine films: voltammetric sensor for pH monitoring*, Sensors Actuators B Chem. 228 (2016) 53–58.

[29] R. Borgohain, J. Yang, J.P. Selegue, D.Y. Kim, *Controlled synthesis, efficient purification, and electrochemical characterization of arc-discharge carbon nano-onions*, Carbon N. Y. 66 (2014) 272–284.

[30] A. Le Goff, F. Moggia, N. Debou, P. Jegou, V. Artero, M. Fontecave, B. Jousselme, S. Palacin, *Facile and tunable functionalization of carbon nanotube electrodes with ferrocene by covalent coupling and π-stacking interactions and their relevance to glucose bio-sensing*, J. Electroanal. Chem. 641 (2010) 57–63.

[31] L. Thibault, A. Beauséjour, M.J. de Grandmont, A. Long, M. Goldman, M.-C. Chevrier, *Establishment of an immunoglobulin-A deficient blood donor registry with a simple in-house screening enzyme-linked immunosorbent assay*, Transfusion. 46 (2006) 2115–2121.

[32] C.K. Booth, D.B. Dwyer, P.F. Pacque, M.J. Ball, *Measurement of immunoglobulin A in saliva by particle-enhanced nephelometric immunoassay: sample collection, limits of quantitation, precision, stability and reference range*, Ann. Clin. Biochem. 46 (2009) 401–406.

[33] M. Rizwan, D. Koh, M.A. Booth, M.U. Ahmed, *Combining a gold nanoparticle-polyethylene glycol nanocomposite and carbon nanofiber electrodes to develop a highly sensitive salivary secretory immunoglobulin A immunosensor*, Sensors Actuators B Chem. 255 (2018) 557–563.

[34] L.C. Rosales-Rivera, J.L. Acero-Sánchez, P. Lozano-Sánchez, I. Katakis, C.K. O'Sullivan, *Amperometric immunosensor for the determination of IgA deficiency in human serum samples*, Biosens. Bioelectron. 33 (2012) 134–138.

[35] N. Laboria, A. Fragoso, C.K. O'Sullivan, *Storage properties of peroxidase labeled antibodies for the development of multiplexed packaged immunosensors for cancer markers*, Anal. Lett. 44, (2011) 2019–2030.

Supplementary material of Chapter 8

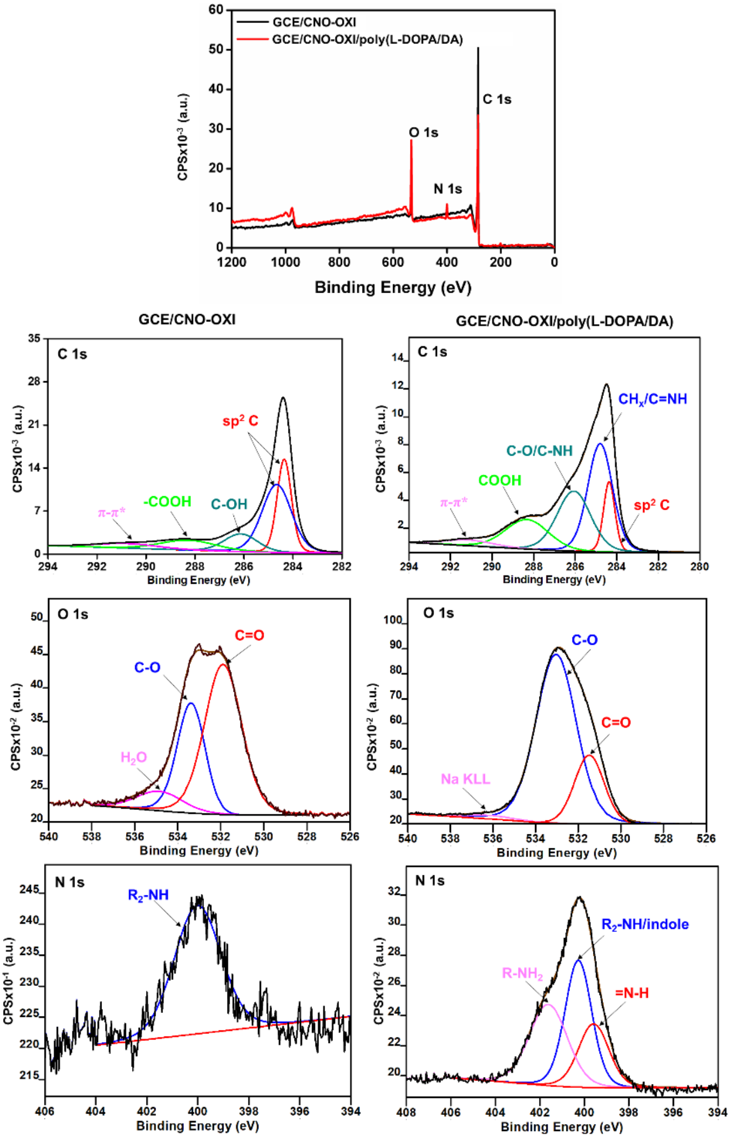

Figure S1. XPS survey spectra (top) and high resolution XPS spectra (bottom) of GCE/CNO-OXI and GCE/CNO-OXI/poly(L-DOPA-DA) surfaces.

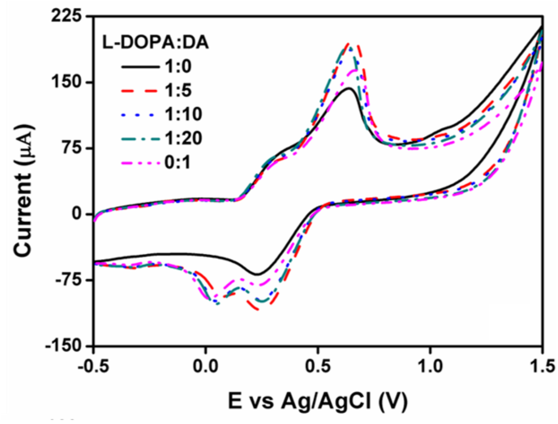

Figure S2. Cyclic voltammograms for the first electropolymerization cycle obtained for GCE/CNO-OXI electrodes in 0.1 mol L^{-1} PB solution containing different L-DOPA:DA molar ratios. Scan rate is 0.1 V s^{-1}.

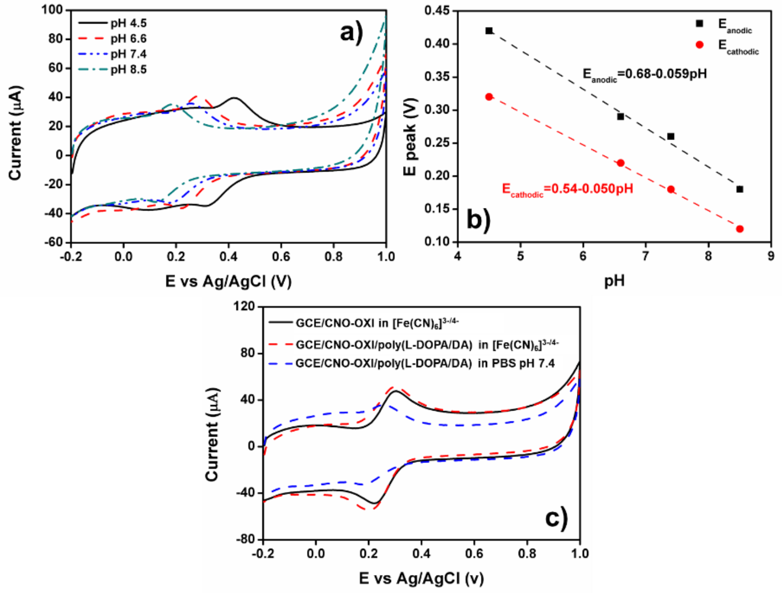

Figure S3. a) Cyclic voltammograms of GCE/CNO-OXI/poly(L-DOPA-DA) at pH 4.5, 6.6, 7.4 and 8.5. b) Plot of oxidation and reduction peak potentials as a function of pH corresponding to a). c) Cyclic voltammograms of GCE/CNO-OXI/poly(L-DOPA-DA) in PBS pH 7.4 and PBS containing 1mmol L^{-1} $[Fe(CN)_6]^{3-/4-}$.

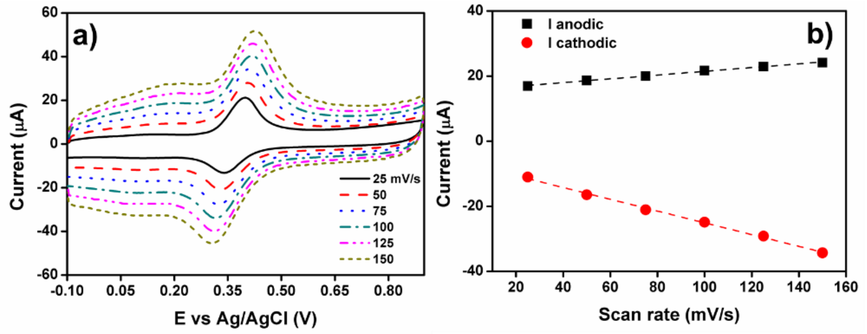

Figure S4. a) Cyclic voltammograms of GCE/CNO-OXI/poly(L-DOPA-DA) at 25, 50, 75, 100, 125 and 150 mV s^{-1} in 0.1 mol L^{-1} acetate buffer pH 5. b) Linear relationships between anodic and cathodic current and potential sweep rate of quinone/hydroquinone redox couple.

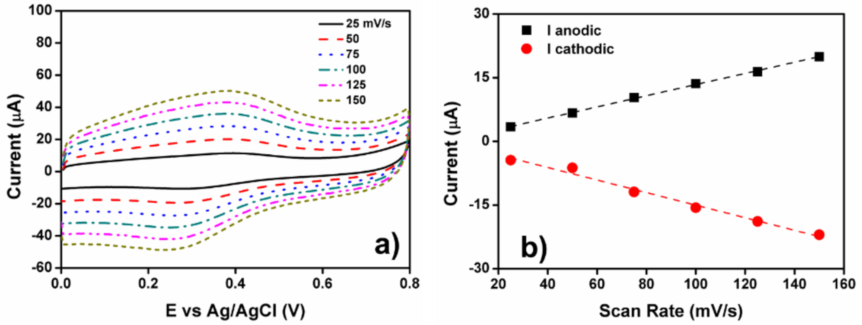

Figure S5. a) Cyclic voltammograms of GCE/CNO-OXI/poly(L-DOPA-DA)-Fc at 25, 50, 75, 100, 125 and 150 mV s^{-1} in 0.1 mol L^{-1} $NaClO_4$. b) Linear relationships between anodic and cathodic current and potential sweep rate of ferrocenium/ferrocene probe.

Conclusions and Future Work

Carbon materials and in particular those with nanometric dimensions exhibit a large number of unique properties leading to unprecedent functions with numerous applications. As it was described in the previous chapters, CNOs present very interesting properties which makes them promising materials for a wide range of applications. Thus, the focus of the present doctoral thesis was to prepare and characterize surfaces modified with CNOs to develop electrocatalytic systems and electrochemical (bio)sensors for biomedical and environmental applications.

In the first part of the present doctoral thesis, we studied the dispersibility, electronic structure, surface chemical composition, and electrochemical properties of CNOs. The dispersibility of CNOs was assessed in 20 solvent of different polarities to estimate the Hansen solubility parameters for CNOs using different optimization algorithms. These parameters were successfully used to predict the dispersion of CNOs in other solvents. The electronic structure and the surface chemical composition of pristine, physical and chemical oxidized CNOs were analyzed by using UPS and XPS. It was found that each oxidative treatment affects the electronic structure and the surface chemical composition of CNOs in different ways. The electrochemical properties of CNOs film were assessed by using outer- and inner-sphere redox probes. The results indicated the electron transfer kinetics for these probes were influenced by the nature of the functional groups on the electrode material, adsorption processes and the electrostatic interactions between the redox probes and the surface of the different carbon nano-onions.

In the second part of the thesis, we explored novel electrocatalytic properties and electrochemical (bio)sensing applications of CNOs. The electroreduction of O_2 to H_2O_2 in acid media and the electrooxidation of H_2O_2 AA, DA and UA were investigated at electrodes modified with pristine and oxidized CNOs. A novel potentiometric pH sensor based on polydopamine films coated on a CNOs conductive surface was presented. Moreover, the co-electropolymerization of DA and L-DOPA on CNOs modified electrodes were used as versatile platform to develop two electrochemical immunosensors to detect IgA antibodies. Overall, these examples demonstrate that CNOs enhance the electroactive properties of redox molecules and are thus promising materials for electrochemical detection and metal-free electrocatalysts of different reactions. Similarly, the incorporation of CNOs in the design of electrochemical (bio)sensors led to a significant improvement of the analytical performance of these devices.

Future work

-To evaluate the uses of CNOs on the development of enzymatic electrochemical biosensors.

-To explore the electropolymerization of other monomers (like dihydroxybenzenes, phenylboronic acids, cyclodextrins, etc.) on CNOs modified electrodes to develop novel electrochemical platforms.

-To incorporate nanoparticles on CNOs modified electrodes to assess their catalytic performance in chemical reactions of industrial interest (e.g. oxidation of polyalcohols, nitrogen reduction, methanol oxidation, etc.).

UNIVERSITAT
ROVIRA i VIRGILI